

Confocal Microscopy and Quantitative Single Molecule Techniques for Metrology in Molecular Medicine

vorgelegt von
Diplom-Physiker
Steffen Rüttinger
aus Halle (Saale)

Von der Fakultät II - Mathematik und Naturwissenschaften
der Technischen Universität Berlin
zur Erlangung des akademischen Grades

Doktor der Naturwissenschaften
- Dr.rer.nat. -

genehmigte Dissertation

Promotionsausschuss:

Vorsitzender: Prof. Dr. A. Knorr
Berichter: Prof. Dr. R. Macdonald
Berichter: Prof. Dr. H. J. Eichler

Tag der wissenschaftlichen Aussprache: 31. Oktober 2006

Berlin 2006

D 83

Meinen Eltern.

CONTENTS

<i>Abstract</i>	V
<i>Kurzzusammenfassung in deutscher Sprache</i>	VII
<i>Acknowledgments</i>	IX
<i>Introduction</i>	1
1. <i>Theoretical Part</i>	5
1.1 Fluorescence	5
1.1.1 Fluorescence Lifetime	7
1.2 Förster Resonant Energy Transfer	8
1.2.1 The Dipole Orientation Factor	12
Probability Distribution for κ^2	14
Averaging Regimes	16
1.3 Fluorescence Correlation Spectroscopy	18
1.3.1 The Free 3D Diffusion Model	20
1.3.2 Effective Volume	21
Autocorrelation	22
Crosscorrelation	23
1.3.3 Background	24
2. <i>Confocal Fluorescence Microscopy and Single Molecule Detection</i>	25
2.1 The Need for Small Detection Volumes	25
2.2 Principle of Confocal Microscopy	26
2.3 PicoQuant MicroTime200	28
2.4 The Resolution of a Confocal Fluorescence Microscope	30

2.4.1	The Excitation Intensity Distribution (EID)	30
2.4.2	The Excitation Probability Distribution (EPD)	32
2.4.3	The Collection Efficiency Function (CEF)	32
2.4.4	The Molecule Detection Function (MDF)	33
2.5	Data Analysis	33
2.5.1	Image Analysis	35
2.5.2	Instrument Response Function (IRF)	35
2.5.3	Fluorescence Correlation Spectroscopy	36
2.5.4	Determination of the Fluorescence Lifetime	36
2.6	Determination of the Confocal Volume by Imaging of Fluorescent Microspheres	38
3.	<i>Fluorescence Correlation Spectroscopy - Confocal Volume, Concentration, Molecular Brightness and Artifacts</i>	43
3.1	Sample Preparation and Experimental Details	45
3.2	Measuring the Confocal Volume with FCS	46
3.2.1	Dilution Series	48
3.2.2	Determination of the Confocal Volume from the FCS Fit	52
3.3	Determination of the Diffusion Coefficient using the Confocal Volume Param- eters acquired by Imaging of Fluorescent Microspheres	55
3.4	The Molecular Brightness	56
3.5	Sources of Artifacts and Systematical Errors	60
3.5.1	Optical Saturation	63
3.5.2	Cover-Slide Thickness Correction	68
3.5.3	Influence of the Pinhole Diameter	72
3.6	Discussion	75
4.	<i>Polyproline as Calibration Assay for FRET Distance Measurements</i>	79
4.1	The Poly-L-Proline Assay	82
4.1.1	Selection of the Fluorophores	82
4.1.2	Spectral Properties of Alexa-555 and Alexa-647	83
4.1.3	Structure of Poly-L-Proline	85
4.1.4	Dynamics of Poly-L-Proline - Worm-Like Chain Model	86

4.2	Sample Preparation and Experimental Details	88
4.3	FRET Analysis	90
4.3.1	Fluorescence Lifetime FRET	90
4.3.2	Burst Detection	90
4.3.3	Fluorescence Intensity FRET	92
	The apparent FRET efficiency - spectral crosstalk	92
	FRET with Pulsed Interleaved Excitation (PIE)	96
4.4	PIE-FRET Data Analysis	99
4.5	Results	101
4.5.1	Confocal Volume	102
4.5.2	Background	102
4.5.3	Donor-Only and Acceptor-Only Labeled Poly-L-Proline	103
4.5.4	Alexa-555 - Poly-L-Proline - Alexa-647	106
4.6	Trans-Location-Motif (TLM)	115
4.7	Concluding Remarks	117
5.	Summary	119
	<i>Acronyms</i>	123
	<i>References</i>	141

ABSTRACT

In the last decade, scientists from medicine, biology, chemistry, and physics have achieved great progress in exploring the structure of complex molecules, in particular of biomolecules. Beside structure, however, it is more and more evident that understanding of the dynamics of biomolecules is important to comprehend their function. Without analysis of the physical mechanisms of biomolecular dynamics it seems to be impossible to achieve progress in the understanding of the functioning of biological macromolecules. Within the frame of this work two experimental techniques have been investigated for their purposes to study biomolecular dynamics quantitatively on the level of single molecules:

1. Fluorescence Correlation Spectroscopy (FCS) was investigated as a tool to study fluctuations in the local concentration of molecules and their dynamic properties like diffusion.
2. Förster Resonance Energy Transfer (FRET) was investigated as a technique to determine distances between two molecules in close proximity (1 nm to 10 nm) under native conditions as well as dynamic changes in the conformation of biomolecules.

It is worth to note that the application of both methods on single molecules is important since ensemble measurements would barely help to gain the desired insight in the molecular dynamics and function due to the huge heterogeneity inherent to biological systems. The scope of this work was to evaluate the accuracy and the limits of quantitative FCS and FRET on the single molecule level. The experimental requirements will be given and hidden pitfalls are discussed. The needs for careful calibration and its realisation are shown. In particular, methods to obtain the detection volume of a confocal microscope and the experimental conditions influencing its shape are discussed, as knowledge of the so-called confocal volume is a prerequisite for quantitative FCS analysis. Secondly, a novel approach for FRET distance measurements is presented which accounts for incomplete labeled samples and experimental conditions, thereby increasing the accuracy of FRET distance measurements.

KURZZUSAMMENFASSUNG IN DEUTSCHER SPRACHE

Mediziner, Biologen, Chemiker und Physiker haben in den vergangenen 10 Jahren große Fortschritte bei der Erforschung der Struktur komplexer Biomoleküle vollbracht. Zum Verständnis der Funktion biologischer Makromoleküle, erweisen sich neben der Struktur die dynamischen Eigenschaften als immer wichtiger. Es erscheint unmöglich, hierbei Fortschritte im Verständnis zu erlangen, ohne die Physik biomolekularer dynamischer Prozesse zu analysieren. Im Rahmen dieser Arbeit wurden zwei experimentelle Techniken, hinsichtlich Ihrer Eignung biomolekulare Dynamiken auf Einzelmolekülniveau zu erforschen, untersucht:

1. Fluoreszenz Korrelations Spektroskopie (FCS), eine Methode zur Untersuchung lokaler Fluktuationen von Molekülen und Ihrer dynamischen Eigenschaften wie z.B. Diffusion.
2. Förster Resonanz Energie Transfer (FRET), eine Technik zur Bestimmung intra- oder intermolekularer Abstände im Bereich von 1 nm bis 10 nm unter nativen Bedingungen. Weiterhin ist es mit FRET möglich, Konformationsänderungen von Biomolekülen zu verfolgen.

Es ist wichtig, beide genannten Methoden auf einzelne Moleküle anzuwenden, da Ensemblemessungen kaum dazu beitragen können, den gewünschten Einblick in die molekularen Dynamiken und Funktionen stark heterogener, biologischer Systeme zu erlangen. Ziel der vorliegenden Arbeit ist die Evaluierung der Genauigkeit und der Grenzen quantitativer FCS und FRET Messungen auf Einzelmolekülniveau. Die experimentellen Voraussetzungen und Notwendigkeiten hierfür werden beschrieben und dabei auftretende Schwierigkeiten aufgezeigt. Die Notwendigkeit und Umsetzung genauer Kalibrationsmessungen wird verdeutlicht, im Besonderen werden Methoden, zur Bestimmung des konfokalen Volumens eines konfokalen Mikroskops sowie die experimentellen Bedingungen, die dessen Form beeinflussen, diskutiert. Weiterhin wird ein neuer Ansatz für FRET Abstandsmessungen vorgestellt, welcher erlaubt, unvollständig markierte Proben zu erkennen und bei der Auswertung

entsprechend zu berücksichtigen. Weiterhin ist mit dem neuen Ansatz eine genauere Berücksichtigung experimenteller Bedingungen möglich. Beides verbessert die Genauigkeit von FRET Abstandsmessungen deutlich.

ACKNOWLEDGMENTS

This work would not have been possible if not for the assistance, support, and guidance of numerous people. My thanks and appreciation goes to my dissertation advisor, Prof. Dr. Rainer Macdonald, for his critical input and encouragement throughout the past years. I am especially grateful for always having an open door to his office.

In addition I would also like to thank my other collaborators. Especially I would like to express my gratitude Dr. Benedikt Krämer, who has been very supportive. His guidance and views were invaluable. Even after he left the laboratory, he had always an open ear for my questions and I above all enjoyed the discussion of physical topics at the Trattoria in Friedenau. Sincere gratitude as well goes to Dr. Jörg Neukammer; his advice and experience were truly helpful for me. For critical input and assistance in the PTB laboratory I am also very grateful to Dr. Andreas Kummrow. In general I would like to thank the whole biomedical optics department of the PTB for a very enjoyable working atmosphere. In particular I would like to acknowledge Mr. Peter Pawlak for the realization of several components of the confocal setup.

This work would not have been possible without my collaborators at the Robert-Koch Institute who provided me with the samples and molecular modeling calculations for the FRET studies. Through the interaction with Dr. Martin Roos I was able to learn some of the chemical and biologic aspects of macromolecules. It is due to him, that I got an idea of the "greater picture" and biological relevancy of my work.

I gratefully acknowledge PicoQuant GmbH, Berlin, Germany where I carried out some of the most important experiments. They were kind enough to provide me with access to the latest in picosecond pulsed laser sources and single molecule detection technology. Additional thanks go to Dr. Volker Buschmann for his company and help with the FCS measurements.

Acknowledgments also go to Prof. Dr. Hans Joachim Eichler from the optical department of the Technische Universität Berlin for his helpful tips and advises.

Finally I want to express my sincere thanks to my friends and family who have given me the strength and encouragement I needed to finish my Ph.D., often at the expense of my neglect of them. In particular, I would like to thank my parents, who have always been there for me.

También quiero agradecer a Claudia, mi mujer, quien me acompañó durante todo mi trabajo de Tesis. Le agradezco su amor y cariño.

INTRODUCTION

In chemistry and biology text books molecular and cellular interactions are generally described on a single-molecule basis, although our knowledge of molecular dynamics has been deduced almost exclusively from experiments on ensembles of molecules. Nowadays, the possibility to perform and analyze experiments on single-molecules is seen as a major technological breakthrough, but which kind of information can be obtained that cannot be obtained by looking at the ensemble?

Most biological systems are either dynamically or stationary inhomogeneous and the inhomogeneities, especially dynamic inhomogeneities, are the key to understand their interactions and functions. For biological systems the ergodic hypothesis [1] does not hold. The trajectory time average of a physical quantity varies among members of the ensemble and therefore is no longer equivalent to the ensemble average. Ensemble measurements naturally can only yield the mean value of the ensemble. Single-molecule trajectories on the other hand are direct records of the fluctuation that contain detailed dynamical and statistical information. Since trajectories may vary for different members of the ensemble the average trajectory contains less information, the ensemble might not even show fluctuations at all as they could be averaged out during the timespan of the experiment.

Erwin Schrödinger in 1944 published a book entitled "What is life" [2] in which he postulated that although current theories in physics and chemistry were not adequate to completely account for all the events that occur in living organisms this did not mean that these sciences could not one day be able to do so. He supported this idea by describing the fundamental differences in structure between the systems that were classically studied by physicists, e.g. atoms and highly ordered periodic crystals, and the systems found in biology that are typically composed of many different types of atoms and adopt, at best aperiodic crystal structures. Thus, the statistical laws that were derived from these more homogeneous systems composed of enumerable atoms were overly simplified to be applied to systems found

in living organisms.

Numerous advances have been made since then and today an important hypothesis is that the understanding of biological systems (proteins, cells, cell structures, whole organisms) can be advanced by identification and quantification of appropriate parameters indicating the state and function of these systems. The state or function of a cell might be correlated with e.g. the number of a particular protein expressed on the cell surface. If so, the measuring task would be to quantify the number of expressed proteins. The state of the cell would then be expressed in appropriate units i.e. number of this selected protein per cell. The task in this case would be the selection of adequate proteins and their specific quantification.

Another important aspect of quantitative techniques in biomolecular research and application is to establish comparability of experiments among different biological systems, but also between different experimental instruments or different laboratories. Even if experiments need not to be quantitative to yield a certain information of interest the possibility to extract quantitative values gives objective criteria and assures the comparability and therefore repeatability of the experiment.

Quantitative results obtained from ensemble measurements might be too simplistic. For example, several copies of a protein or DNA may exist in several, sometimes transient, folded states. A measurement of an ensemble of these molecules would yield only an average structure, and not necessarily any of the actual structures they adopt.

A more or less straightforward application of single molecule detection is to push the limits of chemical or biochemical analytics towards ultra-sensitivity, i.e. the determination of lowest concentrations. If a single molecule of a fluorescent analyte can be detected within the detection volume of a confocal microscope, the concentration of this analyte is as low as a few picomolar.

A more practical advantage of single molecule methods is their inherent possibility to quantitate. Since in biological systems a single molecule may be considered as the smallest unit, quantitative results concerning the state or the property of such systems, can be obtained by identifying and analyzing this smallest unit and then expressing the quantity of interest in numbers of those units. It is for example possible to count the numbers of fluorescent labeled antibodies expressed on a cell surface by tracing their fluorescence intensity back to the fluorescence intensity of single fluorophores in the tissue of interest [3].

This work concentrates on single molecule confocal microscopy, as opposed to other types of microscopy capable of imaging single molecules such as Atomic Force Microscopy (AFM), Scanning Tunneling Microscopy (STM) etc. While with scanning probe techniques single molecules or even atoms can be studied on surfaces, confocal fluorescence microscopy is able to gain information from the interior of three dimensional structures and to resolve fast dynamics of molecular interactions. With confocal fluorescence microscopy specifically labeled individual biomolecules can be studied in-vitro and even in-vivo, which is considered very important as complex biological systems might behave completely different under only slightly modified conditions ex-vivo. The relatively noninvasiveness and high selectivity together with its high sensitivity are the main reasons for the remarkable boom confocal fluorescence microscopy has seen in the past years. Confocal detection coupled with analysis of sparse or single molecules in aqueous environments is currently considered one of the most promising tools [4] for many (molecular-) biological applications.

Fluorescence Correlation Spectroscopy (FCS) [5–9] and Förster Resonance Energy Transfer (FRET) [10–12] are the two methods that have been proven to be rather powerful, especially in the face of biochemical problems, and opened up a whole new field of biological science [13–15]. Despite the fact that both methods, FCS and FRET, are intrinsically quantitative they are mostly used in a qualitative manner.

FCS offers the possibility to measure very small local concentrations of molecules (or particles), together with dynamic properties of these moieties like e.g. diffusion coefficients. The first FCS experiments for example included measurements of DNA-drug intercalation [5, 6]. FCS has since been used to investigate the kinetics and thermodynamics of a wide range of processes [5, 7, 16–20]. The analytical and diagnostic potential of ultrasensitive FCS for the life sciences has been discussed and demonstrated [9, 19, 21, 22]. FCS also offers the possibility to determine the fluorescence intensity as a function of solution concentration (molecular brightness) which is important with respect to biomolecular fluorescence standards [23]. Although FCS is referred to as a technique for absolute concentration measurements it is usually employed to analyze relative concentrations or changes in molecular dynamics. This limitation is caused by a lack of exact knowledge of the confocal volume which is necessary for absolute concentration measurements as well as for the determination of diffusion coefficients. Chapter 3 is devoted to the determination of the confocal volume and several experimental

artifacts that cause a distortion of the confocal volume are discussed.

Förster Resonance Energy Transfer allows for distance measurements on the nm-scale [24]. While high resolution methods like x-ray crystallography and Nuclear Magnetic Resonance (NMR) have provided an enormous amount of structural detail of biological molecules they are limited to ensemble measurements. Studies of dynamic and interactive molecular processes ideally in the "native" environment are not possible with neither x-ray crystallography nor NMR. With FRET molecular structures can be investigated in-vitro and even in-vivo. A huge advantage over e.g. x-ray crystallographic studies where proteins are studied in their crystallized phase, a phase almost not existent in nature. Even though FRET can be used to measure distances on a molecular scale it is used almost exclusively in a decisive manner e.g. to detect colocalization [25–28] or to track conformational changes [29–33]. The difficulties of quantitative distance measurements with FRET are due to experimental artifacts like spectral crosstalk and different / unknown detection efficiencies. In conventional FRET experiments in solution, incompletely labeled FRET pairs give rise to the so-called zero efficiency peak which hampers the interpretation of experimental outcomes. The identification of incompletely labeled FRET pairs and the quantification of the experimental conditions in order to eliminate artifacts are scope of chapter 4 of this work. It will be shown that by utilizing FCS and especially the mentioned molecular brightness as a calibration standard FRET accuracy can be significantly enhanced. Quantitative distance measurements become achievable on the single molecule level. A distance calibration assay was developed and studied. The results allowed not only the determination of the conformation but also of the length of the TransLocation Motif (TLM), a protein important for the cell permeability of the HBV virus [34–37].

The scope of this work is to evaluate how quantitative FCS and FRET measurements can be done on the single molecule level. It will be examined what the experimental requirements are and where the pitfalls are hidden.

1. THEORETICAL PART

In this chapter the basic theoretical aspects and some of the history of fluorescence, Förster Resonance Energy Transfer and Fluorescence Correlation Spectroscopy will be explained.

1.1 Fluorescence

The Aztec culture of New Spain (México) had a rich tradition in herbal medicine that was recorded, among others, by Dr Francisco Hernández [38], who directed the first Spanish royal scientific expedition (1570-1577), and the Franciscan friar Bernardino de Sahagún [39], which registered plant descriptions from native physicians. In these two monumental works, that remained unknown for centuries, the wood of a small tree (coatli) used to treat kidney maladies is described, noting also the property of *turning blue* its water extract [40]. The first recorded observation dates back to 1646 when Athanasius Kircher, a German Jesuit priest, recorded an interesting observation of the wood extract of *Lignum nephriticum*. An aqueous extract of this wood exhibited blue color by reflected light and yellow color by transmitted light. The blue light is actually a type of light emission (fluorescence) and therefore Kircher is often regarded as the discoverer of fluorescence.

In 1856 William Perkin, an English chemist, synthesized a coal-tar dye, aniline purple (the first synthetic dye). His breakthrough attracted the attention of numerous synthetic chemists and a variety of dyes were synthesized. Perkin was acknowledged as the founder of the synthetic dye industry.

Fluorescence found its first biomedical application already in 1882 when Paul Ehrlich employed the fluorescent dye uranin to track the pathway of secretion of aqueous humor in the eye.

After the development of the first fluorescence microscope in 1911 by O. Heimstaedt and H. Lehmann, which was mainly used to investigate autofluorescence of bacteria and different other bioorganic substances already in 1914, S. Von Provaszek, a German protozoologist,

employed the fluorescence microscope to study dye binding to living cells. He stated that fluorochromes introduced into the cell effectively illuminate the partial functions of the cell in the dark field of the fluorescence microscope. So it was already almost a century ago that the foundations for the use of fluorescent markers to study structure and function of cells were laid. The rapid development of numerous fluorescence methods since then testifies the high potential of fluorescence techniques for the biological sciences.

In the following section I will shortly outline the theoretical aspects of fluorescence which date back to 1852 when George Stokes interpreted the light-emitting phenomenon and formulated the law that the fluorescent light is of longer wavelength than the exciting light (the Stokes Law or the Stokes Shift).

If a molecule, by absorption of a photon with suitable energy, is transferred into an excited electronic (singlet-) state S_1 it will return to the ground state S_0 sooner or later releasing the excitation energy. According to the Franck-Condon principle, the excitation is from the vibrational ground state of the electronically ground state to a higher vibrational state of the electronically excited state. In a matter of femto- to picoseconds a part of the energy is transferred to solvent molecules by collision - the molecule relaxes to the vibrational ground state of the electronically excited state. The relaxation of the lowest excited singlet state S_1 to a vibrational state (again due to the Franck-Condon principle) of the electronic ground state then may take place with a half-life time of nanoseconds by emission of electromagnetic radiation. This process is called fluorescence and the corresponding molecule is called a fluorophore. The frequency of the emitted radiation is shifted to the red compared to the frequency of the absorbed radiation, since a part of the absorbed energy is converted into thermal energy by vibrational relaxation (Stokes shift). The fluorescence is not the only relaxation process but competes with other radiationless relaxation processes: Internal Conversion (IC) and InterSystem Crossing (ISC) into the triplet state T_1 . The deactivation processes are shown in the so called Jablonski diagram (figure 1.1).

The relative contribution of fluorescence is the fluorescence quantum yield Q and can be expressed as the ratio of the rate constant k_F for fluorescence to the rate of all relaxation

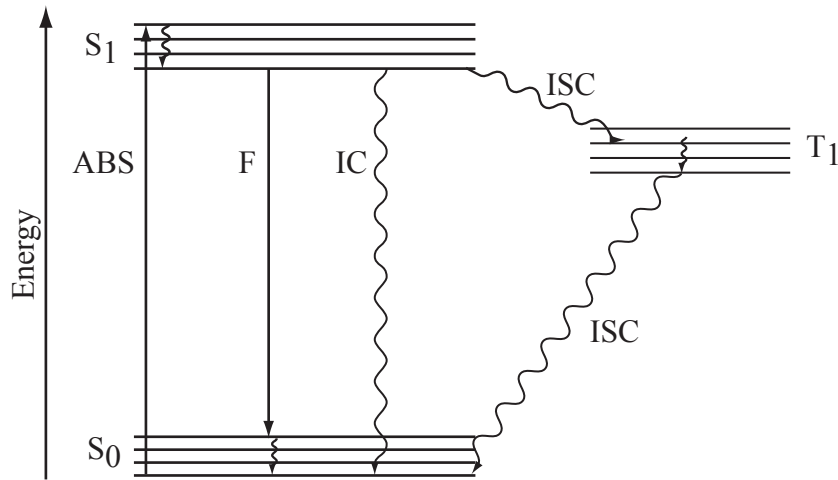


Fig. 1.1: simplified Jablonski diagram of a fluorophore. Possible relaxation processes of a fluorophore in the S_1 state, excited by the absorption (ABS) of a photon: fluorescence (F), Internal Conversion (IC) and InterSystem Crossing into the triplet state T_1 (ISC). Straight lines indicate radiative transitions while undulated lines indicate non-radiative transitions.

processes:

$$Q = \frac{\text{number of emitted photons}}{\text{number of absorbed photons}} = \frac{k_F}{k_F + \sum_i k_i} \leq 1, \quad (1.1)$$

where $\sum_i k_i = k_{IC} + k_{ISC}$.

Another way to define the fluorescence quantum yield is by the rates of the excited state decay: $Q' = \frac{k_F}{\sum_i k_i}$. I will stay with the first definition as it gives the more intuitive conversion efficiency of absorbed to emitted photons.

1.1.1 Fluorescence Lifetime

The time the molecule stays in the excited S_1 state before relaxation is an important parameter and is defined as the excited state or fluorescence lifetime τ :

$$\tau = \frac{1}{k_F + \sum_i k_i}. \quad (1.2)$$

The fluorescence lifetime can be measured e.g. by the decay of the fluorescence signal following short pulsed excitation. If the rate of spontaneous emission, or any of the other rates are

high, the lifetime is short (for commonly used fluorescent compounds typical excited state decay times are within the range of 0.5 to 20 nanoseconds). The fluorescence lifetime is an important parameter for practical applications of fluorescence such as Förster Resonance Energy Transfer (FRET).

According to (1.1) and (1.2) quantum yield and excited state lifetime are related:

$$Q = k_F \tau. \quad (1.3)$$

The time dependence of the decay is not necessarily mono exponential. Especially for compounds multi exponential or non exponential decays are observed. In these cases an average fluorescence lifetime is measured.

1.2 Förster Resonant Energy Transfer

Förster Resonance Energy Transfer (FRET) is the radiationless transmission of an energy quantum from an excited donor fluorophore to an acceptor by resonant interaction, over distances considerably greater than inter-atomic separations. For FRET to take place, donor emission spectrum and acceptor absorption spectrum need to overlap. The distance between donor and acceptor can be up to 10 nm. In literature the above defined phenomenon is also known as *Fluorescence Energy Transfer* or *Fluorescence Resonance Energy Transfer*. The term *Förster resonant energy transfer* is preferred, since the other mentioned names suggest that the transfer occurs through the emission and subsequent reabsorption of fluorescence. Although energy can be transferred by such an emission-reabsorption process as well, the above mentioned energy transfer occurs by radiationless dipole-dipole interaction. And last but not least the theory describing the energy transfer, both classically [41] and quantum mechanically [42, 43] was developed by Theodor Förster and the use of the term Förster Resonance Energy Transfer emphasizes his contribution.

Although the phenomenon is known since the beginning of the 20th century only in 1948 Förster was the first to propose that the transfer occurs by a resonant dipole-dipole interaction between the energy donor and acceptor chromophores [42]. In his treatment of weak coupling, the rate constant for transfer is proportional to the inverse sixth power of the

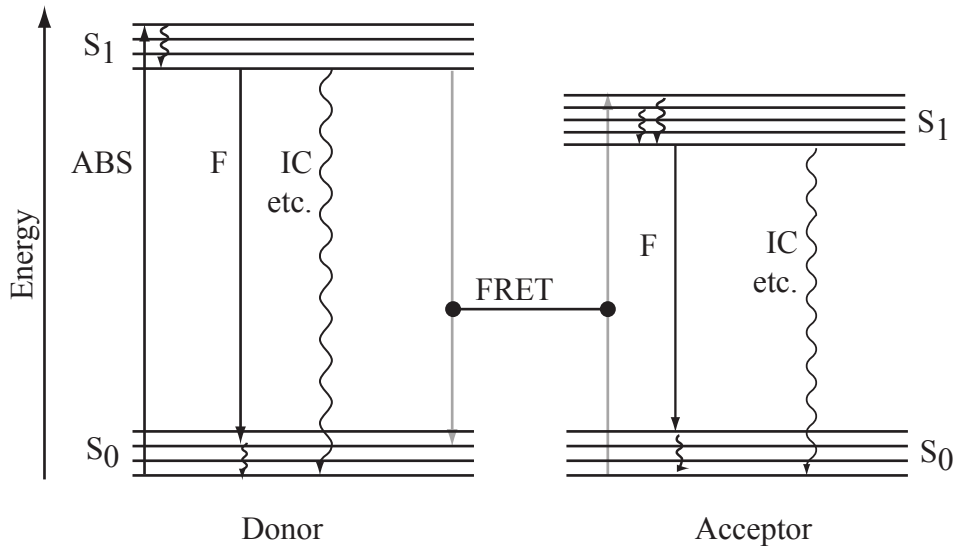


Fig. 1.2: Jablonski diagram of the FRET process. Only singlet states are shown for the sake of clarity.

distance between the chromophores¹. The energy transfer usually happens between singlet states and, therefore, sometimes is also known as singlet-singlet transfer. Figure 1.2 shows the process schematically. The horizontal line indicates that the energy transfer happens without loss, i.e. resonantly. It is not shown that the transfer may also take place to and from triplet states [44, 45]

In the presence of FRET an additional depopulation channel (see figure 1.2) is added to the relaxation processes described above: the energy transfer from the excited state of the donor to the acceptor, denoted by the rate k_T . The FRET process decreases the fluorescence quantum yield of the donor along with its fluorescence lifetime τ . If the acceptor (like shown in figure 1.2) is also a fluorophore, the relaxation of its excited state after excitation by FRET leads to fluorescence of the acceptor. The efficiency of FRET is given by the fraction of the number of photons transferred to the acceptor, divided by the number of absorbed photons:

$$E = \frac{k_T}{k_T + k_F + \sum_i k_i} \quad (1.4)$$

k_F denotes the radiative depopulation rate of the donor excited state to the donor ground state, k_T denotes the transfer rate to the acceptor and k_i represents the sum of all non radia-

¹ Weak coupling occurs when the interaction energy is smaller than the width of a single vibronic level

tive depopulation processes of the donor excited state without FRET. E can be calculated from the fluorescence quantum yield of the donor in presence (Q_{DA}) and in absence of an acceptor (Q_D):

$$E = 1 - \frac{Q_{DA}}{Q_D},$$

with

$$Q_{DA} = \frac{k_F}{k_T + k_F + \sum_i k_i},$$

$$Q_D = \frac{k_F}{k_F + \sum_i k_i}. \quad (1.5)$$

According to Förster [42] the energy transfer rate depends on the sixth power of the distance between donor and acceptor:

$$k_T = (k_F + \sum_i k_i) \left(\frac{R_0}{R} \right)^6 = \frac{1}{\tau_D} \left(\frac{R_0}{R} \right)^6, \quad (1.6)$$

where $\tau_D = 1/(k_F + \sum_i k_i)$ is the donor excited state lifetime in the absence of an acceptor. R_0 is the Förster distance, i.e. the distance at which the energy transfer rate (or probability) equals the sum of all other rates (probabilities) for deactivation of the donor excited state ($k_T = k_F + \sum_i k_i$ for $R = R_0$). Combining (1.6) and (1.4) yields:

$$E = \frac{1}{1 + (R/R_0)^6}. \quad (1.7)$$

E is the commonly used value to describe FRET quantitatively. It is the quantum yield of the transfer process. The distance dependence of E is shown in figure 1.3 in units of R_0 , the distance at which the transfer efficiency equals 50%. It is the strong distance dependence of E that makes FRET particularly interesting for applications like co-localization or separation measurements of biomolecules, as will be discussed in chapter 4.

From figure 1.3 it is obvious that distance measurements with FRET are most sensitive for distances around R_0 , since small variations of the donor-acceptor distance cause large change in the transfer efficiency. Hence the working range of FRET is usually limited to distances of about $0.5R_0$ to $1.5R_0$.

R_0 depends on the donor-acceptor pair under consideration. Typically $R_0 =$

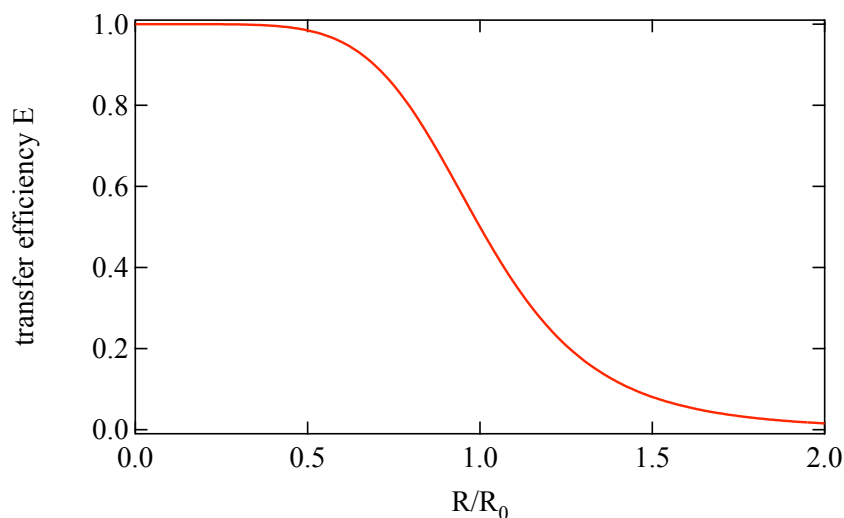


Fig. 1.3: Energy transfer efficiency E (eq. 1.7) as function of the distance R between donor and acceptor in units of R_0 .

4 nm to 6 nm. The working range of FRET therefore falls in the dimension of many biomolecules. The exact determination of R_0 , however, is one of the biggest obstacles for an accurate distance measurement with FRET. Basically, R_0 depends on the properties of the chosen donor and acceptor. It is therefore possible to calibrate a chosen donor-acceptor pair by using a molecule with known size. Förster [42, 43, 46, 47] derived the following equation for R_0 :

$$R_0^6 = \frac{9(\ln 10)\kappa^2 Q_D J(\lambda)}{128\pi^5 n^4 N_{Av}}, \quad (1.8)$$

where n is the index of refraction of the solvent and N_{Av} is Avagadro's number. κ^2 is a factor that reflects the relative orientation of the electronic dipoles. It takes a value of $2/3$ for molecules that are rotating much faster than the energy transfer rate. Q_D is the donor quantum yield in absence of acceptor molecules. $J(\lambda)$, known as the overlap integral is a measure of the spectral overlap of the fluorescence spectrum of the donor ($f(\lambda)$) and the absorption spectrum of the acceptor ($\epsilon(\lambda)$), see figure 1.4.

$$J(\lambda) = \int_0^\infty \epsilon(\lambda)f(\lambda)\lambda^4 d\lambda \quad (1.9)$$

This integral indicates that for efficient energy transfer, resonance is required between the donor emission and acceptor absorption. $\epsilon(\lambda)$ is the molar decadic extinction coefficient for a specific frequency and can be calculated using Beer's law $A = \epsilon(\lambda)lc$, where A is the

absorbance or optical density, l the length and c the concentration. $f(\lambda)$ is the normalized fluorescence spectrum of the donor:

$$f(\lambda)d\lambda = \frac{F(\lambda)d\lambda}{\int_0^\infty F(\lambda)d\lambda}. \quad (1.10)$$

$\epsilon(\lambda)$ usually is given in molar decadic extinction coefficient units ($M^{-1}cm^{-1}$), therefore the obvious unit for $J(\lambda)$ is $M^{-1}cm^3$. Evaluating the constants yield the following useful forms of equation 1.8:

$$R_0^6[\text{\AA}^6] = 8.79 \times 10^{23} \kappa^2 Q_D n^{-4} J(\lambda) \quad \text{with } [J(\lambda)] = M^{-1}cm^3 \quad (1.11)$$

$$R_0[\text{\AA}] = 9.78 \times 10^3 (\kappa^2 Q_D n^{-4} J(\lambda))^{1/6} \quad \text{with } [J(\lambda)] = M^{-1}cm^3 \quad (1.12)$$

$$R_0^6[\text{\AA}^6] = 8.79 \times 10^{-5} \kappa^2 Q_D n^{-4} J(\lambda) \quad \text{with } [J(\lambda)] = M^{-1}cm^{-1}nm^4 \quad (1.13)$$

Often equation 1.8 is given as:

$$R_0^6 = \frac{9000(\ln 10)\kappa^2 Q_D J(\lambda)}{128\pi^5 n^4 N_{Av}}, \quad (1.14)$$

implying that $J(\lambda)$ is given in $M^{-1}cm^3$. The factor 10^3 here results from the conversion of the volume unit liter to cm^3 ($M=\text{mol/l}$). The resulting R_0^6 is then given in cm^6 .

1.2.1 The Dipole Orientation Factor

The orientation factor κ^2 describes the angle between the emission dipole of the donor and the absorption dipole of the acceptor (see figure 1.5):

$$\kappa^2 = (\cos \theta_T - 3 \cos \theta_D \cos \theta_A)^2, \quad (1.15)$$

where θ_T is the angle between the emission transition moment of the donor and the absorption transition moment of the acceptor, θ_D is the angle between the donor emission transition moment and the vector connecting their centers ($\vec{R} = R\vec{e}_R$). θ_A is the angle between this vector and the acceptor transition moment. Theoretically κ^2 may vary from 0 to 4. If both the donor and acceptor rotate freely in a time that is short compared to the excited state lifetime of the donor, κ^2 equals $2/3$ [50]. If this is not the case, the situation becomes more

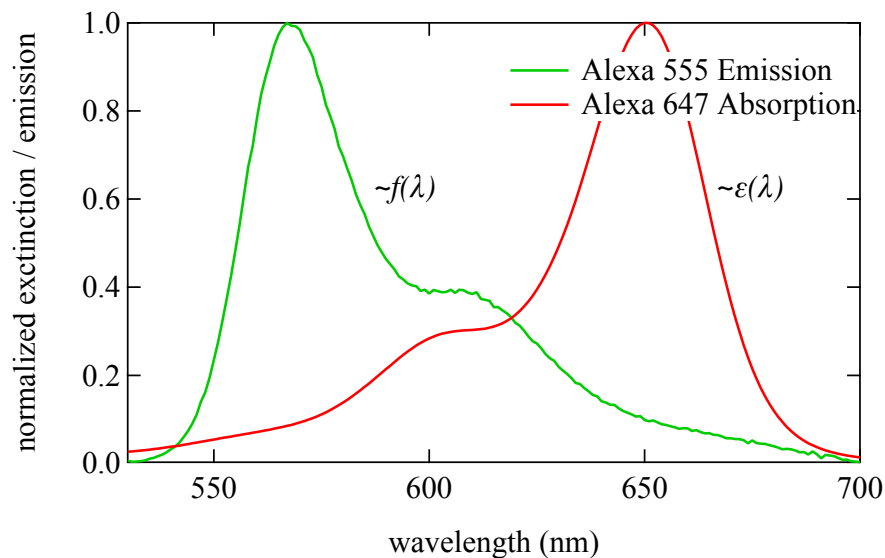


Fig. 1.4: Normalized emission spectrum ($\sim f(\lambda)$) of Alexa-555 oligo and normalized absorption spectrum ($\sim \epsilon(\lambda)$) of Alexa-647 oligo, both in H_2O . The area of overlap between both spectra defines the overlap integral $J(\lambda)$. Spectral data according to the Molecular Probes Website [48, 49]

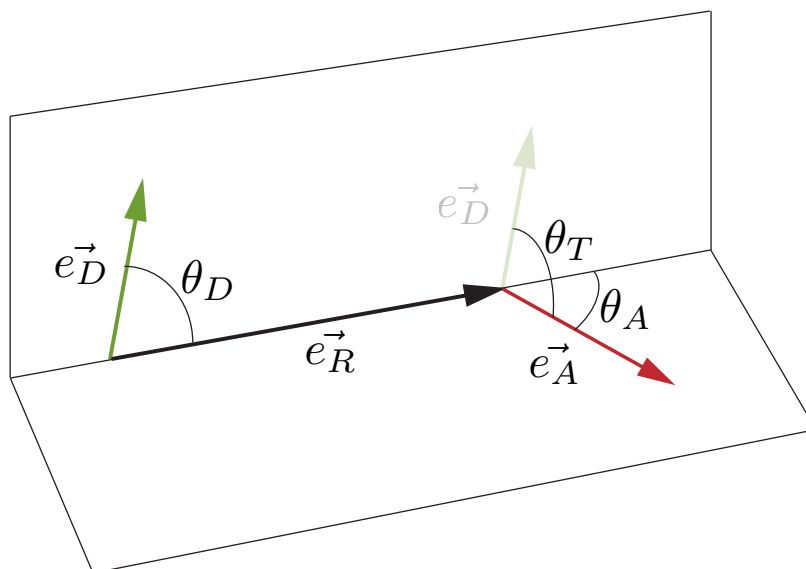


Fig. 1.5: Visualization of the angles used to define the relative orientation of the donor ($D\vec{e}_D$) and acceptor ($A\vec{e}_A$) transition moments and the separation vector $R\vec{e}_R$

complicated since the influence of κ^2 on R_0 and therefore on the transfer efficiency is strong. Upper and lower bounds for κ^2 can be deduced from anisotropy values at times that are short compared to the transfer time [50, 51]. If the transfer rate is comparable to the rotational motion, other values than $\kappa^2 = 2/3$ need to be taken into account. That can be done by using a model that incorporates all possible orientations [52].

The orientation factor can also be expressed in vector form using the unit vectors \vec{e}_D and \vec{e}_A , \vec{e}_R along the donor transition moment, the acceptor transition moment and the vector connecting the centers of both. Equivalent to (1.15):

$$\kappa^2 = (\vec{e}_D \cdot \vec{e}_A - 3(\vec{e}_D \cdot \vec{e}_R)(\vec{e}_A \cdot \vec{e}_R))^2 \quad (1.16)$$

The electric dipole vector, \vec{E}_D due to the donor transition moment at unit distance from the donor is given by:

$$\vec{E}_D = \vec{e}_D - 3(\vec{e}_D \cdot \vec{e}_R)\vec{e}_R = e_{\vec{E}_D} \sqrt{1 + 3(\vec{e}_D \cdot \vec{e}_R)^2}, \quad (1.17)$$

with $e_{\vec{E}_D}$ being the unit vector in the direction of \vec{E}_D . Combining (1.16) and (1.17) yields:

$$\kappa^2 = (\vec{E}_D \cdot \vec{e}_A)^2 = (e_{\vec{E}_D} \cdot \vec{e}_A)^2 [1 + 3(\vec{e}_D \cdot \vec{e}_R)]. \quad (1.18)$$

Defining ω as the angle between the electric dipole vector \vec{E}_D and the acceptor transition moment we obtain the following equation for κ^2 :

$$\kappa^2 = \cos^2 \omega (1 + 3 \cos^2 \theta_D). \quad (1.19)$$

$1 + 3 \cos^2 \theta_D$ describes the intensity of the electric dipole field produced by the donor transition moment at the location of the acceptor, which is modified by the factor $\cos^2 \omega$ to account for its component along the axis of the acceptor transition moment.

Probability Distribution for κ^2

Expressions for the probability distribution of κ^2 have been published by Dale et al. [50] as well as by Tompa and Englert [53]. However, since both publications have typographical

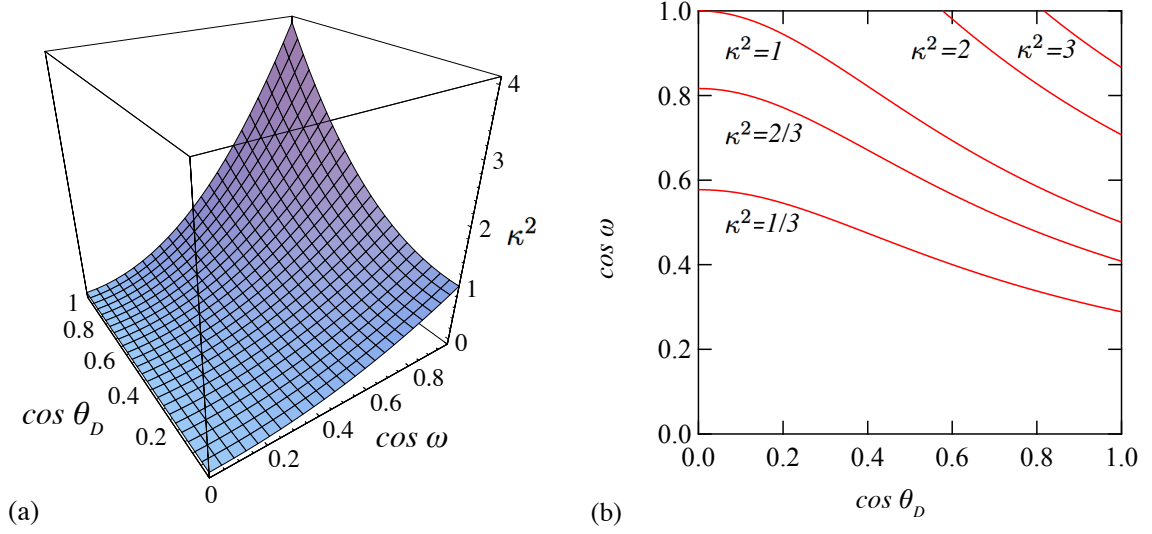


Fig. 1.6: (a) κ^2 versus $\cos \theta_D$ and $\cos \omega$. (b) $\cos \omega$ versus $\cos \theta_D$ at constant κ^2 . The curves are projections of horizontal cuts through the three dimensional curve shown in (a).

errors in the respective formulas, the review by van der Meer [54] is recommended instead.

The dependence of κ^2 on $\cos \omega$ and $\cos \theta_D$ is shown in figure 1.6a while figure 1.6b shows projections of horizontal cuts through the κ^2 -surface at constant κ^2 . Lets consider, that all orientations of \vec{e}_D , \vec{e}_A , \vec{e}_R are equally probable. The probability of finding a value of κ^2 in the range from 0 to κ^2 ($P_{\kappa^2}(0 - \kappa^2)$) then equals the area under the curves of figure 1.6b. For $\kappa^2 \leq 1$, $P_{\kappa^2}(0 - \kappa^2)$ equals the integral of $\kappa^2/(1 + 3x^2)$ from $x = \cos \theta_D = 0$ to $x = 1$. If κ^2 is larger than 1, the curve $\kappa^2 = \text{const}$ will intersect the line $y = \cos \omega = 1$ at $x = \cos \theta_D = \sqrt{(\kappa^2 - 1)/3}$. Thus $P_{\kappa^2}(0 - \kappa^2)$ in that case is given by $\sqrt{(\kappa^2 - 1)/3}$ + the integral of $\kappa^2/(3x^2 + 1)$ in the limits of $x = \sqrt{(\kappa^2 - 1)/3}$ and $x = 1$. These integrations yield the following expression:

$$P_{\kappa^2}(0 - \kappa^2) = \begin{cases} \sqrt{\frac{\kappa^2}{3}} \ln(2 + \sqrt{3}), & 0 \leq \kappa^2 \leq 1 \\ \sqrt{\frac{\kappa^2 - 1}{3}} + \sqrt{\frac{\kappa^2}{3}} \ln\left(\frac{2 + \sqrt{3}}{\sqrt{\kappa^2} + \sqrt{\kappa^2 - 1}}\right), & 1 \leq \kappa^2 \leq 4 \end{cases}. \quad (1.20)$$

The difference between $P_{\kappa^2}(0 - \kappa_1^2)$ and $P_{\kappa^2}(0 - \kappa_2^2)$ represents the probability of finding a κ^2 between κ_1^2 and κ_2^2 . This leads to the definition of the probability density:

$$\rho(\kappa^2) = \frac{dP_{\kappa^2}(0 - \kappa^2)}{d\kappa^2}, \quad (1.21)$$

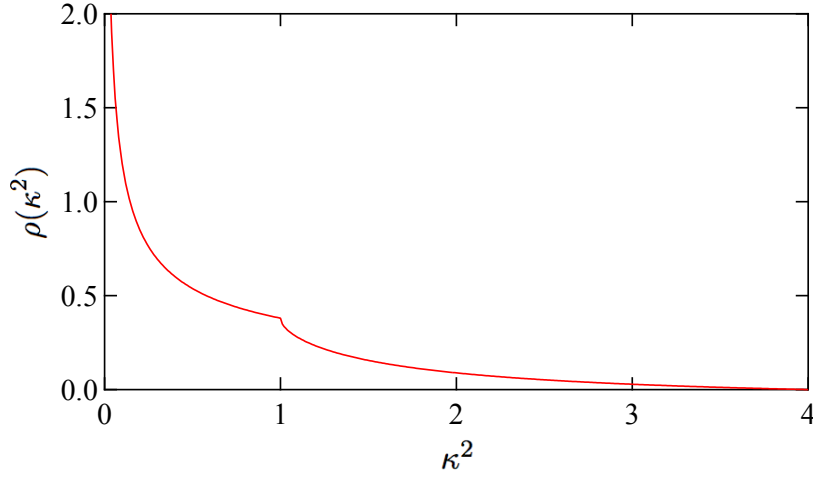


Fig. 1.7: The isotropic probability density $\rho(\kappa^2)$ versus the orientation factor κ^2 . $\rho(\kappa^2)d\kappa^2$ is the probability of encountering a value of the orientation factor between κ^2 and $\kappa^2 + d\kappa^2$, if all orientations of the transition moments of donor and acceptor are equally probable.

And the differentiation of equation 1.20 yields:

$$\rho(\kappa^2) = \begin{cases} \frac{1}{2\sqrt{3}\kappa^2} \ln(2 + \sqrt{3}), & 0 \leq \kappa^2 \leq 1 \\ \frac{1}{2\sqrt{3}\kappa^2} \ln\left(\frac{2+\sqrt{3}}{\sqrt{\kappa^2+\sqrt{\kappa^2-1}}}\right), & 1 \leq \kappa^2 \leq 4 \end{cases} \quad (1.22)$$

Figure 1.7 shows a plot of equation 1.22. The probability of finding a value of the orientation factor lying between κ^2 and $\kappa^2 + d\kappa^2$ is given by $\rho(\kappa^2)d\kappa^2$.

Averaging Regimes

If the donor and acceptor can take up their entire range of orientations during the time the energy transfer occurs, the system is said to be in the dynamic averaging regime. In this case the orientation factor can be replaced by its appropriate average value $\langle \kappa^2 \rangle$, obtained by integrating the probability density $\rho(\kappa^2)$ over all possible values for κ^2 . The average transfer efficiency $\langle E \rangle_{dynamic}$ is calculated according to the following equation:

$$\langle E \rangle_{dynamic} = \left(1 + \frac{1}{\frac{3}{2}\langle \kappa^2 \rangle} (R/R_{\frac{2}{3}})^6 \right)^{-1} \quad (1.23)$$

$R_{\frac{2}{3}}$ stands for R_0 calculated assuming $\langle \kappa^2 \rangle = 2/3$. For the case that all orientations are equally probable, the probability distribution is the isotropic probability distribution given by equation 1.22 and $\langle \kappa^2 \rangle$ equals the already mentioned 2/3. The dynamic isotropic averaging

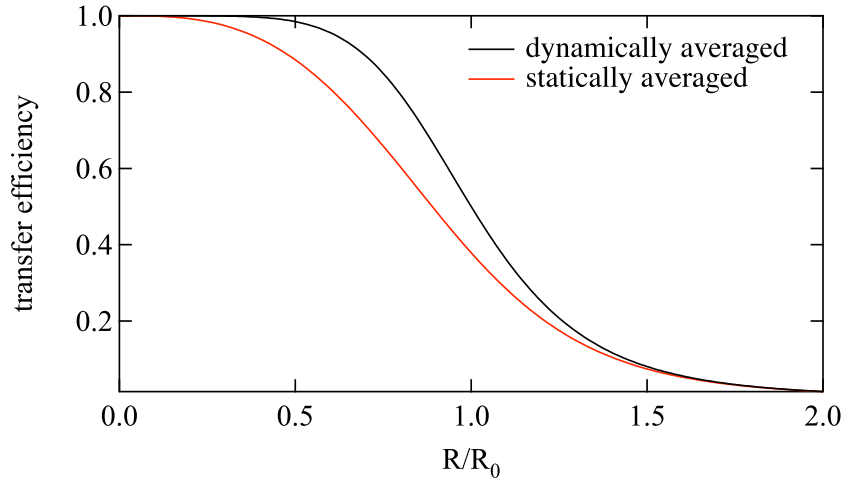


Fig. 1.8: The dynamically (black line, eq. 1.24) and statically (red line, eq. 1.25) averaged transfer efficiencies as functions of R/R_0 , assuming that all transition moment orientations are equally probable (isotropic assumption).

condition is satisfied and equation 1.7 is reproduced:

$$\langle E \rangle_{dynamic} = (1 + (R/R_0)^6)^{-1}. \quad (1.24)$$

If, on the other hand, the rotational motion is much slower than the energy transfer process, the transition moment orientations are static but random during the transfer process, hence the transfer efficiency cannot be calculated assuming $\langle \kappa^2 \rangle = 2/3$. The system is said to be in the static averaging regime. If, again, all transition moment orientations are equally probable the average transfer efficiency can be calculated utilizing the isotropic probability density (1.22):

$$\begin{aligned} \langle E \rangle_{static} &= \left\langle \left(1 + \frac{1}{\frac{3}{2}\kappa^2} (R/R_{\frac{2}{3}})^6 \right)^{-1} \right\rangle \\ &= \int_0^4 \left(1 + \frac{1}{\frac{3}{2}\kappa^2} (R/R_{\frac{2}{3}})^6 \right)^{-1} \rho(\kappa^2) d\kappa^2. \end{aligned} \quad (1.25)$$

Figure 1.8 shows the comparison between dynamically and statically averaged transfer efficiencies calculated under the isotropic assumption. The area between the two curves corresponds to all averaging regimes between the static and the dynamic limits. As expected, for low transfer efficiencies, the averaging regime is seen to make little difference.

As can be seen in figure 1.8, the distance at which the transfer efficiency equals 50% is

reduced for the static but random case. Compared with the FRET efficiency for $\kappa = 2/3$ the critical distance R_0 is reduced to $R_0^{static} = 0.89 * R_0$. At a distance R_0 the transfer efficiency has already dropped to 38% compared to the $\kappa^2 = 2/3$ case where it drops to 50%.

1.3 Fluorescence Correlation Spectroscopy

Correlation analysis was originally introduced for noise suppression and statistical data analysis by Wiener in 1949 [55]. Fluorescence Correlation Spectroscopy (FCS) is the application of this method to fluorescence signals. FCS was originally introduced in the early 1970s [5–7, 56]

In correlation analysis signal fluctuations are studied. During ensemble measurements fluorescence signal fluctuations are not observable in general due to the large number of molecules involved. If, however, the number of particles in the detection volume is reduced drastically, fluorescence fluctuations become prominent. Those fluctuations can be caused by concentration fluctuations due to diffusion but also by fluctuations of the photophysical property of the molecule itself.

FCS measures fluorescence intensity fluctuations (e.g. due to brownian motion of a particle through the detection volume), caused by a small number of molecules. Due to the necessity for small concentrations the signal intensity in FCS experiments is limited and hence is the Signal to Background ratio (S/B) since only a few fluorescent molecules are surrounded by a huge number of solvent molecules within the detection volume which strongly contribute to the measuring signal e.g. by scattering the excitation light. The breakthrough of FCS therefore came in the 1990 after the pioneering work of Rigler [8, 57–59] who applied FCS analysis to confocal microscopy. In doing so, the effective detection volume could be reduced, which largely increased the S/B ratio and enabled the analysis of single molecule fluctuations. The size of the detection volume is of great importance. Since the number of fluorescent molecules is small, the number of molecules contributing to the background signal must be kept as small as possible as well.

FCS analyzes the resemblance of a signal time trace with itself (autocorrelation) or with a different signal (crosscorrelation) e.g. from a second detector or a second fluorescent species in the sample. By calculating the auto/cross-correlation of a fluctuating signal $F(t)$, time-dependent dynamics can be followed.

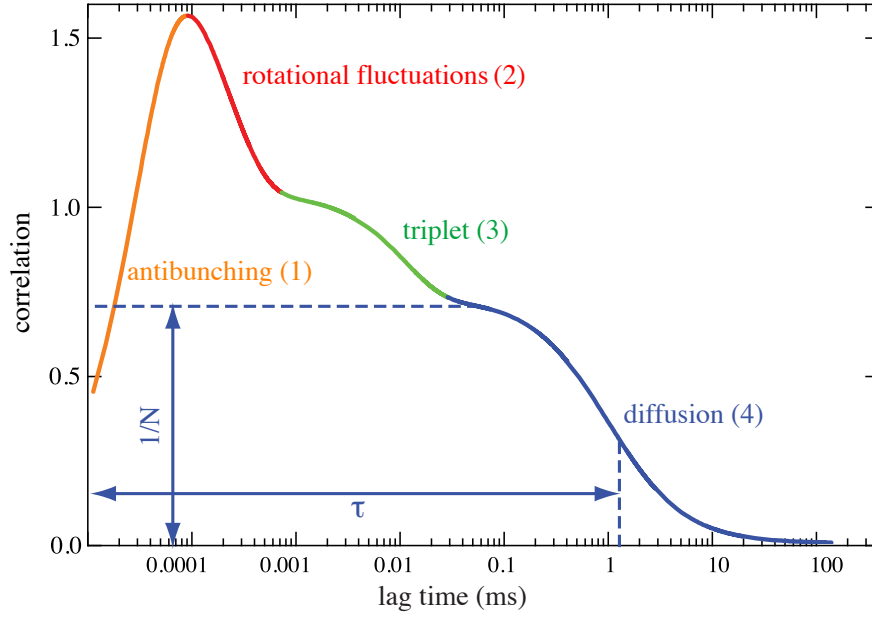


Fig. 1.9: Theoretical FCS curve for fluorophores of one species with with diffusion (4), triplet kinetics (3), rotational fluctuation (2) and antibunching (1). N equals the number of fluorophores in the singlet states (S_1 or S_0) and τ is the diffusion time.

The general form of the normalized fluctuation correlation function reads as follows:

$$G_{i \times j} = \frac{\langle \delta F_i(t) \delta F_j(t + \tau) \rangle}{\langle F_i(t) \rangle \langle F_j(t) \rangle}, \quad (1.26)$$

with $i = j$ for autocorrelation and $i \neq j$ for crosscorrelation. The number of detected fluorescence photons per time at detector D is of the following form:

$$F_D = \sum_k g_k^D \int_V \phi_{ex}(\vec{r}) CEF^D(\vec{r}) \sigma_k Q_k n_k(\vec{r}, t) dV. \quad (1.27)$$

k runs over all fluorescent species contributing to F_D . g_k^D is the photon to count conversion efficiency of filter and detector D , ϕ_{ex} is the Excitation Intensity Distribution (EID) (see also section 2.4.1), the spatial distribution of the photon flux density with amplitude ϕ_0 and $CEF^D(\vec{r})$ is the Collection Efficiency Function, a dimensionless optical transfer function of the detector pinhole combination (see also section 2.4.3). σ_k is the molecular absorption cross section, Q_k the quantum efficiency and n_k the particle number density. Individually these parameters are difficult to measure, therefore, $\phi_{ex}(\vec{r})/\phi_0 \cdot CEF(\vec{r})$ are usually combined into the Molecule Detection Function (MDF), a single distribution function $W_D(\vec{r})$ (see also

section 2.4.4). $W_D(\vec{r})$ depends on the detection wavelength and therefore is labeled with the index D of the detector. Furthermore we combine ϕ_0 with the factors g_k^D , σ_k and Q_k into a parameter that is proportional to the count rate per detected molecule: $\beta_k^D = \phi_0 g_k^D \sigma_k Q_k$. It depends on the fluorophore (k) and detection channel (D).

The fluorescence fluctuations detected with detector D can then be written as:

$$\delta F_D(t) = \phi_0 \sum_k \int_V W_D(\vec{r}) \delta(\beta_k^D n_k(\vec{r}, t)) dV. \quad (1.28)$$

Fluctuations may either occur in β_k^D or in n_k : $\delta(\beta_k^D n_k(\vec{r}, t)) = n_k \delta\beta_k^D(t) + \beta_k^D(t) \delta n_k(\vec{r}, t)$. The intramolecular fluctuations contribute to the first term, whereas particle motion and reaction kinetics govern the latter. In the case where only diffusion is responsible for the fluctuation, it is $\delta\beta_k^D = 0$, i.e. no intramolecular fluctuation and no attractive or repulsive forces between the molecules contribute. The correlation function in this case becomes:

$$G_{i \times j}(\tau) = \frac{\int_V \int_{V'} W_i(\vec{r}) W_j(\vec{r}') \sum_k \beta_k^i \beta_k^j \langle \delta n_k(\vec{r}, t) \delta n_k(\vec{r}', t + \tau) \rangle dV dV'}{\langle F_i(t) \rangle \langle F_j(t) \rangle}. \quad (1.29)$$

1.3.1 The Free 3D Diffusion Model

For translational diffusion the fluctuation term can be replaced by the so-called concentration correlation factor:

$$\begin{aligned} \Phi_k(\vec{r}, \vec{r}', \tau) &= \langle \delta n_k(\vec{r}, 0) \delta n_k(\vec{r}', \tau) \rangle \\ &= \langle n_k \rangle (4\pi D_k \tau)^{-3/2} \exp\left(-\frac{(\vec{r} - \vec{r}')^2}{4D_k \tau}\right). \end{aligned} \quad (1.30)$$

Equation 1.29 then becomes:

$$G_{i \times j}(\tau) = \frac{\int_V \int_{V'} W_i(\vec{r}) W_j(\vec{r}') \sum_k \beta_k^i \beta_k^j \Phi_k(\vec{r}, \vec{r}', \tau) dV dV'}{\langle F_i(t) \rangle \langle F_j(t) \rangle}. \quad (1.31)$$

The concentration correlation factor determines the joint probability of finding the molecule k at a position \vec{r}' at a time τ which was at $\tau = 0$ at position \vec{r} , multiplied by the average particle number density $\langle n_k \rangle$. D_k is the Diffusion coefficient of the molecule. When integrating over space the meaning of the concentration correlation function becomes evident: It is the

probability that a molecule detected at $\tau = 0$ is still in the detection volume at time τ . It is a decay function with its parameter τ describing the average residence time in the detection volume.

1.3.2 Effective Volume

For $\tau = 0$ the concentration correlation factor is $\Phi(\vec{r}, \vec{r}', 0) = \langle n_k \rangle \delta(\vec{r} - \vec{r}')$ (time origin of the diffusion equation) and for a single fluorescent species the normalized fluctuation correlation function becomes:

$$\begin{aligned} G_{i \times j}(0) = G_0 &= \frac{\int \int W_i(\vec{r}) W_j(\vec{r}') \beta^i \beta^j \langle n \rangle \delta(\vec{r} - \vec{r}') dV dV'}{\langle n \rangle^2 \beta^i \beta^j \left(\int W_i(\vec{r}) dV \right) \left(\int W_j(\vec{r}') dV' \right)} \\ &= \frac{\beta^i \beta^j \langle n \rangle}{\beta^i \beta^j \langle n \rangle^2} \frac{\int W_i(\vec{r}) W_j(\vec{r}') dV}{\left(\int W_i(\vec{r}) dV \right) \left(\int W_j(\vec{r}') dV' \right)} \\ &= \frac{1}{\langle n \rangle V_{eff}} = \frac{1}{\langle N \rangle}, \end{aligned} \quad (1.32)$$

with

$$V_{eff} = \frac{\left(\int W_i(\vec{r}) dV \right) \left(\int W_j(\vec{r}') dV' \right)}{\int W_i(\vec{r}) W_j(\vec{r}') dV}. \quad (1.33)$$

The fluctuation correlation amplitude gives the inverse number of particles which are detected on average.

The usually applied confocal optics with diffraction-limited illumination and detection through field apertures or so-called pinholes in the image plane have to be described by Fourier optics [60, 61], where the objective point spread function is convoluted with the geometrical pinhole function. In the diffraction limited case, the illumination point spread function is described by Bessel functions. It can be, however, approximated by a Gaussian profile in lateral and by a Lorentzian profile in axial direction, if the back aperture is under-filled² [8, 16]. The convolution routine, inferred by the pinhole function can however not be solved analytically for a Gauss-Lorentz beam. For this reason a three-dimensional Gaussian distribution is often assumed for $W(\vec{r})$:

$$W(\vec{r}) = \exp\left(-\frac{2(x^2 + y^2)}{w_0^2}\right) \exp\left(-\frac{2z^2}{z_0^2}\right), \quad (1.34)$$

² Underfilling of the back aperture yields weaker focussing, the focal spot is not diffraction limited.

with w_0 and z_0 defining the $1/e^2$ values of $W(\vec{r})$ in the lateral and axial axis respectively.

$W(\vec{r})$ is nonzero for every point in space. The confocal volume therefore is of infinite size causing the probability to detect a fluorescent molecule, dependent on its location in the sample, to be naturally nonzero throughout the space. The integrals of the Gaussian functions, however, are convergent allowing us to assign a finite, effective volume V_{eff} . The fluorescence correlation function can be calculated analytically using the 3D-Gaussian approximation.

Autocorrelation

For autocorrelation $W_i(\vec{r})$ is identical to $W_j(\vec{r})$. By inserting equation 1.34 into equation 1.31 we get the autocorrelation function:

$$\begin{aligned} G(\tau) &= \frac{1}{w_0^2 z_0 \pi^{3/2} \langle n \rangle} \cdot g(\tau) \\ &= G_0 \cdot g(\tau) \\ &= \frac{1}{V_{eff} \langle n \rangle} \cdot g(\tau) \\ &= \frac{1}{\langle N \rangle} \cdot g(\tau), \end{aligned} \tag{1.35}$$

with

$$g(\tau) = \left(1 + \frac{4D\tau}{w_0^2}\right)^{-1} \left(1 + \frac{4D\tau}{z_0^2}\right)^{-1/2} \tag{1.36}$$

being the shape function of the autocorrelation function while the first part, $G(\tau = 0) = G_0$, gives the amplitude and is equal to the inverse average number of detected particles $\langle N \rangle$.

The proportionary factor $\pi^{3/2} w_0^2 z_0$ is the effective volume:

$$V_{eff} = \pi^{3/2} w_0^2 z_0. \tag{1.37}$$

With the knowledge of V_{eff} the concentration of the sample can be calculated from G_0 . It is worth noting that the effective volume is not the confocal volume. For autocorrelation the effective volume (compare eq. 1.33) is defined as:

$$V_{eff} = \frac{[\int W(\vec{r}) d\vec{r}]^2}{\int W^2(\vec{r}) d\vec{r}}, \tag{1.38}$$

whereas the confocal volume is calculated by integrating the shape function over space:

$$V_{3DG} = \int W(\vec{r}) d\vec{r}. \quad (1.39)$$

By comparing equation 1.39 (using (1.34)) with equation 1.37 it turns out, that for the 3D-Gaussian approximation the confocal volume is only about 1/3 of the corresponding effective Volume:

$$V_{3DG} = \left(\frac{\pi}{2}\right)^{3/2} w_0^2 \cdot z_0 = \left(\frac{1}{2}\right)^{3/2} V_{eff}. \quad (1.40)$$

Crosscorrelation

Crosscorrelation investigates the correlation of two different signals with each other. Applications include colocalization experiments, investigation of binding kinetics or FRET determination through FCS. The most simple application of crosscorrelation analysis is to split the fluorescence signal into two detection channels. By correlating the signals of two detectors correlations caused by the detectors e.g. afterpulsing are suppressed. Other possibilities include the usage of two different fluorophores excited by two different lasers or by the same laser e.g. with 2-photon excitation or anisotropy measurements where the parallel and orthogonal components of the fluorescence emission are correlated with each other. Recently crosscorrelation of two-focus FCS has been used to measure the diffusion coefficient of ATTO-655 unbiased by experimental artifacts that introduce distortions to the confocal volume [62].

In dual color crosscorrelation W_i will not equal W_j even if only one laser is used for excitation because the collection efficiency function $CEF_k(\vec{r})$ depends on the emission wavelength. The excitation and/or detection profiles of both detection channels will differ in size. The corresponding effective volume is:

$$V_{eff}^\times = \pi^{3/2} \frac{(w_i^2 + w_j^2)}{2} \sqrt{\frac{(z_i^2 + z_j^2)}{2}}, \quad (1.41)$$

with w_i and w_j , respectively z_i and z_j being the $1/e^2$ half axis of the two different 3D Gaussian MDFs W_i and W_j .

1.3.3 Background

The presence of uncorrelated background reduces the correlation amplitude since the intensity of the fluctuations is reduced. This results in apparently higher concentrations and needs to be taken into account if the signal to background ratio is low.

If there is uncorrelated background (like ambient light or dark counts of the photo detectors) the detected fluorescence signal in detector D can be written as:

$$F_D(t) = f_D(t) + b_D(t), \quad (1.42)$$

where f is the signal due to fluorescence and b signal due to uncorrelated background. The normalized fluctuation correlation function 1.26 then becomes:

$$G_{i \times j} = \frac{\langle \delta [f_i(t) + b_i(t)] \delta [f_j(t + \tau) + b_j(t + \tau)] \rangle}{\langle f_i(t) + b_i(t) \rangle \langle f_j(t) + b_j(t) \rangle} \quad (1.43)$$

and, because by definition the background signal is uncorrelated:

$$G_{i \times j} = \frac{\langle \delta f_i(t) \delta f_j(t + \tau) \rangle}{\langle f_i(t) + b_i(t) \rangle \langle f_j(t) + b_j(t) \rangle} \quad (1.44)$$

which can be written as:

$$G_{i \times j} = \frac{1}{\chi_i \chi_j} \frac{\langle \delta f_i(t) \delta f_j(t + \tau) \rangle}{\langle f_i(t) \rangle \langle f_j(t) \rangle}, \quad (1.45)$$

with

$$\frac{1}{\chi_i \chi_j} = \frac{1}{(1 + \langle b_i \rangle / \langle f_i \rangle) (1 + \langle b_j \rangle / \langle f_j \rangle)} \quad (1.46)$$

$\chi_i \chi_j$ (or χ^2 for autocorrelation) is the background correction factor. It compensates the damping of the correlation amplitude by uncorrelated background signal. The background-corrected number of particles in the effective volume is calculated according to:

$$\langle N \rangle = \frac{1}{\chi_i \chi_j G_{ij}}. \quad (1.47)$$

2. CONFOCAL FLUORESCENCE MICROSCOPY AND SINGLE MOLECULE DETECTION

In this chapter the principle of confocal microscopy will be described, followed by a presentation of the experimental setup. After explaining the data analysis techniques that were used throughout this work, a method to obtain the detection volume of the confocal microscope by imaging fluorescent microspheres will be presented.

2.1 *The Need for Small Detection Volumes*

”It is not difficult to detect the fluorescence of a single molecule but NOT to detect anything else.” (Richard A. Keller)

For single molecule detection one key parameter is, as for almost all other experiments as well the Signal to Noise ratio (S/N). The second crucial parameter is the Signal to Background ratio (S/B). Background is a (sometimes quantifiable) bias to the signal, which originates from scattering of the excitation light or residual ambient light. Even if the signal can be corrected for background contribution, the background decreases the contrast of the signal of interest.

Since the number of fluorescence photons that a single fluorophore can emit is limited to some 10^6 photons, the maximum signal a single fluorophore can emit is limited. Therefore the only way to increase the S/B is to decrease the background. Background can be due to endogenous (auto-) fluorescence of cells or tissues or simply due to elastic or inelastic scattering of the excitation light of the laser. While elastic scattering can usually quite efficiently be suppressed by appropriate filters, parts of inelastic scattering like Raman scattering may fall into the same spectral region as the fluorescence signal and therefore passes the detection filter. Although the cross section for Raman scattering is about a factor of 10^8 smaller than that for fluorescence the huge excess of solvent molecules over one single target molecule increases the yield for Raman scattering drastically.

The signal of a single molecule depends on the time the molecule stays in the detection volume V and is limited by the maximum number of excitation relaxation cycles the molecule can undergo before it leaves the detection volume. For free diffusion this time and therefore the signal intensity is proportional to $V^{1/3}$. The background intensity on the other hand is proportional to the number of additional molecules in the detection volume and therefore directly proportional to the detection volume. The signal to background ratio therefore increases with decreasing volume as:

$$S/B \propto \frac{V^{1/3}}{V} = V^{-2/3}. \quad (2.1)$$

Confocal microscopy has been proven to be a very efficient tool to reduce background by reducing the measurement volume to below femtoliters.

2.2 *Principle of Confocal Microscopy*

Figure 2.1 shows the principle of a scanning confocal microscope. The excitation light source is a laser with a suitable wavelength. The laser beam passes a dichroic beamsplitter with high reflectivity at the laser wavelength but high transmission at different wavelengths. A high Numerical Aperture (NA) microscope objective focusses the incident beam into the sample. The excitation intensity is highest in the focal point but fluorescence (and scattering) is generated in the whole volume illuminated.

The fluorescence photons (as well as scattered excitation light) are collected by the same objective, pass the dichroic filter and focussed onto the confocal pinhole. This pinhole is placed conjugate to the spot being illuminated. Because the pinhole is confocal, other spots than the focal point in the specimen are not focussed at the pinhole, so that most of the light originating from these spots cannot pass the pinhole. The light reaching the detector from out-of-focus regions is thus greatly attenuated. In addition, the pinhole diameter can be made smaller than the diameter of the Airy diffraction image formed by the objective lens so that the Airy disk is trimmed down to regions near its central peak.

Photons that pass the confocal pinhole are detected by a suitable detector e.g. a Photo Multiplier Tube (PMT) or an Avalanche Photo Diode (APD) equipped with a suitable bandpass filter, rejecting ambient and elastically scattered excitation light.

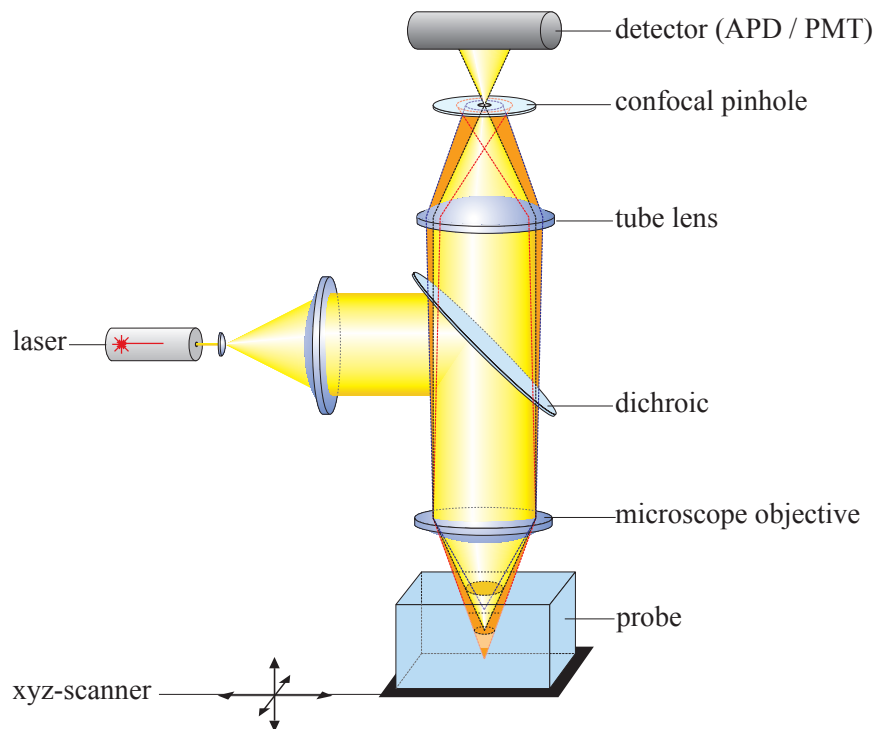


Fig. 2.1: Principle of confocal microscopy: The excitation laser is focused to a tight spot by a microscope objective. Emitted fluorescence is collected by the same objective, passes through a dichroic mirror, and is focused by the tube lens onto the confocal pinhole. Photons passing the pinhole are then detected by an APD or PMT. Image generation is achieved by scanning either the probe (shown), the objective or the excitation beam. (Figure adapted from Zeiss AG)

The image of the specimen is created by either moving the objective or the specimen by the means of a piezo scanner. Since the confocal microscope, through the confocal pinhole, provides depth of focus it is possible to scan the sample not only in the xy plane but also to record images with depth resolution as scans of the xz -, yz - or even arbitrary planes. Furthermore it is possible to record stacks of planes and then reconstruct 3D images of the specimen.

Another scanning method is not to scan the specimen or objective, but the laser beam itself, by the means of galvanic mirrors. The advantage thereof is the improved scanning speed. Beam scanning only can be used lateral, the axial resolution still has to be provided by scanning the sample or objective.

2.3 *PicoQuant MicroTime200*

The measurements presented in this work were performed on a MicroTime 200 confocal microscope (PicoQuant, Berlin, Germany). The MicroTime system is comprised of 4 parts: A modified Olympus IX71 inverted microscope stand, equipped with an Olympus UPlanAPO NA 1.2 water immersion objective. Laser incoupling and fluorescence collection happens through the main optical unit, shown schematically in figure 2.2. The main optical unit is connected to the microscope body via the sideport. The excitation laser beam passes an adjustable attenuator (not shown) and is coupled into the main optical unit via a single mode fiber. There, the beam is directed via the major dichroic mirror into the Olympus IX71. Using an additional beamsplitter (Mirror 2), a part of the excitation light is directed to a photo diode. The output of the photo diode was calibrated by measuring the laser output on the microscope table (after the objective) with a calibrated powermeter and then used to determine the excitation light intensities. Simultaneously, a back reflection from the sample was directed via the same mirror onto a CCD camera. The fluorescence emission passes the major dichroic mirror and is focussed onto the adjustable pinhole by the detection tube lens, where off-focus photons are rejected. Beamsplitter 3 and 2 can be used to extend the detection unit with additional detectors. However, only two detection channels were used and both beamsplitters remained empty. Beamsplitter 1 was used to either spectrally separate the fluorescence emission for two color detection (FRET measurements, chapter 4) or to equally split the fluorescence emission for FCS crosscorrelation measurements as done in chapter 3. Finally the emission filters placed directly in front of the detector units select the spectral detection range and additionally suppress scattered excitation or ambient light. For detection Single Photon counting Avalanche Diode modules (SPADs) supplied by Perkin Elmer (SPCM-AQR 14) were used.

Image generation was achieved by scanning the objective with a xyz-piezo scanner. The actual position of which is registered together with the detected photons so that the spatial origin of every detected photon is recorded.

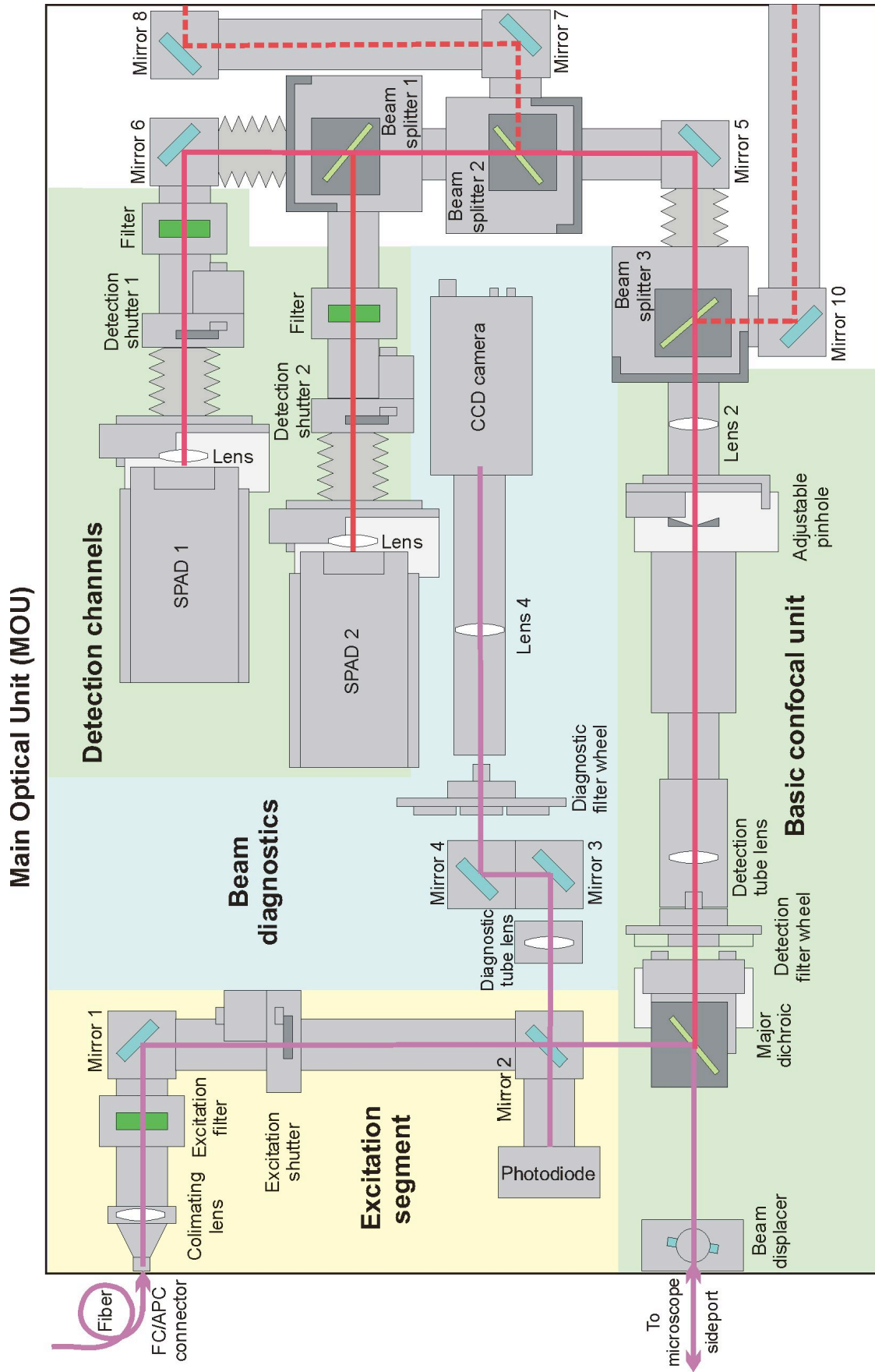


Fig. 2.2: Main optical unit of the MicroTime 200 confocal fluorescence microscope.

excitation		
wavelength	λ_{ex}	635 nm
beam waist ($1/e^2$ -radius)	w_0	2.37 mm
detection		
wavelength	λ_{em}	(687 ± 35) nm
Objective		
numerical aperture	NA	1.2
magnification	M	60x
tube length	l_T	180 mm
back aperture radius		4 mm
pinhole diameter		63 μm
sample		
refractive index	n	1.33

Tab. 2.1: Experimental parameters used for the FCS studies in chapter 3 and throughout this section.

2.4 The Resolution of a Confocal Fluorescence Microscope

The resolution of a confocal fluorescence microscope is determined by the Molecule Detection Function (MDF). The MDF quantifies the efficiency of detecting a fluorescence photon from a fluorescing molecule at a given position in the sample. If the emission dipole orientation is statistically independent of the absorption dipole orientation (rotational diffusion time much faster than the fluorescence lifetime), then the MDF is given by the direct product of the excitation probability distribution (EPD) and the Collection Efficiency Function (CEF). If the excitation intensity is much below saturation, the EPD is proportional to the Excitation Intensity Distribution (EID) and the MDF will be the product of the EID and the CEF.

Usually the term confocal volume (V_{conf}) is used as a practical measure of the resolution of a confocal microscope. The borders of the confocal volume are defined by the $1/e^2$ values of the MDF. The confocal volume is the volume in which the efficiency of detecting a fluorescence photon from a fluorophore exceeds 13.5% of the maximum efficiency.

In the following a simplified expressions of the EID, the CEF and the MDF will be given. Where applicable the experimental parameters of the setup, as relevant in chapter 3, are used for illustration (see table 2.1).

2.4.1 The Excitation Intensity Distribution (EID)

The excitation laser, upon leaving the polarization maintaining mono-mode fiber, is assumed to be a Gaussian beam. Its Rayleigh length, a measure of the divergence of the laser beam,

is given by

$$z_R(w_0, \lambda_{ex}) = \frac{\pi n w_0^2}{\lambda_{ex}}, \quad (2.2)$$

where $w_0 = 2.37$ mm is the beam waist of the excitation laser, measured after the fiber out-coupler, λ_{ex} the vacuum wavelength of the excitation laser and n the refractive index of the medium. In front of the objective the refractive index is $n = 1$ (air) while behind the objective the refractive index of the medium (water, $n = 1.33$) has to be used. It is assumed, that the focussed beam is also Gaussian, a valid assumption if the beam diameter is small compared to the back aperture of the objective. In the experimental setup the beam waist was about half that of the back aperture. The Rayleigh length changes when the laser beam is focused by the objective:

$$z'_R(w'_0, \lambda_{ex}) = \frac{f^2 z_R}{(z_l - f)^2 + z_R^2}, \quad (2.3)$$

where f is the focal length of the objective:

$$f = \frac{n l_T}{M}, \quad (2.4)$$

with $M = 60$ being its magnification. $l_T = 180$ mm is the tube length and z_l is the objective position with respect to the beam waist position (focal plane of the laser beam leaving the fiber-outcoupler). From (2.3) we can then calculate the beam waist in the sample w'_0 with the aid of equation 2.2. The position of the objective with respect to the beam waist position z_l is unknown since the beam was adjusted in such a way that no divergence was detectable. While z_l determines the axial position of the focal spot in the sample, fortunately the dependence of w'_0 on z_l is very weak. Setting $z_l = 0$ m, which means that the beam waist would be at the position of the objective, yields $w'_0 = 0.295$ μm . z_l could not be measured but an estimate of its uncertainty can be given by estimating the uncertainty of the beam divergence. An assumed maximum divergence of 0.05 mrad causes z_l to change by 12 m, which in turn results in a reduction of the beam waist in the focal region by 9% ($z_l = 12$ m instead of $z_l = 0$ m). Since w'_0 cannot easily be measured, $w'_0 = 0.295$ μm is used as an estimate for the width of the focal spot in the further calculations. The calculated EID is shown in figure 2.3 (top)

where it has been truncated at the $1/e^2$ value. The plateau therefore represents its $1/e^2$ extension.

2.4.2 The Excitation Probability Distribution (EPD)

Usually, and if not otherwise noted also in this work, it is assumed that the probability to excite a fluorophore has a linear dependence on the excitation intensity. In this case The Excitation Propability Distribution (EPD) is directly proportional to the EID. In reality this linear dependence is not given if for example saturation effects have to be considered. Due to saturation the excitation probability of a fluorophore no longer depends linearly on the excitation intensity. Hence the EPD will differ (also in shape) from the EID. Saturation effects will be topic of section 3.5.1.

2.4.3 The Collection Efficiency Function (CEF)

For the calculation of the CEF, a semi-geometrical optical approach can be used [63]:

$$CEF(\rho, z) = \int_A \frac{disc\left(\frac{|\vec{\xi} - \vec{\rho}|}{w(z)}\right)}{\pi w^2(z)} d\vec{\xi}. \quad (2.5)$$

with $w(z) = w_0 \sqrt{1 + \left(\frac{z\lambda_{em}}{\pi w_0^2}\right)^2}$ and $w_0 = \frac{\lambda_{em}}{\pi \tan \Theta}$. *disc* denotes a step function, being unity for arguments smaller than one, and zero otherwise. λ_{em} is the center wavelength of the fluorescence emission, Θ is the maximum angle of light collection, defined by the objective's numerical aperture NA and the refractive index of the medium n as $\sin \Theta = NA/n$. The variables $\vec{\rho}$ and z are the coordinates of the emitter perpendicular and along the optical axis. The integration variable $\vec{\xi}$ is perpendicular to the optical axis, and the integration extends over the area A of the aperture's image in object space. For a circular aperture with radius a' and corresponding radius $a = a'/M$ in object space, the integration in equation 2.5 can be done analytically, leading to:

$$CEF(\rho, z) = \begin{cases} 0, & \rho \geq w + a \\ \max(a, w_0)^2 (\theta_1 a^2 + \theta_2 w^2 - \Delta) / (\pi a^2 w^2), & |w - a| < \rho < w + a \\ \max(a, w_0)^2 / \max(a, w)^2, & \rho \leq |w - a| \end{cases} \quad (2.6)$$

where the following abbreviations were used:

$$\begin{aligned}\theta_1 &= \arccos \left[\frac{a^2 + \rho^2 - w^2}{2a\rho} \right] \\ \theta_2 &= \arccos \left[\frac{w^2 + \rho^2 - a^2}{2w\rho} \right] \\ \Delta &= \frac{\sqrt{(a + \rho + w)(-a + \rho + w)(a - \rho + w)(a + \rho - w)}}{2}.\end{aligned}\tag{2.7}$$

Enderlein et al. [64] have shown that the semi-geometrical approach represented by equation 2.6 is an excellent approximation of the exact wave-optically calculated CEF which can be found in [65]. Figure 2.3 (center) shows the collection efficiency function. The mean difference between the shown semi-geometrical approach and the exact wave-optically calculated CEF is the absence of the plateau in the latter.

2.4.4 The Molecule Detection Function (MDF)

The Molecule Detection Function is the product of the EPD and the CEF. For the sake of simplicity (and for the unknown dependence of the EPD on the EID) we here assume that the EPD equals the EID, an not valid if saturation effects have to be acknowledged. Figure 2.3 (bottom) shows the MDF for the EID and CEF presented above. Usually, the MDF is approximated by a 3D Gaussian, which for example makes it possible to solve the diffusion correlation function analytically (see section 1.3). Therefore the 3D Gaussian approximation is shown alongside the semi-geometrically calculated MDF. The quality of this approximation is subject of chapter 3. Both MDFs are truncated at $1/e^2$. The plateau therefore represents the shape of the confocal volume.

2.5 Data Analysis

Collected photons were detected by Single Photon counting Avalanche Diode modules (SPADs) and analyzed by electronics for Time Correlated Single Photon Counting (TCSPC) [66, 67]. TCSPC basically records the arrival time with respect to a preceding laser pulse (micro time), the time from the start of the experiment (macro time) as well as routing information like detection channel and (if applicable) the image position for every detected photon.

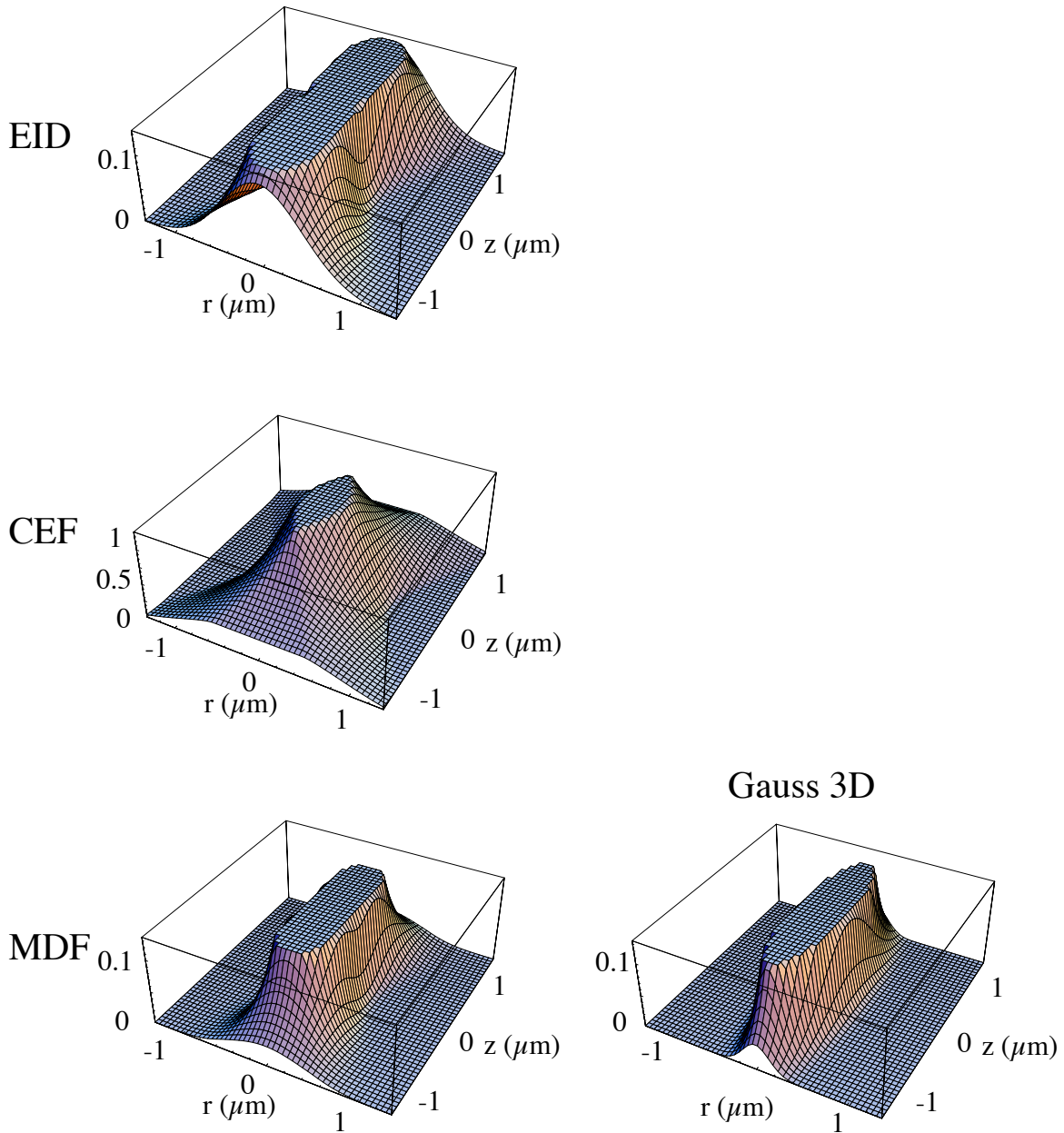


Fig. 2.3: Excitation Intensity Distribution (EID), Collection Efficiency Function (CEF), Molecule Detection Function (MDF) and its 3D Gaussian approximation. Note that except for the CEF, the z -axis has been cut at the $1/e^2$ value of its respective maximum. The flat area therefore represents the $1/e^2$ extension of the EID and the MDF respectively.

For the experiments of chapter 3 a PicoHarp USB-connected TCSPC box (PicoQuant GmbH, Berlin) was used. The Förster Resonance Energy Transfer (FRET) experiments of chapter 4 acquisition were done using a TimeHarp (PicoQuant GmbH Berlin) TCSPC PCI-board. The time resolution of the PicoHarp is 16 ps while the TimeHarp has a time resolution of 40 ps. The data was stored in the proprietary (but documented) Time Tagged Time Resolved (t3r) file format.

The main advantage of recording data in the `t3r` mode is that the complete temporal and spatial information of all photons detected is stored and a variety of possible analysis strategies can be applied to the very same data set. The `t3r` files are the basis for the different analyzing schemes briefly outlined in the following sections.

2.5.1 Image Analysis

The `t3r` file contains x, y and z coordinates of every detected photon, from which the actual image can be reconstructed. This has been done with the PicoQuant software available together with the acquisition system (MicroTime 200 (TimeHarp) and SymphoTime (PicoHarp) respectively). The images were then exported from the PicoQuant software in `bmp` format and loaded for further analysis into IgorPro (a scientific analysis program, similar to Origin from Wavemetrics, Portland USA). The 3D renderings of the confocal volume were done with MatLab (MathWorks, Massachusetts USA).

2.5.2 Instrument Response Function (IRF)

The lower limit of the time resolution for TCSPC measurements is ultimately given by the jitter of the TCSPC electronics. Practically the limits are however set by the jitter of the detector response and the excitation pulse duration. A measure of the time resolution of the measuring system is the Instrument Response Function (IRF). The IRF is measured as the response of the system to the excitation pulse. Figure 2.4 shows the IRF, recorded with a mirror placed on top of the microscope objective (instead of the sample). The reflected excitation light is attenuated by an OD3 neutral density filter whereas the bandpasses, used for fluorescence detection, are removed. The width of the IRF has been measured to be 0.54 ns (FWHM). The so-called diffusion tail (causing the asymmetry of the curve in figure 2.4) is a feature of all single-photon APDs and is caused by carrier generation in the

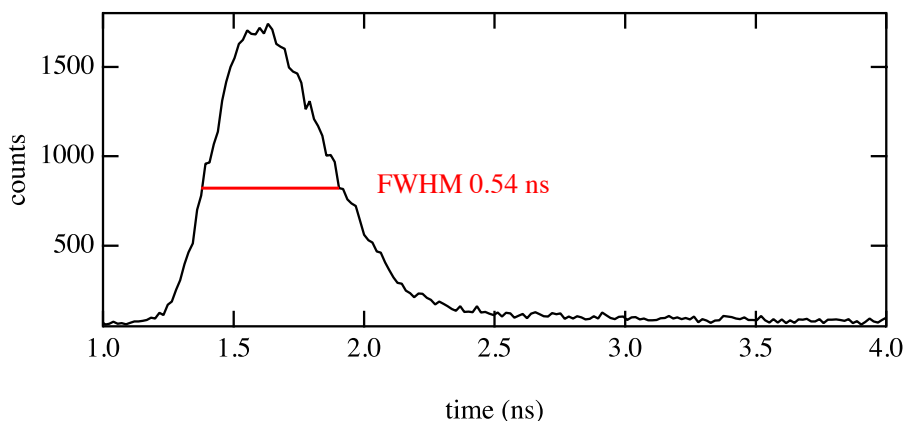


Fig. 2.4: Measured Instrument Response Function (IRF)

neutral layers below the avalanche region.

2.5.3 Fluorescence Correlation Spectroscopy

For Fluorescence Correlation Spectroscopy experiments fluorescence intensities were recorded over a time span of several minutes. Correlations were calculated using the PicoQuant software according to the algorithm published in [68]. Figure 2.5 shows a simplified scheme of the algorithm. The fluorescence intensity trace is obtained by binning the detected fluorescence photons and the correlation of the intensity trace is calculated as the product of the intensity trace at time t and the same intensity trace delayed by the lag time τ . Since the correlation curve is calculated for lag times ranging from nanoseconds up to seconds, the bin width is increased logarithmically with the lag time. For simplicity, the changing bin size is not shown in figure 2.5.

The calculated FCS curves were exported to an ASCII file and further analysis and fitting e.g. with the autocorrelation function was done in IgorPro and Origin (OriginLab, Massachusetts USA).

2.5.4 Determination of the Fluorescence Lifetime

As already mentioned, the `t3r` data files contain information about the time span between the exciting laser pulse and the detected photon (micro time). Fluorescence lifetime histograms are built up by histogramming the photon arrival times with respect to the excitation pulse. Depending on the experiment, histograms can be obtained individually for the different detec-

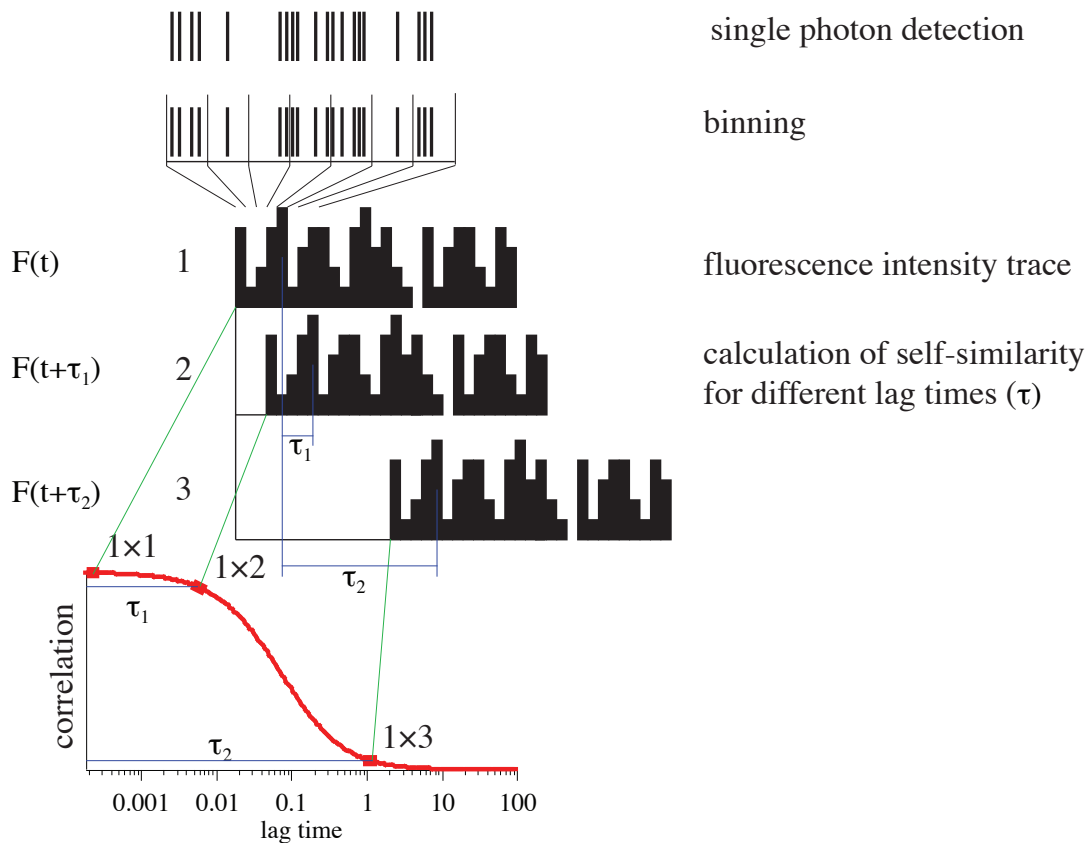


Fig. 2.5: Calculation of the FCS (autocorrelation) curve: Fluorescence intensity traces are obtained by binning the detected photons. The correlation is calculated as the product of the fluorescence fluctuations at every time t and the corresponding fluctuations at lag time $t + \tau$

tion channels (one lifetime histogram per detection channel). When using Pulsed Interleaved Excitation (PIE) as in chapter 4, additionally to the detection channels, different histograms are built up for the two excitation pulses used. The discrimination of fluorescence photons excited by the first or the latter pulse is done in the micro time range. If the fluorescence yield per burst exceeds some 100 photons, lifetime histograms of single bursts can be analyzed. Practically such high count rates have not been achieved in the FRET experiments discussed in chapter 4 and the burst-wise fluorescence lifetime analysis therefore will not be discussed further. The fluorescence lifetime can be extracted from the lifetime histogram by fitting with an exponential decay function. The fluorescence lifetime histograms are not only formed by fluorescence photons but also by scattered light from the excitation laser pulse. To measure short times, the lifetime histogram therefore has to be deconvoluted with the IRF.

During the fit process, an exponential decay function is convoluted with the measured

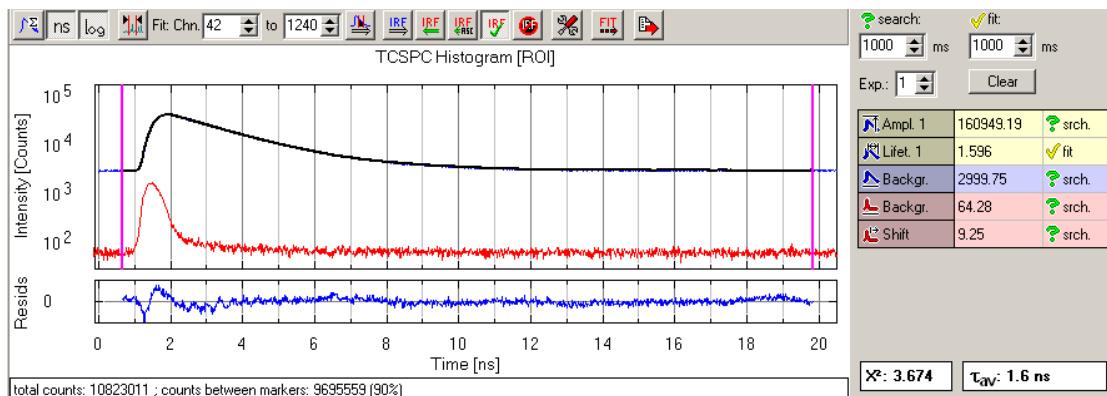


Fig. 2.6: Screenshot of the lifetime fitting routine of the PicoQuant SymphoTime Software. The top blue curve represents the fluorescence lifetime histogram, the red curve the IRF. The fit is shown in black and the residues are shown in blue at the bottom. The fitted parameters can be found on the right side.

IRF. The least square fit routine is then used to vary the parameters of the exponential decay function and finally yields the fluorescence lifetime(s) of the experimental curve. Besides the fluorescence lifetime, amplitude and background, another parameter is introduced, i.e. the shift between the IRF and the experimental lifetime histogram. Since measured in different experiments, IRF and fluorescence lifetime histograms may be shifted with respect to each other. This leads to uncertainties, since the relative temporal position of the IRF and the fluorescence signals are not known exactly. As a result, the uncertainty of the time zero is reflected in the determined fluorescence lifetime.

The fitting of the lifetime histograms was done with the SymphoTime Software, a screenshot of the fitting process is shown in figure 2.6. The sample in this case was a 5 nM aqueous ATTO-655 solution. When considering the IRF, the lifetime histogram could be fitted with a monoexponential decay function yielding a fluorescence lifetime of 1.6 ns for this dye solution, which is in accordance with literature [69].

2.6 Determination of the Confocal Volume by Imaging of Fluorescent Microspheres

An important parameter to characterize a confocal fluorescence microscope is the size and the shape of the confocal volume. One possibility to visualize the confocal volume is the imaging of fluorescent beads, smaller than the diffraction limited point spread function of the instrument. They can thus be treated as a point source.

Images of 100 nm diameter fluorescent beads (Tetra Spec from Molecular Probes, Eugene

USA) on a clean cover-slide were recorded. These fluorescent beads are labeled with various fluorophores and can thus be excited in a broad wavelength range. Due to the different fluorophores contained in the microspheres they undergo FRET and therefore also have a very broad emission spectrum and are therefore an all-purpose tool for the visualization of the confocal volume for a broad range of excitation and emission wavelengths. The confocal volumes presented in this chapter were measured with excitation at 635 nm, while detection was limited to (687 ± 35) nm. A $63 \mu\text{m}$ pinhole (diameter) was chosen and the laser power was $0.9 \mu\text{W}$, which allowed for continuous scanning without noticeable bleaching. A scanning speed of 0.6 ms per pixel gave about 600 counts in the center of the fluorescent bead.

First, an overview image was taken from which solitary spots with low fluorescence intensity were selected for further analysis. Selecting spots with low fluorescence intensity minimizes the risk of analyzing agglomerates, making it easier to subsequently fit the acquired sections with an appropriate model function. For the selected spots sectional scans were recorded. Additionally, stacks of xy-sections were acquired to allow for a 3D reconstruction of the confocal volume.

Figure 2.7a shows the measured iso-surface representations of the confocal volume. The image was reconstructed from a series of 46 xy-sections with a resolution of $0.02 \mu\text{m}/\text{pixel}$ while the distance between the sections is $0.1 \mu\text{m}$. The iso-surfaces shown in figure 2.7 represent the $1/e^2$ values of the maximum fluorescence intensity. For comparison, the usually approximated 3D Gaussian function (figure 2.7b) is depicted along with the measured MDF. The axial and lateral size of the calculated Gaussian MDF depicted in figure 2.7b was determined by fitting sections of the measured MDF. Comparing the measured MDF and its 3D Gaussian approximation we notice that the measured MDF is more elongated.

While the iso-surface images are very illustrative, it is more convenient to analyze sections of the MDF in the three spatial planes. An additional advantage is that these sections can be recorded faster than a complete xy-stack.

Figure 2.8 shows xy, xz and yz sections as contour plots. The contour lines indicate iso-intensity values of $(1/e^2)I_{max}$, $(1/2)I_{max}$ and $0.9I_{max}$, where I_{max} stands for the maximum fluorescence intensity in the respective plane. All sections were fitted with a 2D Gaussian function, asymmetry was permitted, but only along the principal axis of the sections. The sections are accompanied by line sections through the centers of the recorded planes and

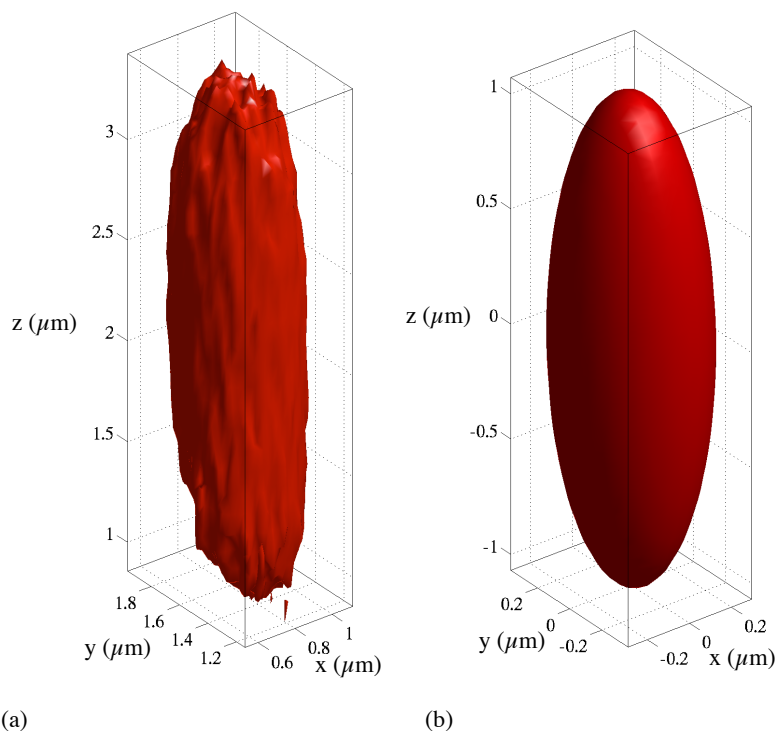


Fig. 2.7: Isosurface images of the confocal volume. (a) 3D reconstruction of the measured confocal volume. (b) 3D Gaussian representation of the measured confocal volume,

section	w_x	w_y	w_z
xy	0.278	0.342	
xz	0.308		1.07
yz		0.376	1.07
mean	0.292 ± 0.014	0.360 ± 0.018	1.07 ± 0.001

Tab. 2.2: Dimensions of the confocal volume in μm determined from 2D Gaussian fits of the section shown in figure 2.8. The resulting effective volume is (0.63 ± 0.06) fl.

their respective 2D Gaussian fits. Clearly the confocal volume is neither a 3D Gaussian nor has it rotational symmetry along the optical axis (z -axis). The asymmetry in the xy -section is due to the astigmatism of the excitation laser profile. This is a common effect if polarization maintaining fibers are used. The astigmatism of the excitation laser is probably also responsible for the distortions of the confocal volume visible in the yz -section (figure 2.8c). Unfortunately, the beam astigmatism is hardly recognizable in the collimated beam. It may become evident only in the focal region. Anyhow, all sections of the confocal volume were

fitted with a 2D Gaussian function¹:

$$I = I_0 + I_{max} \cdot e^{-2 \left[\left(\frac{x-x_0}{w_x} \right)^2 + \left(\frac{y-y_0}{w_y} \right)^2 \right]} \quad (2.8)$$

x_0, y_0 is the center of the section and w_x, w_y are the $1/e^2$ radii of the confocal volume in the fitted plane. I_{max} is the maximum fluorescence intensity of the bead. I_0 ideally should equal zero but has a small positive value due to background signal.

Table 2.2 shows the resulting lateral and axial dimensions, extracted from the three different sections of the confocal volume. The extension along each axis can be obtained from two different sections (i.e. w_x can be determined from the xy-section and the xz-section) the mean values of both extensions were calculated and are shown together with their standard deviation in table 2.2. The effective volume is then calculated from these mean values as

$$V_{eff} = \pi^{3/2} w_x w_y w_z = (0.63 \pm 0.06) fl \quad (2.9)$$

Although the shape of the sections is different from a 2D Gaussian, their shape can be approximated quite well by it. This is justified by the good reproduction of the line sections of the measured confocal planes by the line sections of their respective fits. The shape of the confocal volume and the experimental parameters that influence it will be subject of a more detailed discussion in section 3.5.

¹ For the xz- and yz-sections x, y and w_x, w_y have to be replaced by the appropriate variables.

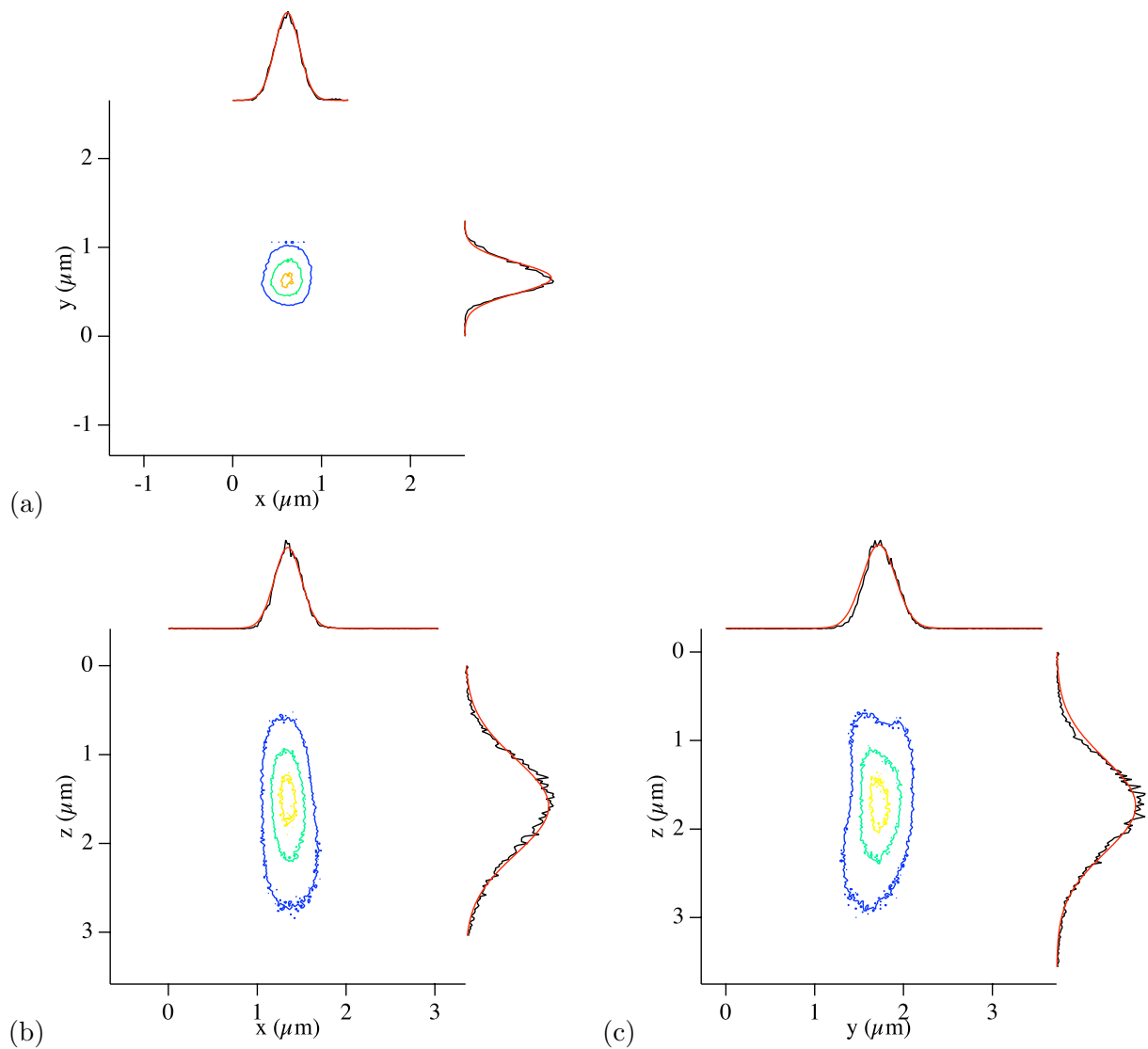


Fig. 2.8: Different sections of the confocal volume, measured on 100 nm TetraSpec beads. (a) xy-section, orthogonal to the optical axis (b) xz-section and (c) yz-section. The contour lines represent 90%, 50% and 13.5% of the maximum intensity. Along with the 2D sections line profiles through the center-positions are shown. Experimental values are shown as black lines whereas line sections of the 2D Gaussian fits are represented by red lines.

3. FLUORESCENCE CORRELATION SPECTROSCOPY - CONFOCAL VOLUME, CONCENTRATION, MOLECULAR BRIGHTNESS AND ARTIFACTS

Single molecule techniques, especially in combination with fluorescent labels offer the possibility to gain not only qualitative but also quantitative insight into the function of complex biological systems.

Historically confocal single molecule detection was developed out of Fluorescence Correlation Spectroscopy (FCS). In FCS, the fluctuations of the measured fluorescence signal are exploited for analysis. Significant fluctuation amplitudes occur when the number of molecules that are simultaneously present in the detection volume is small. FCS is therefore targeted at detection and analysis of single or few molecules. The first single molecule detection with a FCS setup was reported by Rigler et al. [57]. Afterwards this approach has become quite popular due to its relative simplicity [11, 22]. Nowadays FCS is a single molecule detection and analysis method with ever increasing importance for life sciences. It is mostly applied to determine the diffusion coefficient of the fluorescent species but also to gain insight into molecular photophysics [70–73], to monitor conformational changes [71, 74, 75] and chemical reactions [73, 76, 77]. Examples of quantitative FCS measurements include the *in vivo* determination of RNA concentrations in a single bacterium [78], the investigation of molecular concentrations and mobility in cells and membranes [79], or the study of binding kinetics of RNA comprising on the primer binding site of HIV-1 reverse transcriptase [80]. FCS has also found its application in Polymerase Chain Reaction (PCR), where it is used to reflect amplification kinetics [81]. These are just a few randomly chosen examples from a vast field of applications of FCS.

The basic necessity for quantitative FCS measurements in particular but also commonly for all quantitative single molecule experiments is the precise knowledge of the experimental conditions.

It is the scope of this chapter to evaluate different methods to acquire information about the performance of the confocal microscope. This is not only necessary to control potential sources of systematic errors and to optimize the set-up but also to achieve comparability between experiments performed e.g. on different days. Hence, the control of the experimental conditions is a key parameter to achieve reliable and comparable results. In particular, it is a prerequisite to foster quantitative approaches and analytics in biology e.g. to gain much deeper insight into function and dynamics of biological systems.

In single molecule experiments the characterization of experimental conditions, is not easily done due to the complexity of the setup and the difficulties involved in the acquisition of such parameters.

For confocal microscopy important system parameters are spatial resolution in 3D and detection efficiency. The determination of these parameters is problematic, as they not only rely on the experimental setup itself but also on the sample properties (e.g. the medium or the fluorophores used). It is therefore desirable to measure both parameters on the sample itself, or, if this is not possible, at least on a comparable model system.

The spatial resolution of a confocal fluorescence microscope is usually described by the confocal volume, that is the excitation volume folded with the detection volume. It depends on the Excitation Intensity Distribution (EID) as well as the Collection Efficiency Function (CEF) of the fluorescence emission (see section 2.4.4). To further complicate matters it also depends on sample properties like the refractive index of the sample containing medium, the photo-physics of the fluorophore, cover slide thickness and other experimental conditions.

The detection efficiency of a confocal fluorescence microscope is difficult - if not impossible at all - to be measured independently from the excitation efficiency of the fluorophore. Therefore, a parameter called molecular brightness is introduced to characterize the overall detection efficiency of a certain fluorophore in a particular setup. The characterization of molecular brightness and the confocal volume is a necessity also for the nm distance determination on single molecules, which will be the topic of chapter 4.

In the following it will be shown that Atto-655 is a well-suited fluorophore for the determination of the mentioned parameters. Furthermore, the molecular brightness is an easily accessible parameter to control changes in the mentioned parameters of the instrument on a day to day basis.

3.1 Sample Preparation and Experimental Details

The measurements were performed on a MicroTime 200 confocal microscope (PicoQuant, Berlin, Germany). A description of the setup can be found in section 2.3. In particular, a 635 nm pulsed laser diode with a repetition rate of 40 MHz (LDH-P-635) was used for excitation. The laser beam passed an adjustable attenuator and was coupled via a single mode fiber into the main optical unit. There, the beam was directed via a dichroic mirror (z467/638pc) into the Olympus IX71. The fluorescence emission passed the dichroic mirror, an emission filter (HQ687/70) and was focused on a pinhole. Pinholes with three different diameters (37 μm , 63 μm and 93 μm) were used. For saturation and dilution measurements, the pinhole size was 63 μm . Afterwards the fluorescence light was divided via a 50/50 beam splitter and focused onto two SPCM-AQR Single Photon counting Avalanche Diode modules (SPADs).

For bead scanning, 100 nm fluorescent microspheres (TetraSpeck, Invitrogen) were immobilized by drying of the bead solution on a clean cover-slide. An area with a small particle density was selected and images of the spots with the weakest fluorescence were recorded. The scanning resolution was 20 nm/pixel. For stack recording, a distance of 100 nm between consecutive xy-sections was chosen.

FCS measurements were performed on aqueous solutions of Atto-655 (ATTO-TEC, Siegen, Germany). The measurements (normally 5 min. measuring time) were conducted 20 μm above the cover slide surface. The signal was divided with a 50/50 beam splitter and two detectors were used to calculate the cross-correlation¹ of the detected fluorescence signal, as described in section 2.5.3.

The dilution series was prepared by subsequently diluting with triple distilled H₂O by pipetting. The initial concentration was measured spectroscopically with an UV-160A UV-Vis absorption spectrometer (Shimadzu) and found to be $(3.8 \pm 0.2) \mu\text{M}$. This stock solution was diluted to 1 μM for the sake of even numbers. To prevent aggregation and surface adhesion 0.5 ‰ Tween 20 (a detergent polysorbate) was added to the solvent. To further minimize surface adsorption pipetting volumes were kept relatively large (typically above

¹ The cross-correlation is not affected by detector noise or afterpulsing since the noise and afterpulsing probability of detector 1 is not correlated with the noise and afterpulsing probability of detector 2. The interpretation of the resulting FCS is therefore considerably facilitated.

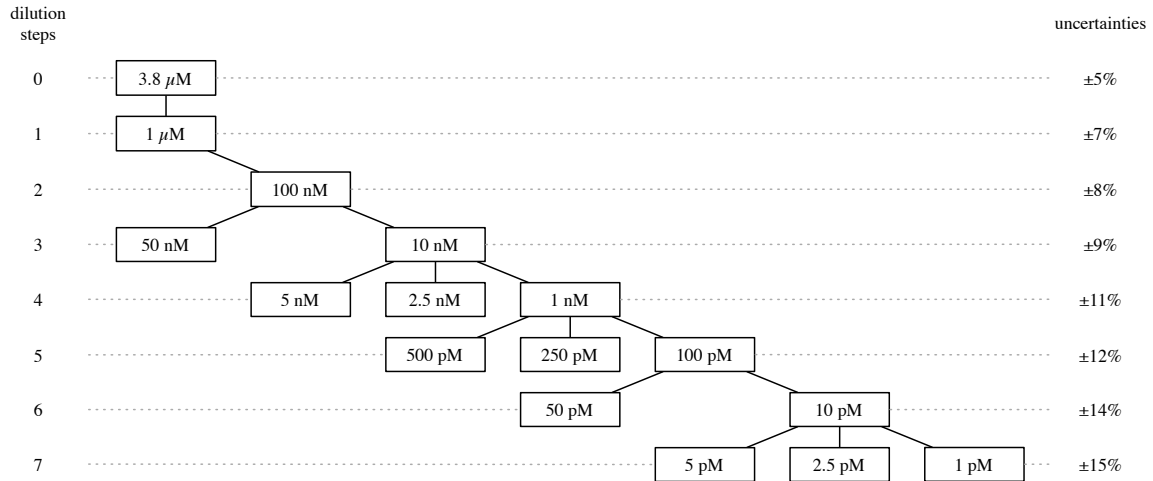


Fig. 3.1: Dilution scheme. Dilution involved 1:10-, 1:4- and 1:2-dilution steps. For example the 5 nM sample was produced by 1:2-dilution of the 10 nM sample, whereas the 100 pM sample was produced by 1:10 dilution of the 1 nM sample.

100 μ l) and polypropylene tubes (Plastibrand, Brand, Wertheim Germany) were used as sample containers. The dilution was done subsequently according to the scheme depicted in figure 3.1. Uncertainties of the different sample concentrations increase with the number of dilution steps involved. The uncertainties given in figure 3.1 were calculated according to the inaccuracies of the pipettes (given by the manufacturer).

For the measurements the sample was pipetted into the cap of a polypropylene tube (approximately 80 μ l) and put onto a cover slide (see photo in figure 3.2). This geometry is very favorable since it reduces sample evaporation and therefore changes in the concentration during the experiment can be neglected². Because disposable materials were used, every experiment could be performed with a new cover-slide and cap, hence sample diversion due to improper cleaning of containers was eliminated.

3.2 Measuring the Confocal Volume with FCS

FCS analysis itself has been used to measure the confocal volume [8]. The advantage thereof is, that it can be measured under the same conditions as the experiment of interest.

There are two different approaches to determine the confocal volume using FCS. If the signal fluctuations are due to diffusion only, the amplitude of the auto- or cross-correlation equals the inverse number of fluorescent molecules on average present in the effective volume,

² This was confirmed by verifying that the fluorescence count rate stayed constant during the measuring time and by FCS concentration measurements at the beginning and end of the data acquisition.

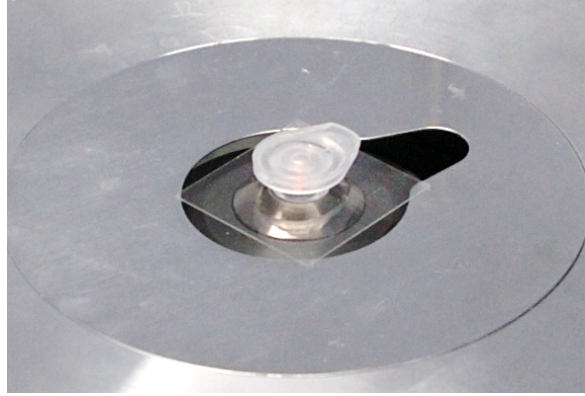


Fig. 3.2: Measuring geometry for solution measurements. The sample is contained in the plastic cap and placed onto a cover slide.

while the devolution of the correlation for increasing lag times depends on the size and shape of the effective volume.

Please note, that the term effective volume (V_{eff}) will be used here, which is not identical to the confocal volume (V_{conf}) (see section 1.3.2). If of 3D Gaussian shape, the effective volume is by a factor of $2^{3/2}$ larger than the confocal volume:

$$V_{conf} = \left(\frac{\pi}{2}\right)^{3/2} w_0^2 z_0 = \left(\frac{1}{2}\right)^{3/2} V_{eff}. \quad (3.1)$$

w_0 is the lateral and z_0 the axial $1/e^2$ -radius of the confocal volume. It is common to express z_0 in terms of $z_0 = kw_0$ with k referred to as the eccentricity of the confocal volume.

The first approach to determine the effective volume (and therefore the confocal volume) is to measure the correlation amplitude of a sample with known concentration, as the effective volume can be calculated by:

$$V_{eff} = \frac{1}{G_0 N_A c}, \quad (3.2)$$

where G_0 is the correlation amplitude at zero lag time (i.e. $\tau = 0$, equation 1.35), c the sample concentration in molar units and $N_A = 6.022 \times 10^{23} \text{mol}^{-1}$ is Avogadro's number. The advantage of this approach is the independence of a model if no additional fast fluctuations (e.g. caused by triplet transitions, protonation/deprotonation) are present. No assumptions about the shape of the confocal volume need to be made, as G_0 can be extracted without any fitting procedure.

The second approach relies on the assumption, that the confocal volume can be approximated by a 3D Gaussian shape. In this case the autocorrelation function can be calculated analytically (see section 1.3):

$$G(t) = G_0 \cdot \left(1 + \frac{t}{\tau}\right)^{-1} \cdot \left(1 + \frac{t}{k^2\tau}\right)^{-1/2}. \quad (3.3)$$

τ is the lag time for which the correlation has dropped to half of its maximum, the time a molecule on average needs to transverse the confocal volume by diffusion. τ is connected with the lateral extension of the confocal volume by the diffusion coefficient D :

$$w_0^2 = 4D\tau, \quad (3.4)$$

hence

$$V_{conf} = \left(\frac{\pi}{2}\right)^{3/2} k (4D\tau)^{3/2}. \quad (3.5)$$

Thus, with a known diffusion coefficient the size of the confocal volume can be extracted by fitting the correlated data with equation 3.3. Knowledge about the concentration of the sample is not necessary. Moreover the concentration can be directly obtained by the FCS analysis in this case, since the number of molecules within the confocal volume can be determined from G_0 .

3.2.1 Dilution Series

At first, the determination of the confocal volume by analyzing the fluorescence correlation of a sample with a known concentration will be discussed. For this purpose the number of particles in the confocal volume was analyzed via G_0 for a Atto-655 dilution series covering six orders of magnitude, from 1 μM to 1 pM .

The preparation of this dilution series is described in section 3.1, where also a description of the experimental setup can be found. The acquisition times for the different samples were 5 to 10 minutes each, depending on the sample concentration (shorter acquisition times for higher concentrations). The cross-correlation was calculated according to section 2.5.3 using the SymphoTime Software.

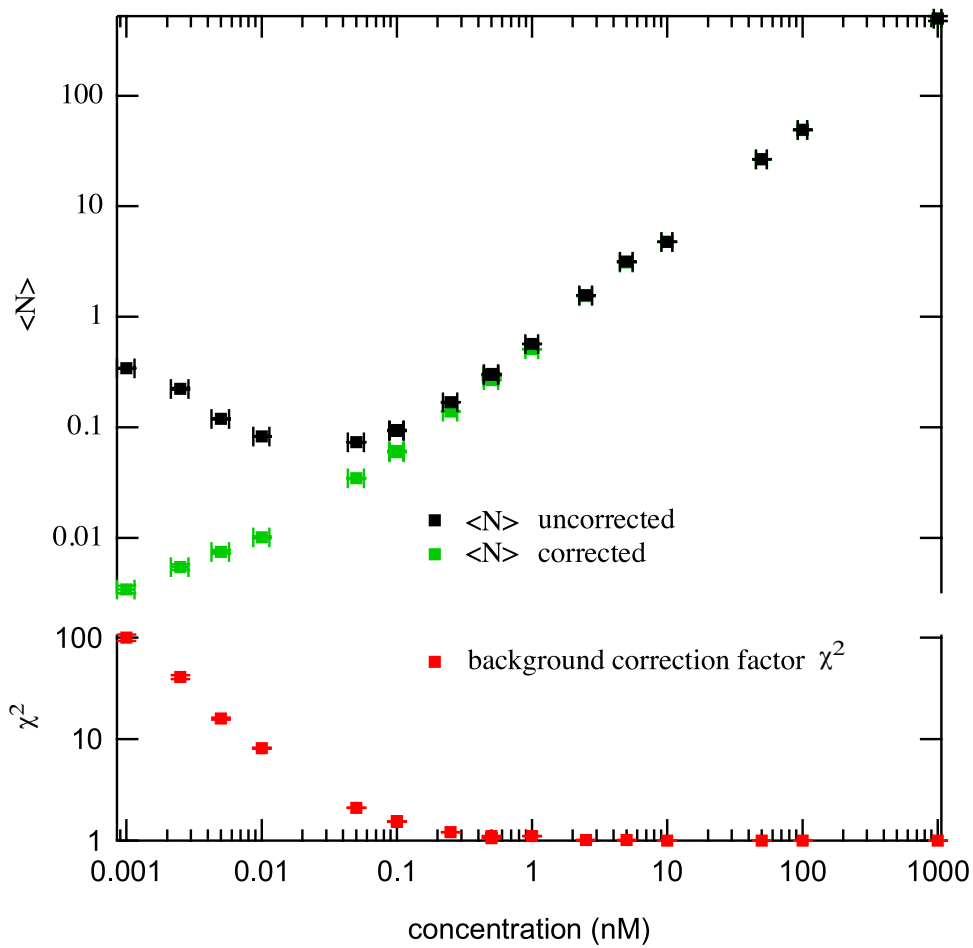


Fig. 3.3: Dilution series of Atto-655 in H_2O : Top: apparent number of particles (black squares) and background corrected number of particles (red squares). Bottom: background correction factor χ^2 .

Figure 3.3 shows the particle numbers extracted from the correlation amplitudes for the different sample concentrations measured. Note that both axis have logarithmic scales to cover the large concentration range measured. The black squares are the apparent numbers of particles calculated as $\langle N_{app} \rangle = 1/G_0$, while the green squares are the numbers of particles calculated considering the influence of uncorrelated background signal.

A linear dependence between the average number of particles and the concentration is expected with the slope giving the effective volume. While $\langle N_{app} \rangle$ (black squares) first decreases with decreasing sample concentration this trend is inverted for low concentrations. The increase at low concentrations is caused by the increasing contribution of the uncorrelated background signal. As uncorrelated background signal becomes more prominent at low sample concentration, damping of the correlation amplitude occurs (see section 1.3.3 or refer-

ence [56]). This reduction of the correlation amplitude apparently leads to a higher particle concentration. The damping of the correlation amplitude has to be taken into account if the signal to background ratio is low, which is the case for the samples with a concentration below 1 nM. The influence of the uncorrelated background on the correlation amplitude can be considered through a correction factor χ^2 as described in section 1.3.3:

$$\frac{1}{\chi^2} = \frac{1}{(1 + \langle b \rangle / \langle f \rangle)^2}. \quad (3.6)$$

$\langle b \rangle$ is the average background count rate measured on a sample containing blank solvent, and $\langle f \rangle$ is the count rate of the actual sample, reduced by the background count rate ($\langle f \rangle = \langle F \rangle - \langle b \rangle$). As can be seen in figure 3.3, χ^2 increases with decreasing concentration. Considering the influence of this uncorrelated background, the number of particles present on average in the effective volume can be calculated according to the following equation (see sec. 1.3.3):

$$\langle N \rangle = \frac{1}{\chi^2 G_0}. \quad (3.7)$$

The background corrected particle numbers $\langle N \rangle$ are shown as green squares in figure 3.3. A more or less linear dependence on the sample concentration down to a concentration of 50 pM is obtained.

It is worth noting that $\langle N \rangle$ can be determined with high accuracy as shown in figure 3.4. For sample concentrations between 50 pM and 100 nM the uncertainties are below 1%. The accuracy of the concentration determination however is limited by the accuracy of the measurement of the effective volume.

To get a measure of the linearity of the dilution series the logarithm of $\langle N \rangle$ was calculated and plotted versus the logarithm of the pipetted sample concentration. The slope of a linear fit yields the exponent of the dependence, which for a linear function is expected to be 1. The exponent found for the dilution series is 0.97 ± 0.01 , indicating almost linear behavior.

Unfortunately for the two highest concentrations, the excitation power had to be reduced to prevent detector saturation. Since the excitation power influences the size of the effective volume (see section 3.5.1), only concentrations smaller than 100 nM were fitted and are shown in figure 3.5. In this concentration region a logarithmically weighted fit yields an

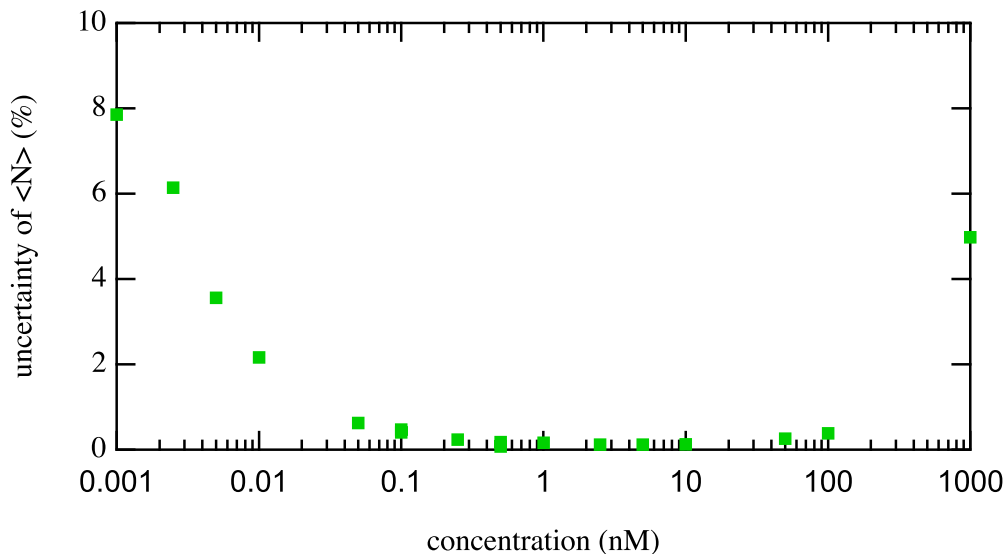


Fig. 3.4: Dilution series of Atto-655 in H₂O: Relative uncertainties of the background corrected numbers of particles, $\langle N \rangle$, for the dilution series shown in figure 3.3.

effective volume of (0.98 ± 0.03) *fl* and an offset of $(3.00 \pm 0.03) \times 10^{-3}$. The weighting was applied because, due to the logarithmically varied concentrations, ordinary fitting tends to overweight higher concentrations. The offset can be explained as originating from impurities in the solvent, most probably stemming from Tween 20. If we speculate, that the offset is due to impurities with the same molecular brightness as Atto-655, it would correspond to a concentration of 6.3×10^{-13} M.

To get an idea of the errors that might be caused by potential sample loss, experimental data were fitted additionally in two different concentration regions. For concentrations above 1 nM ($5 \text{ nM} \leq c \leq 50 \text{ nM}$) an unweighed linear fit yields an effective volume of (0.88 ± 0.01) *fl* while for concentrations below 100 pM an effective volume of (1.06 ± 0.03) *fl* is found. The effective volume seems larger for smaller concentrations. This can be explained by sample loss due to adsorption on pipette tips and container walls. The uncertainties of the mentioned effective volumes do not include the uncertainties caused by the sample preparation. For the smallest sample concentration the uncertainties can reach 15%. For the higher concentrations these uncertainties are lower, therefore the extracted effective volume in the high concentration region is considered to be most trustworthy.

The effective volume determined from the complete dilution series (omitting the two highest concentrations) is (0.98 ± 0.03) *fl*. The uncertainty, however, needs to be raised due

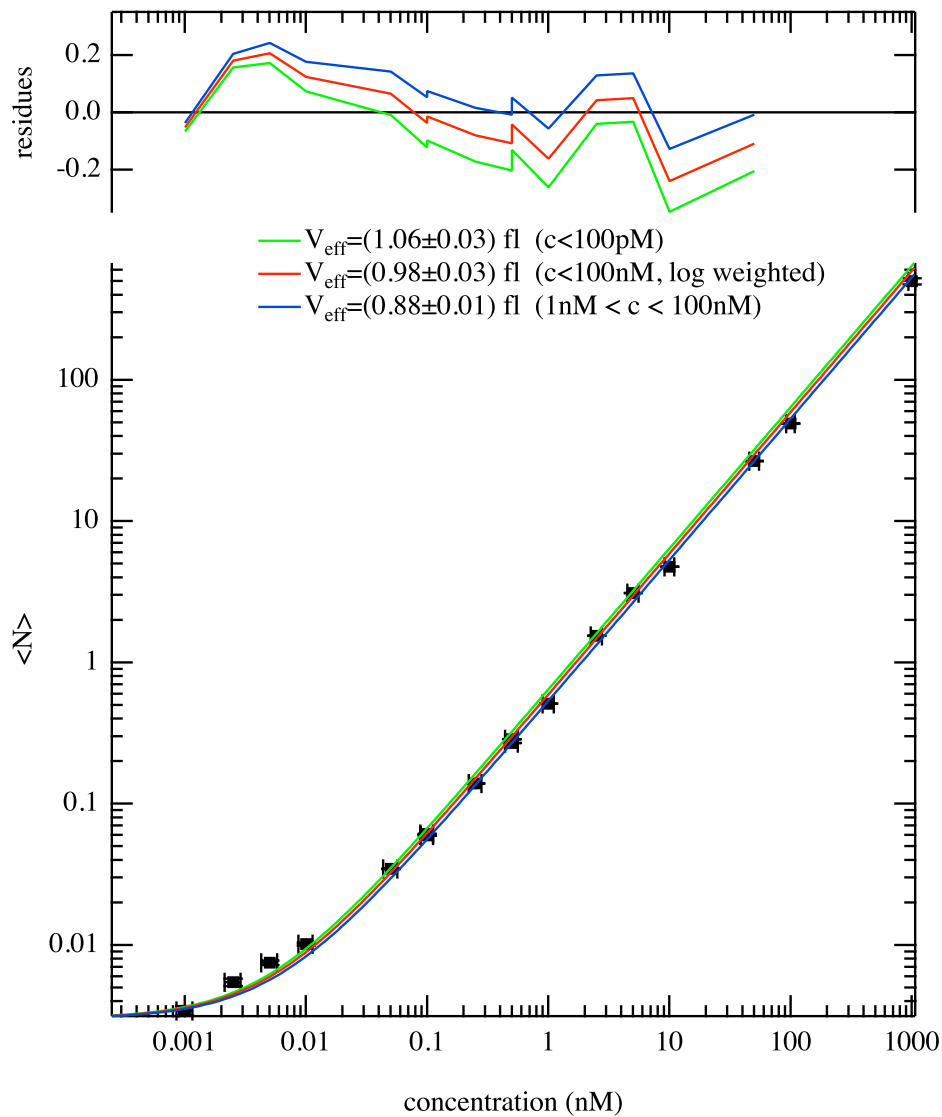


Fig. 3.5: Dilution series of Atto 655 in H_2O : Different linear fits and their relative deviations from the measured particle numbers (top).

to the uncertainties of the sample pipetting and potential sample loss due to adsorption. Therefore the effective volume resulting from the dilution series is $(1.0 \pm 0.1) \text{ fl}$

For comparison the effective volume has also been measured by imaging fluorescent microspheres immediately before the FCS measurements (see also section 2.6). The resulting effective volume was $(1.0 \pm 0.1) \text{ fl}$.

3.2.2 Determination of the Confocal Volume from the FCS Fit

As mentioned, the lateral and axial dimensions of the confocal volume can be extracted from the fit of the fluorescence correlation data. If a fluorophore with a known diffusion coefficient

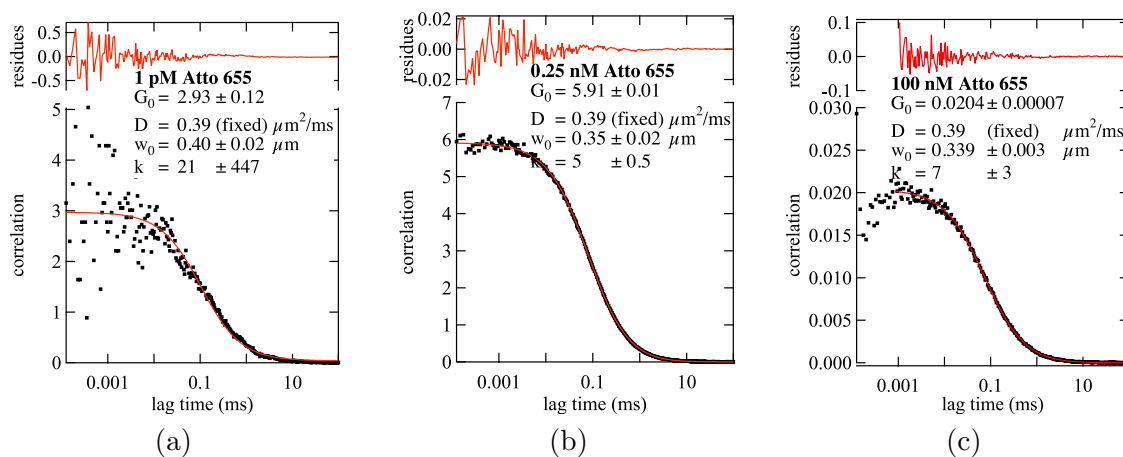


Fig. 3.6: Fluorescence correlation spectra of three different dilutions of Atto 655 (black squares) and their respective fits (red curves).

is used (and assuming that the confocal volume can be approximated by a 3D Gaussian function), the dimensions of the confocal volume can be obtained by fitting the following function to the correlation curves:

$$G(\tau) = G_0 \cdot \left(1 + \frac{4Dt}{w_0^2}\right)^{-1} \cdot \left(1 + \frac{4Dt}{k^2 w_0^2}\right)^{-1/2} + C_0. \quad (3.8)$$

The diffusion coefficient D was fixed³ to $0.39 \mu\text{m}^2/\text{ms}$. The introduction of C_0 accounts for certain statistic variations and yields a more reliable fit. It must be noted however, that C_0 was found to be by 3 orders of magnitude smaller than the correlation amplitudes, but always with an uncertainty of more than 100%. The introduction of C_0 is therefore only a means of stabilizing the fit process but does not change the resulting parameters. Figure 3.6 shows three example correlation curves together with their respective fits. The dropping of the correlation amplitude observable in figure 3.6c for lag times below 0.001 ms is probably caused by the dead-time⁴ of the SPADs. The fits reproduce the correlated data well for all three concentrations, but already the amplitude of the G_0 -normalized residues reveal the variation of the fit quality for the different concentrations. Analyzing the resulting parameters, it turns out, that for the 1 pM sample the eccentricity of the confocal volume determined by the fits is $k = 21 \pm 447$ whereas expected values fall between 2 and 6, indicating that the fit is unable

³ The diffusion coefficient of Atto 655 has been measured with two focus FCS and compared to Nuclear Magnetic Resonance (NMR) findings by Thomas Dertinger et al. In water, the diffusion coefficient has been found to equal $(0.39 \pm 0.01) \mu\text{m}^2/\text{ms}$ [62]

⁴ The time to quench the avalanche evoked by the detection of a photon and subsequent recharging of the diode to its normal bias is termed "dead-time" as during this time span no further photons can be detected.

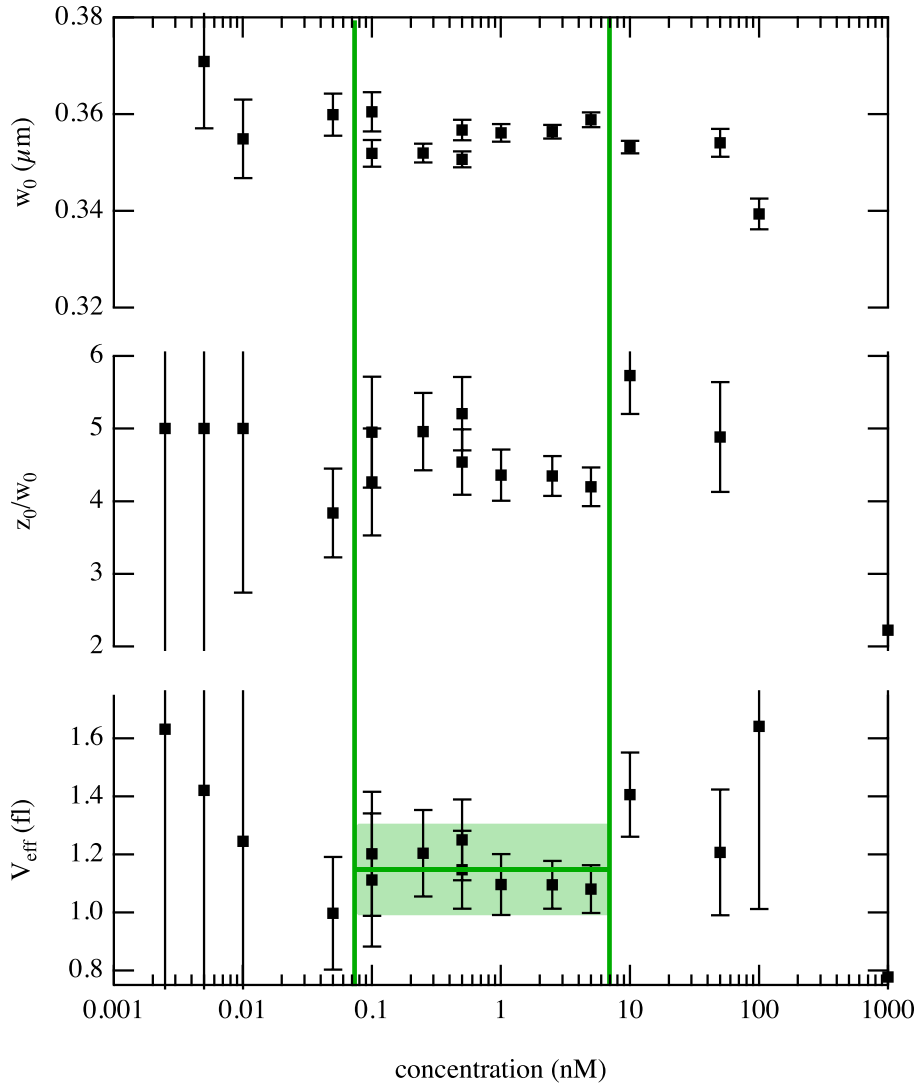


Fig. 3.7: Dilution series of Atto-655 in H_2O : Beam waist ($1/e^2$), eccentricity $k = z_0/w_0$ and resulting effective volume found by fitting the correlated data with the autocorrelation function for pure diffusion and a 3D Gaussian confocal volume.

to yield reasonable values for the shape of the confocal volume. For 100 nM the uncertainty of the eccentricity determined is high as well ($k = 7 \pm 3$), while for 0.25 nM all parameters of the fit could be acquired with reasonable uncertainties ($w_0 = (0.35 \pm 0.02) \mu\text{m}$, $k = 5 \pm 0.5$). The examples shown in figure 3.6 indicate that the quality of the parameters that can be extracted by fitting with the autocorrelation function vary dramatically depending on the sample concentration.

Figure 3.7 shows the lateral $1/e^2$ radii w_0 , the eccentricities k and the resulting effective volumes for sample concentrations between 1 pM and 1 μM . All three parameters are expected to be constant since they should only depend on the experimental setup but not on the sample

concentration.

From equation 3.8 it becomes evident, that k can only be extracted with a relative high uncertainty since its contribution to the shape of the correlation function is rather small. k is also strongly correlated to w_0 , making it difficult to find both parameters with sufficient accuracy, especially if the correlation curve becomes noisy. As can be seen in figure 3.7, the uncertainty for k increases strongly for low and high concentrations. At low concentrations this is due to poor statistics and for high concentration due to the low correlation amplitude. If the average number of molecules contained in the confocal volume is high, fluctuations due to entering and leaving molecules are low and become more and more difficult to observe. For the 100 nM sample the correlation amplitude is only 0.02. The correlation amplitude drops from this value to zero on a time scale of about 4 orders of magnitude. The dependence of the correlation function on the lag time is very weak and the fit parameters are therefore difficult to extract. Only in the range of 0.1 nM to 5 nM the fits yield reasonable values with acceptable uncertainties for the eccentricity. The uncertainties for w_0 are smaller and the trustworthy concentration region lies between 0.05 nM and 10 nM. For the determination of the effective volume from both, w_0 and k , however, the concentration region of confidence is smaller, i.e. between 0.1 nM and 5 nM. This region is indicated by the vertical lines in figure 3.7. The average effective volume in this concentration region is (1.15 ± 0.15) fl, as indicated by the horizontal line in figure 3.7.

3.3 Determination of the Diffusion Coefficient using the Confocal Volume

Parameters acquired by Imaging of Fluorescent Microspheres

As the Molecule Detection Function (MDF) can be easily measured by scanning fluorescent microspheres, the confocal volume can also be determined in a separate experiment. Then, knowing the lateral extension of the effective volume w_0 , and assuming that the MDF of the bead experiment equals the MDF of the FCS experiment, the diffusion coefficient D can be calculated from the fitted diffusion time ($D = w_0^2/(4\tau)$, equation 3.4). Substituting equation 3.4 in equation 3.8 we get the fit function for the diffusion time:

$$G(t) = G_0 \cdot \left(1 + \frac{t}{\tau}\right)^{-1} \cdot \left(1 + \frac{t}{k^2\tau}\right)^{-1/2} + C_0. \quad (3.9)$$

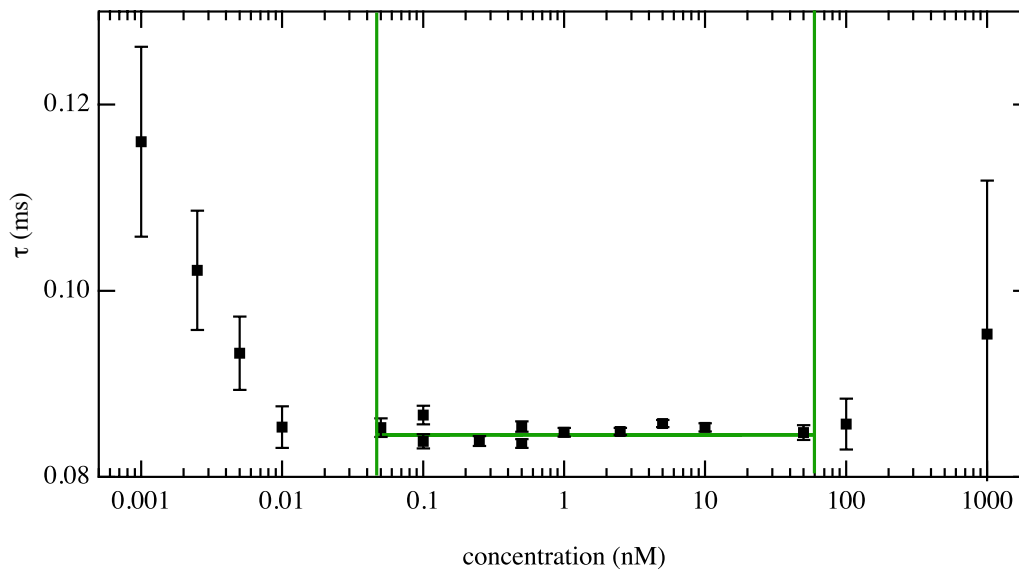


Fig. 3.8: Dilution series of Atto-655 in H_2O : Diffusion times from FCS fits. The green vertical lines mark the trustworthy concentration region, while the horizontal green line symbolizes the average diffusion time within this region.

By imaging the confocal volume with fluorescent microspheres (see section 2.6) we found ($w_0 = 0.38 \pm 0.02$) μm and $k = 3.2 \pm 0.2$. Therefore, for the fit of the correlated data k was kept constant at 3.2. The fit yields the diffusion time τ , which is plotted in figure 3.8 for the different concentrations of the dilution series.

The average diffusion time of the samples within the trustworthy concentration region between 50 pM and 50 nM is $\tau = 0.0849 \pm 0.0009$ ms . According to equation 3.4 this diffusion time yields an diffusion coefficient of $D = (0.42 \pm 0.04)\mu m^2/ms$. Dertinger et al. measured the diffusion coefficient of Atto-655 with two-focus FCS and NMR and found a diffusion coefficient of $D = 0.39 \pm 0.01$) $\mu m^2/ms$ [62]. Concerning the uncertainties we find both values in good agreement.

3.4 The Molecular Brightness

As many factors influence the confocal volume, the need of a simple parameter in order to calibrate, compare and optimize system performance is evident. The molecular brightness is such a parameter. On its own, the molecular brightness has been exploited in two fluctuation analysis methods, PCA or PCH (Photon Counting Analysis [82–84] or Photon Counting Histogram) and Fluorescence Intensity Distribution Analysis (FIDA) [85–87].

The average fluorescence intensity measurement in solution is [88]:

$$\langle \tilde{F} \rangle = \phi_{ex} \cdot \langle N \rangle \cdot \sigma Q, \quad (3.10)$$

with σ being the absorption cross section at the given excitation wavelength, Q the quantum yield and $\langle N \rangle$ the average number of molecules in the confocal volume. ϕ_{ex} is the photon flux density of the excitation laser which can be determined from the laser power measured behind the microscope objective, $P_{ex} = \phi_{ex} h\nu A$, where A is the cross sectional area of the incident laser beam at the focus and $h\nu$ the energy of the incident photons.

In practical terms, the limited Collection Efficiency Function (CEF, see section 2.4.3) and the detection efficiency g determines the measured fluorescence.

$$\langle F \rangle = CEF \cdot g \langle \tilde{F} \rangle. \quad (3.11)$$

As the laser power P , the total count rate $\langle F \rangle$ and the number of molecules $\langle N \rangle$ can be measured, the count rate per molecule and laser power, which we here define as the molecular brightness β , is a well suited parameter for comparison of instrument performance and quality of adjustment: If the system is not optimally aligned, the excitation or the emission will not be as efficient, and the molecular brightness will drop.

$$\beta = \frac{\langle f \rangle}{\langle N \rangle P_{ex}} \quad (3.12)$$

$\langle f \rangle = \langle F \rangle - \langle b \rangle$ is the count rate reduced by the background count rate, which can be measured on a pure solvent solution. My definition is different from the one given by Chen et al. [82]. Chen et al. use the photon count rate of a single molecule (λ):

$$\lambda = \frac{\langle k \rangle}{\langle N \rangle T}, \quad (3.13)$$

where k is the number of detected photons and T is the sampling time ($\langle k \rangle = \langle f \rangle T$). For Sanchez-Andres et al. [89], the brightness ϵ characterizes the number of photons received per

concentration (nM)	pinhole diameter (μm)			beam waist (mm)	
	37	63	93	2.37	1.02
0.25	0.14	0.42 ± 0.06	0.48	0.42 ± 0.06	0.16
0.5	0.15	0.41 ± 0.04	0.48	0.41 ± 0.04	0.16
1.0	0.17	0.39 ± 0.06	0.48	0.39 ± 0.06	0.16

Tab. 3.1: Left: the molecular brightness $\langle\beta\rangle$ (in counts per ms, molecule and μW) for different confocal pinhole diameters measured with an excitation beam waist of 2.37 mm. Right: Comparison of molecular brightness for different beam waists, measured with the 63 μm pinhole.

molecule for a sampling time T . In the short sampling time limit it is proportional to λ :

$$\epsilon = \lambda T. \quad (3.14)$$

ϵ therefore explicitly depends on the sampling time. λ is independent of the sampling time but still depends on the excitation power. Still another possibility would be to normalize the molecular brightness not with the average laser power as done in the definition of β but with the laser power per focal area. This would make the molecular brightness independent of the excitation and thus only dependent on the molecular properties and detection efficiency (β changes with the excitation beam waist). However the focal area is not an experimentally accessible parameter and therefore not a good normalization parameter.

Note, that despite its name, the molecular brightness is not a molecular property. β is proportional to the molecular properties σ and Q , the Excitation Propability Distribution (EPD) (or, if neglecting optical saturation, the EID) and the detection efficiency, which is a parameter of the setup. The molecular brightness is a combined parameter measuring the number of detected photons per time, laser power and molecule of a specific fluorophore and a specific experimental setup. Although being a parameter depending on sample and setup properties, $\langle\beta\rangle$ is well suited as a calibration parameter. It can be used to compare the brightness of different dyes on the same setup or of the same dye on different setups / different alignments.

To illustrate the influence of the experimental conditions, molecular brightness for different pinhole diameters (different CEFs) and different excitation beam waists (different EIDs) were measured. The sample was an aqueous Atto-655 solution with concentrations between 250 pM and 1 nM, excitation power was 89 μW . Note that the determination of the molecular

beam waist	w_x	w_y	$w_{x,y}^{calc}$	w_z	w_z^{calc}	V_{eff}	V_{eff}^{calc}
<i>mm</i>	μm	μm	μm	μm	μm	<i>fl</i>	<i>fl</i>
2.37	0.29 ± 0.01	0.36 ± 0.02	0.289	1.07 ± 0.08	0.875	0.63 ± 0.06	0.406
1.02	0.53 ± 0.08	0.53 ± 0.07	0.573	2.2 ± 0.5	3.156	3.0 ± 1.5	5.76

Tab. 3.2: Measured and calculated extensions of the confocal volume for the two different excitation beam waists ($1/e^2$ -radius). Note that the calculations were done under the assumption of ideal optics and are considered to be only a rough estimate of the expected experimental values.

brightness is not limited to the mentioned concentration range. In principle, the accuracy of the determined molecular brightness depends on the accuracy by which the number of particles in the confocal volume can be determined (see section 3.2.1). Table 3.1 shows the molecular brightness for different pinhole diameters as well as for different excitation beam waists. The left part of the table was measured with an excitation beam waist ($1/e^2$ -radius) of 2.37 *mm* (compared to 4 *mm* back-aperture of the objective), the pinhole diameter was varied between 37 μm and 93 μm . The right part of the table shows measurements with the 63 μm pinhole and two different excitation beam waists (2.37 *mm* and 1.02 *mm*).

Variation of the pinhole diameter changes the Collection Efficiency Function (CEF) while the Excitation Intensity Distribution (EID) remains unchanged. By increasing the pinhole diameter the effective volume increases as will be discussed in section 3.5.3. Reducing the size of the pinhole does not only decrease the effective volume (for the measured effective volumes see table 3.3, section 3.5.3) but also decreases the molecular brightness. Achieving higher confocality is paid by a loss in molecular brightness.

The situation is slightly more complex for the different excitation beam waists. By decreasing the excitation beam waist, the diameter of the focal spot is increased and thus not only the EID is changed but also the collection efficiency function since the latter depends on the size of the confocal spot. For an illustration the measured confocal volumes for two excitation beam waists are shown in figure 3.9. Figure 3.10 shows the calculated EIDs and semigeometrical CEFs as well as the product of both, the MDFs. From figure 3.10 it becomes clear that the increase of the focal spot yields a broader CEF and finally also a larger MDF. The calculated and measured extensions of the confocal volume are summed up in table 3.2

As mentioned, reducing the confocal pinhole diameter decreases the confocal volume thus reducing the number of fluorescence photons that reach the detector, which in turn results

in a decreased molecular brightness. By reducing the excitation beam width, we broaden the EID and therefore the MDF which leads to a larger effective volume. Since the reduction of the MDF through a smaller pinhole leads to a smaller molecular brightness we would expect the molecular brightness to rise when broadening the MDF by broadening the EID. From table 3.1 however, the opposite behavior can be observed. Increasing the effective volume through a broadening of the EID actually decreases the molecular brightness. This effect is due to the decrease of the local laser intensity, since the same laser intensity now is spread over a broader excitation volume.

A focal spot of $0.3 \mu\text{m}$, as expected for an excitation beam waist of 2.37 mm , results in a diffraction limited spot of $36 \mu\text{m}$ at the pinhole plane⁵. For an excitation beam waist of 1.02 mm , the calculated width of the focal spot is $0.69 \mu\text{m}$ which gives a diffraction limited spot of $83 \mu\text{m}$ diameter at the pinhole plane. Since the measurements of the molecular brightness for the 1.02 mm beam waist were done with a pinhole diameter of $63 \mu\text{m}$ the pinhole essentially reduces the fluorescence intensity even from the confocal region.

3.5 Sources of Artifacts and Systematical Errors

FCS is commonly analyzed approximating the molecule detection function by a 3D Gaussian function. While, under ideal experimental conditions this has proven to be a good approximation, errors may arise if these ideal conditions are not met.

The deviation of the real MDF from the usually assumed 3D-Gaussian is a known fact. It is however often ignored because even in the case of a clearly non 3D-Gaussian confocal volume the autocorrelation function still fits the correlated data sufficiently well. Systematic errors introduced due to the deficient model used are often not noticed.

Calculations published by Enderlein et al. [64, 90] investigate the influence of systematic errors due to the deficiency of the 3D-Gaussian model for different experimental conditions as optical saturation, cover-slide thickness mismatch, refractive index mismatch and others. The effects of optical saturation in connection with triplet kinetics have already been subject of experimental studies [20]. To account for deviations of the confocal volume from the assumed 3D-Gaussian the correlation curves have been fitted using two diffusion constants (corresponding to 2 different 3D-Gaussian volumes). However, fitting with 8 parameters will

⁵ see section 2.4.1 for the calculation of the focal spot diameter

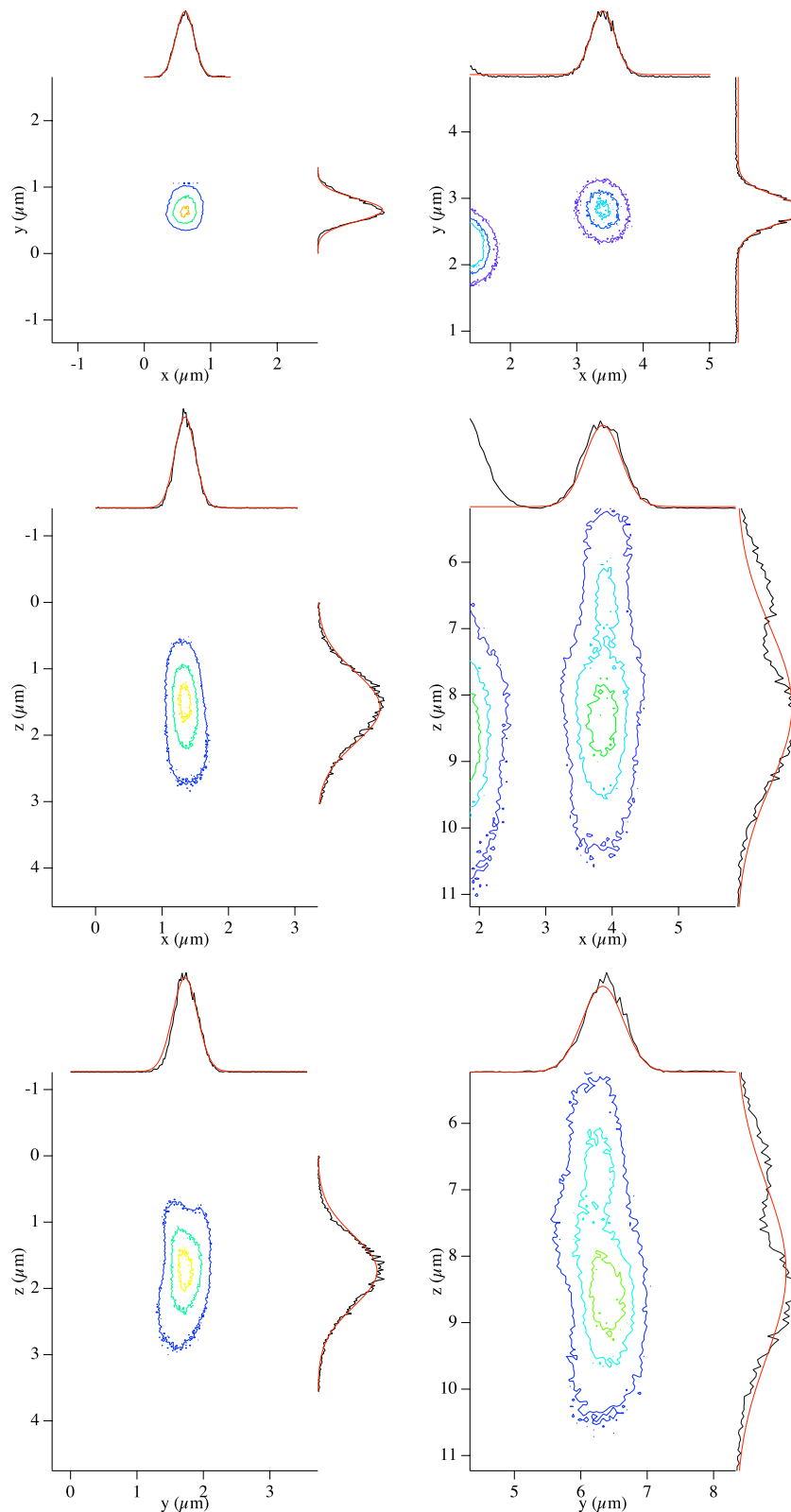


Fig. 3.9: Comparison of the different profiles of the confocal volume for different excitation beam waists; measured on 100 nm TetraSpec beads. The contour lines represent 90%, 50% and 13.5% of the maximum intensity. Left: 2.37 mm beam waist and Right: 1.02 mm beam waist. Along with the 2D sections line profiles through the center-positions are shown. Experimental values are shown as black lines whereas line sections of the 2D Gaussian fits are represented by red lines.

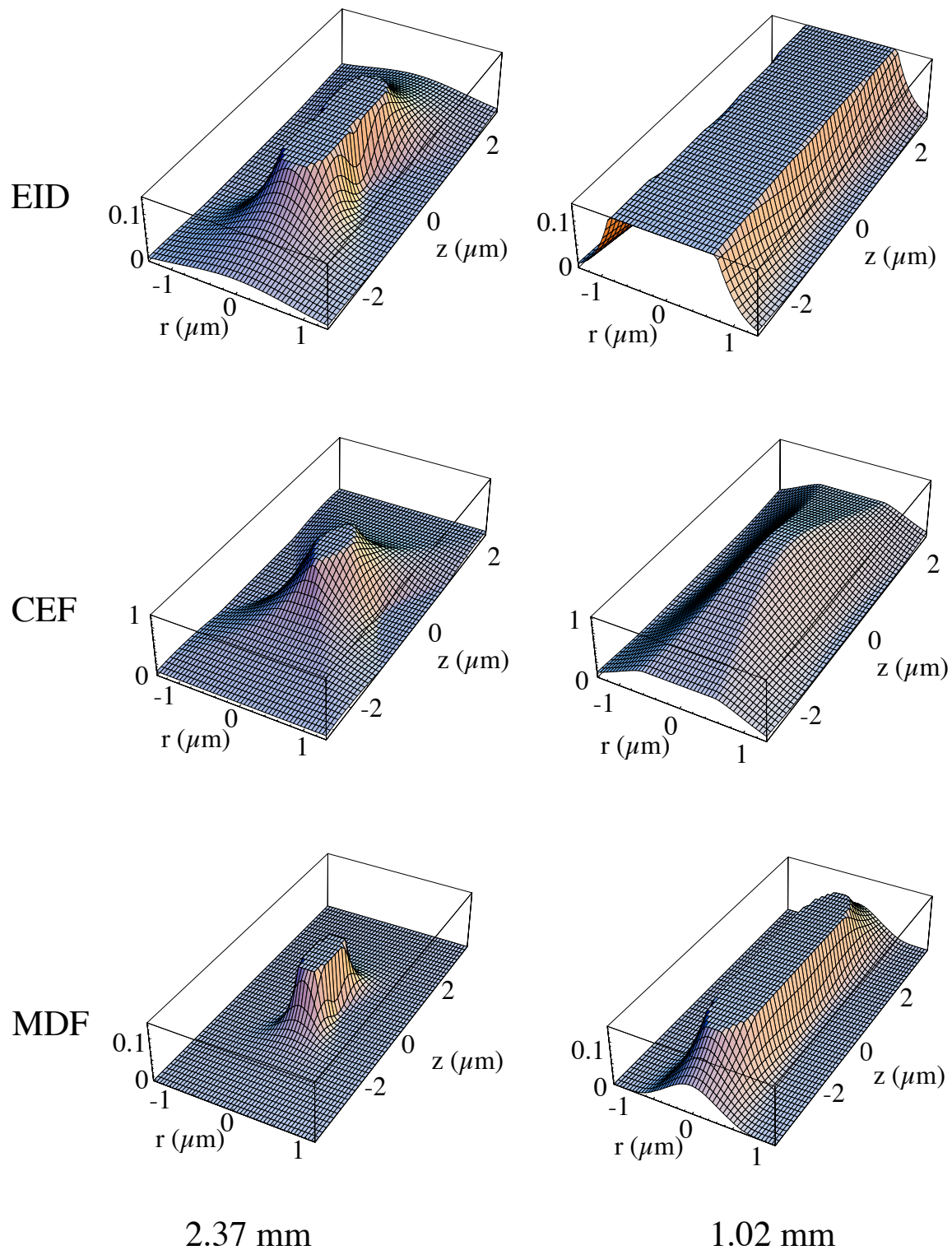


Fig. 3.10: Calculated Excitation Intensity Distribution (EID), Collection Efficiency Function (CEF) and resulting Molecule Detection Function (MDF) for two different excitation beam waists. Left: 2.37 mm beam waist and Right: 1.02 mm beam waist. Note that except for the CEF, the z -axis has been cut at the $1/e^2$ value of its respective maximum. The flat area therefore represents the $1/e^2$ extension of the EID and the MDF respectively.

obviously result in a good accordance with the experimental FCS curve but also render the extracted parameters somewhat questionable.

In the following estimates for the systematical errors introduced by experimental shortcomings will be given, and thus by characterizing them a means to correct for these deficiencies through calibration will be established.

3.5.1 Optical Saturation

Optical saturation occurs when the excitation intensity becomes so large that the molecule spends more and more time in a non-excitable state. Under single molecule conditions and with pulsed excitation, given that the pulse separation is much longer than the fluorescence lifetime, the maximum rate of photons that can be emitted by a fluorophore is the pulse repetition rate. The most common sources of optical saturation are: i) excited state saturation, that is, the fluorophore is still in the excited state when the next photon arrives, ii) triplet state saturation, where the fluorophore undergoes InterSystem Crossing (ISC) from its excited state to a long-lived triplet state, it then can no longer be excited until it returns to its ground state, iii) other transitions to non-fluorescing states, iv) photo destruction. The exact relation between fluorescence emission and excitation intensity can be relatively complex [91] and also depends on whether cw or pulsed excitation is used [92].

The excitation intensity function can be assumed to be of Gauss-Lorentzian shape. Saturation effects therefore will first occur in the center (the focal spot) of the EID. This leads to a deviation of the Excitation Probability Distribution (EPD) from the EID, as the EPD can no longer be assumed to be proportional to the EID. This causes a deviation between the actual MDF and the assumed 3D Gaussian shape of the confocal volume. Consequently the deviation between the assumed model and the saturation affected MDF can lead to misinterpretation of FCS experiments.

To investigate the influence of optical saturation on the correlation function a series of FCS measurements with different excitation powers was performed. Again, the Atto-655 fluorophore was chosen as sample, because it shows almost no triplet state population, saturation therefore is either due to excited state saturation or photo destruction. The fluorescence lifetime of Atto-655 is 1.6 ns (see section 2.5.4), allowing one to operate at a pulse repetition rate of 40 MHz. The concentration of the sample was 5 nM.

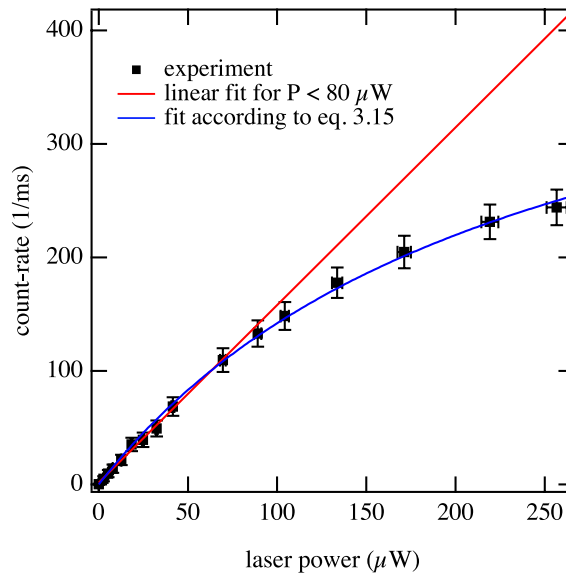


Fig. 3.11: The fluorescence count rate as a function of the excitation power. With increasing excitation power saturation increases and the measured count rate deviates from the linear dependence (red curve).

Figure 3.11 shows the excitation power dependence of the fluorescence count rate. For excitation powers higher than $80 \mu\text{W}$ a deviation due to optical saturation from the linear dependence becomes visible. Usually it is assumed, that the fluorescence intensity depends linearly on the excitation power. This approximation holds only for small excitation powers.

The red line in figure 3.11, displaying the approximated linear dependence, was obtained by fitting the count rates for excitation powers below $80 \mu\text{W}$ with a linear function. The offset was found to be 1.6 ± 1 counts/ms and the slope was found to be (1.56 ± 0.04) counts/(ms, μW). For excitation powers below $80 \mu\text{W}$ the linear approximation is sufficiently satisfied. For higher excitation powers the count rate dependence deviates from the linear approximation and saturation effects become evident. The maximum fluorescence intensity obtainable for this sample can be extracted by fitting the curve depicted in figure 3.11 with the following saturation function:

$$I = I_{max} \frac{P}{P_{sat} + P}. \quad (3.15)$$

I is the measured count rate at excitation power P , I_{max} is the maximum fluorescence count rate. Further increase of excitation power will not yield higher fluorescence count rates. P_{sat} is the excitation power at which the fluorescence intensity reaches half of its maximum

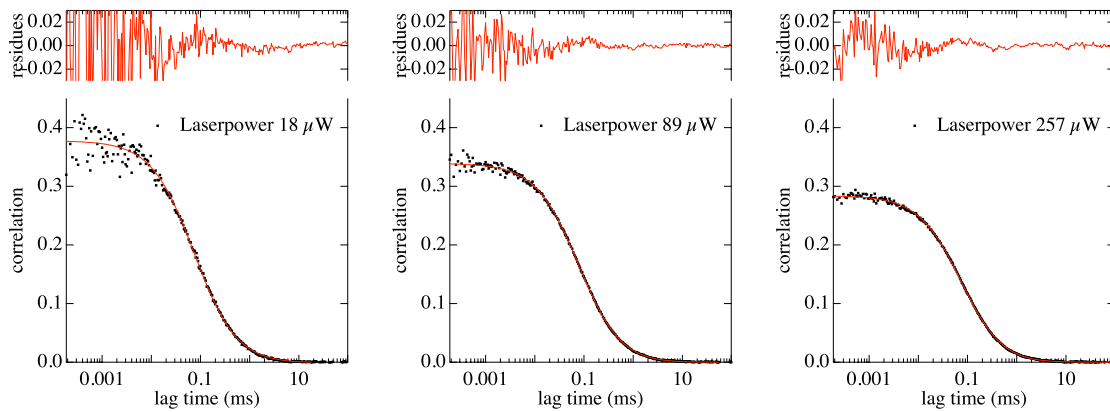


Fig. 3.12: Crosscorrelation of a 5 nM Atto-655 sample for different excitation powers and respective fits, assuming a 3-dimensional Gaussian MDF.

value. P_{sat} is a measure of how fast saturation is reached. $I_{max} = (485 \pm 20)$ counts/ms and $P_{sat} = (242 \pm 16)$ μW were found from the fitted saturation curve, represented by the blue curve in figure 3.11.

Figure 3.12 showcases FCS curves for different excitation powers with their respective fits. Notably, the amplitude of the autocorrelation function is reduced with increasing excitation power. According to calculations of Enderlein et al. [64] optical saturation yields a deformation and an increase of the effective volume (V_{eff}). As the excitation power increases, saturation will first appear in the center of the beam in the focal plane. This will lead to a broadening of the fluorescence intensity profile, thereby increasing V_{eff} and decreasing the correlation amplitude [20]. Defining the optical saturation factor ζ as

$$\zeta = \frac{\max(P)}{P_{sat}}, \quad (3.16)$$

Enderlein et al. found for $\zeta = 1$ an increase of the apparent concentration by a factor of approximately 1.6. $\max(P)$ in reference [64] refers to the maximum excitation intensity, that would be found in the center of the EID. The calculations also account for the shape of the EID, which is not experimentally accessible. Considering that the experimental parameters (objective, focussing and so on) are also different from the assumptions used for the calculations, a comparison can only be qualitative. However, looking at figure 3.12a and figure 3.12c, we see the correlation amplitude drop from 0.38 to 0.28, meaning an increase of the number of particles $\langle N \rangle$ in V_{eff} by a factor of 1.36, compared to 1.6 published in [64].

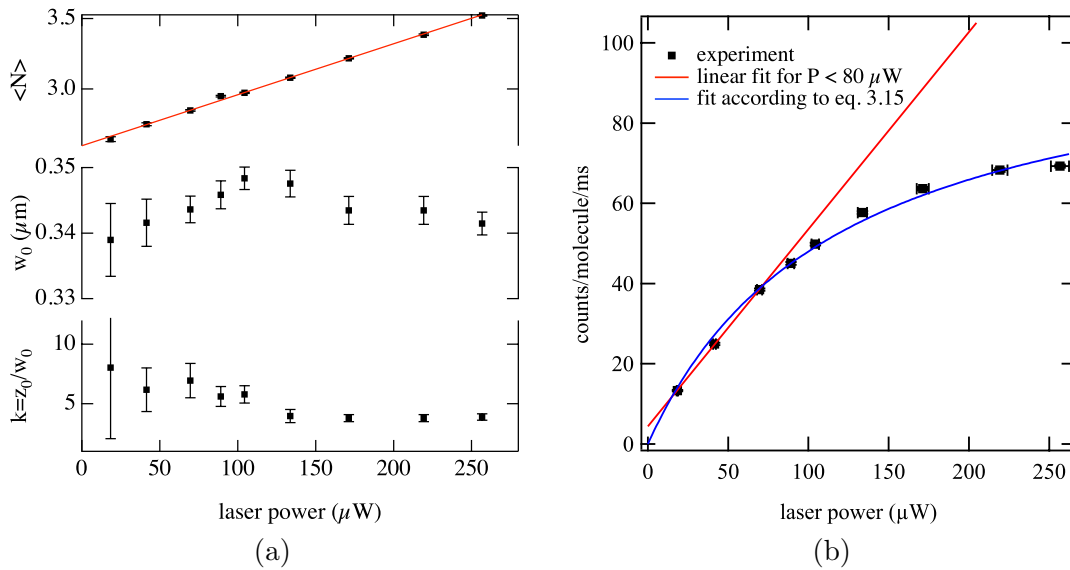


Fig. 3.13: (a) $\langle N \rangle$ increases with the excitation power. The rise is caused by an increase of V_{eff} . The increase of V_{eff} is not reflected directly in w_0 and k . This might be due bleaching or simply caused by the increasing deviation between experiment and model used to extract w_0 and k . (b) The saturation effect becomes even more evident when looking at the fluorescence count rate per molecule.

Figure 3.13a shows $\langle N \rangle$ along with the parameters defining the size of the assumed 3D Gaussian MDF (w_0 and k). While $\langle N \rangle$ rises with increasing excitation power, V_{eff} does not follow this trend as can be seen from w_0 and k in figure 3.13a. One explanation might be the breakdown of the 3D Gaussian model at higher excitation powers due to the expected deformation of the MDF. Another explanation might be the occurrence of photo-bleaching. If bleaching takes place in the same time range as diffusion, it may just result in a slightly shortened diffusion time, thus yielding a lower determined w_0 , while $\langle N \rangle$ would not be affected. Despite the fact that the uncertainties of w_0 are rather large this interpretation is supported by the evolution of w_0 with increasing excitation power. Up to a power of 104 μW w_0 rises, while above this excitation power w_0 starts to decrease again. This decrease could be caused by the appearance of bleaching. It would counteract the apparently increasing observation volume due to optical saturation and explain the discrepancy between an increasing number of molecules and the excitation power dependence of the lateral beam radius w_0 .

The saturation effect becomes even more pronounced when looking at the fluorescence intensity per molecule. Figure 3.13b shows the dependence of the fluorescence intensity per molecule on the laser power⁶. Fitting with equation 3.15 reveals a maximum of $I_{max} =$

⁶ Contrary to section 3.4 and chapter 4, here the count rate per molecule is not normalized with the

105 ± 5 detected photons per molecule and millisecond and an excitation power of $P_{sat} = (119 \pm 11) \mu W$ necessary to reach half of the maximum fluorescence intensity per molecule. Saturation on the per-molecule level occurs almost twice as fast as for the fluorescence count rate. The saturation of the latter is partly compensated by the increasing number of molecules excited/detected.

The maximum absorption cross section of Atto-655 is $4.6 \times 10^{-8} \mu m^2$. An excitation power of $100 \mu W$ equals 8×10^6 photons per pulse and with a beam radius ($1/e^2$) of $0.38 \mu m$ this gives a photon density of $17.6 \times 10^6 1/\mu m^2$ per pulse. Hence, at an excitation power of $100 \mu W$, every Atto-655 fluorophore absorbs on average 0.5 photons per burst. The saturation power (P_{sat}) was found to be $105 \mu W$ almost identical to the calculated saturation power. Therefore triplet or other dark-states are not necessary to explain the experimentally found saturation power, which is consistent with the absence of triplet dynamics in the FCS curves. The calculation however is only a rough estimate since the excitation power was assumed to be uniform while in reality it is distributed according to the EID. Therefore the occurrence of photo-bleaching or the existence of long-lived (longer than the diffusion time) dark-states can not be excluded (evidence of the existence of photo-bleaching was given above).

Since $\langle N \rangle$ depends on the excitation power, this dependence has to be acknowledged when measuring concentrations with FCS. V_{eff} needs to be determined with the same laser excitation power used in the final FCS experiment and has to be measured on the same fluorophores. If, for example, imaging of fluorescent microspheres is used for the determination of the confocal volume, this volume needs to be corrected for the saturation effect⁷. Figure 3.13a enables us to extrapolate $\langle N \rangle$ for a saturation factor of $\zeta = 0$ (linear power dependence assumed). For an imaginary excitation power of $0 \mu W$, 2.60 ± 0.01 particles are expected in V_{eff} . Assuming that the dependence of $\langle N \rangle$ on the excitation power is only caused by the change of V_{eff} , for an excitation power of $89 \mu W$ the effective volume is predicted to be by 13% larger than for the imaginary case of no excitation at all.

The FCS measurements presented in this chapter were performed at an excitation power of $89 \mu W$. The fluorescence count rate per molecule, at $89 \mu W$, has reached 43% of its maximum value. This makes a good compromise between confocal volume distortion, molec-

excitation power.

⁷ Imaging of fluorescent microspheres will not be influenced by saturation effects because of the much lower excitation powers.

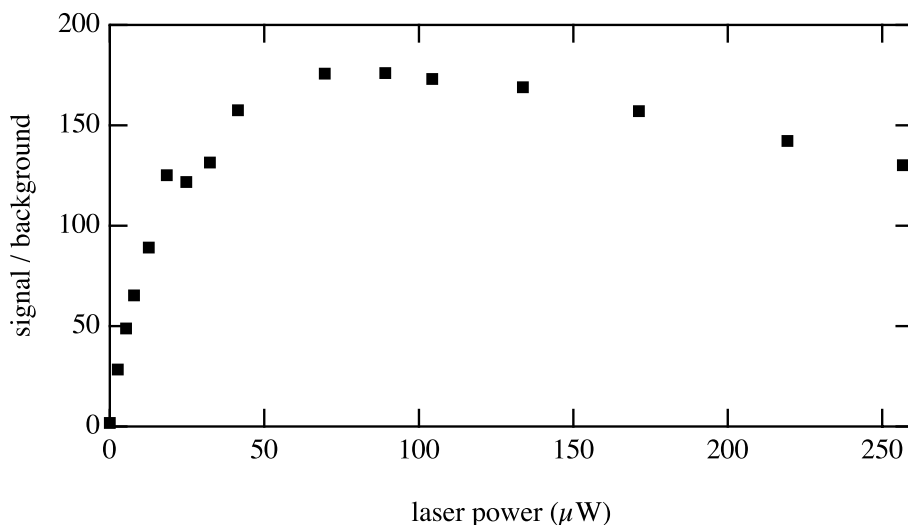


Fig. 3.14: Dependence of the signal to background ratio on the excitation power. Two sources contribute to the background: (i) constant background due to ambient light and dark-counts of the SPADs and (ii) background due to scattering of the excitation light on solvent molecules. The latter depends linearly on the excitation power. Therefore the signal to background ratio rises up to a maximum. The following decline is due to optical saturation of the fluorophore.

ular brightness and signal to background ratio (see figure 3.14). For the $89 \mu\text{W}$ excitation power used in the FCS experiments, the effective volume is expected to be about 13% larger compared to the effective volume measured on fluorescent microspheres.

3.5.2 Cover-Slide Thickness Correction

The next effect studied is the impact of cover-slide thickness on the MDF and thus on the FCS. Water-immersion objectives are optically corrected for imaging through cover slides of a definite thickness. Advanced objectives offer the possibility to adjust them to a specific thickness value with an adjustment ring. A deviation of the cover-slide thickness from its expected value introduces aberration into the optical system, leading to deteriorated laser focusing and fluorescence detection. Although cover slides are sold with a specified thickness value, their actual thickness may differ by a few percent. A wrong cover-slide correction leads to a deformation of the confocal volume and due to its increase to a wrongly determined concentration and diffusion coefficient.

Figure 3.15 shows examples of confocal volume profiles, recorded for two different cover-slide thickness settings. The profiles were acquired by scanning a fluorescent microsphere

(bead) in all three spatial planes (see also section 2.6). The actual thickness of the cover-slide was measured with a micrometer screw and found to be $(153 \pm 1) \mu\text{m}$. On the left side of figure 3.15 confocal volume profiles for the correct cover-slide correction setting are shown, while the profiles on the right side of figure 3.15 were recorded with the cover-slide correction ring set to $190 \mu\text{m}$, a rather large deviation of $40 \mu\text{m}$. While the differences between both correction ring settings are not obvious in the xy -plane, the xz - and yz -profiles show a significant increase of the axial extension of the confocal volume. The eccentricity of the confocal volume increases if the correction ring setting deviates from the actual cover-slide thickness.

The profiles of the same fluorescent microsphere were recorded for several cover-slide thickness corrections and fitted with 2-dimensional Gaussian functions in order to calculate V_{eff} for each correction ring setting (see section 2.6 for details). Additionally, V_{eff} was determined by FCS analysis of a 5 nM Atto-655 sample (as described in section 3.2.2).

Figure 3.16 shows the dependence of V_{eff} on the cover-slide correction ring setting. As expected, the effective volume increases with increasing cover-slide thickness deviation. As already supposed from figure 3.15 the increase of V_{eff} is due to an increase of the eccentricity k . While w_0 does not change significantly for different correction ring settings, k noticeably increases with the cover-slide thickness deviation.

The w_0 - and k - values obtained with FCS do not fall together with the ones measured on the fluorescent microspheres. Interestingly w_0 obtained with the fluorescent microspheres is higher than the FCS obtained value, while this is reversed for the eccentricity k . This behavior is probably caused by optical saturation, which is an issue for the FCS measurements but not for the measurements on the fluorescent microspheres.

The increase of the eccentricity with increasing cover-slide thickness deviation is in agreement with the findings of Enderlein et al. [64]. According to their calculations the MDF becomes elongated and slightly shifts along the optical axis for increasing cover-slide thickness deviation. The calculations also revealed an increase of V_{eff} . For a cover-slide thickness deviation of $10 \mu\text{m}$ Enderlein et al. find the confocal volume to increase by a factor of 2. Certainly an increase of the confocal volume is found, the findings of this work however, are not so pronounced. The calculations were performed for diffraction limited focussing while in the experiments described here, the back-aperture of the objective was underfilled and

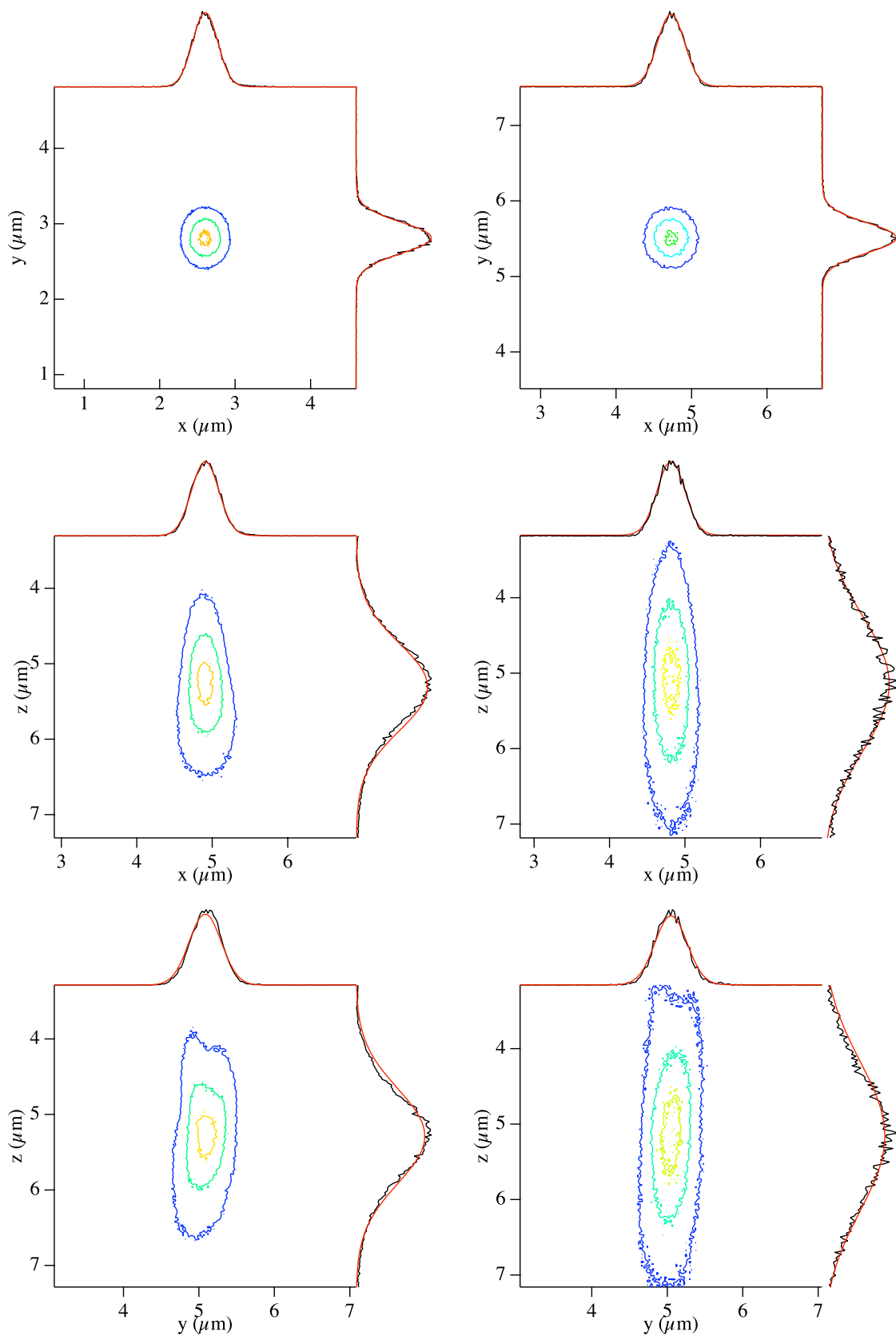


Fig. 3.15: Influence of the cover-slide thickness deviation on the confocal volume, measured on 100 nm TetraSpec beads. Sections of the confocal volume are shown for the correct cover-slide thickness setting (left) and a deviation from the correct setting of 40 μm . (right). The contour lines represent 90%, 50% and 13.5% of the maximum intensity. Along with the 2D sections line profiles through the center-positions are shown. Experimental values are shown as black lines whereas line sections of the 2D Gaussian fits are represented by red lines.

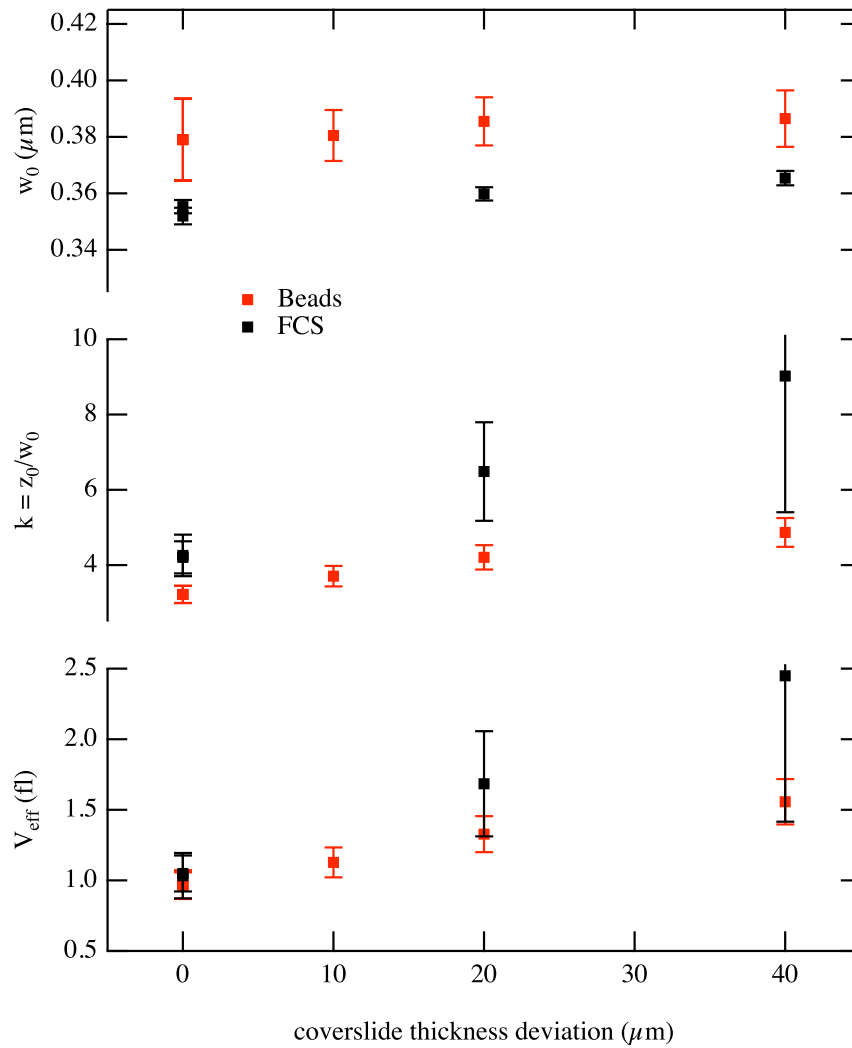


Fig. 3.16: The effective volume (V_{eff}) for different cover-slide thickness corrections. The used coverslide had a thickness of $153 \mu\text{m}$. Values resulting from 100 nm TetraSpec beads (red) are shown together with the volume deduced from fitting the autocorrelation curves of a 5 nM Atto-655 solution

focussing therefore is not as strong as assumed in the calculations. Aberration effects are expected to be more pronounced for stronger focussing which explains the stronger increase of V_{eff} predicted by Enderlein et al.

3.5.3 Influence of the Pinhole Diameter

The axial resolution of a confocal microscope is due to the integration of a pinhole which is placed conjugate to the spot being illuminated. Only the light originating from the illuminated spot is transmitted. As shown in section 2.4.3, the pinhole diameter influences the CEF. And since the MDF is a direct product of the EPD and the CEF, the confocal volume depends on the size of the confocal pinhole. By varying the pinhole diameter, the CEF is altered while the EID (and therefore the EPD) remains unchanged.

Usually the pinhole radius is chosen slightly larger than the beam waist in the confocal plane ($R \gtrsim w_0 \cdot M$). The pinhole then mainly determines the axial extension of the CEF and with it the MDF and therefore the confocal volume.

The beam waist in the sample has a $1/e^2$ radius in the order of $0.3 \mu m$ (section 2.4.1), which yields a corresponding minimum pinhole diameter of $36 \mu m$. Three different pinhole diameters above this threshold ($37 \mu m$, $63 \mu m$ and $93 \mu m$) were chosen and the images of fluorescent microspheres were recorded (see also section 2.6).

Figure 3.17 shows the profiles of the confocal volume for two pinholes with diameters of $36.5 \mu m$ (figure 3.17, left) and $92.8 \mu m$ (figure 3.17, right) respectively. As can be seen also from table 3.3, the confocal volume increases when a larger pinhole is chosen. Both, the lateral w_x , w_y and the axial size w_z increase. The increase of the axial extension however is more pronounced than the increase of the lateral. The discrepancy between w_x and w_y is due to astigmatism of the excitation laser beam. The calculated values are shown for comparison. Although the trend is reproduced, a quantitative agreement, is not expected because of the simplified nature of the calculations. Looking at the xz-sections, we notice that while for the the $37 \mu m$ pinhole the effective volume is relatively smooth, additional features besides the expected shape occur when measuring with the $93 \mu m$ pinhole. These features have been predicted for refractive index mismatch by calculations [64], as it occurs here, since the fluorescent microspheres were placed on the coverslide surface. We see these ring-like features on the air-side of the glass-air interface, which is consistent with Enderleins calculations [64]

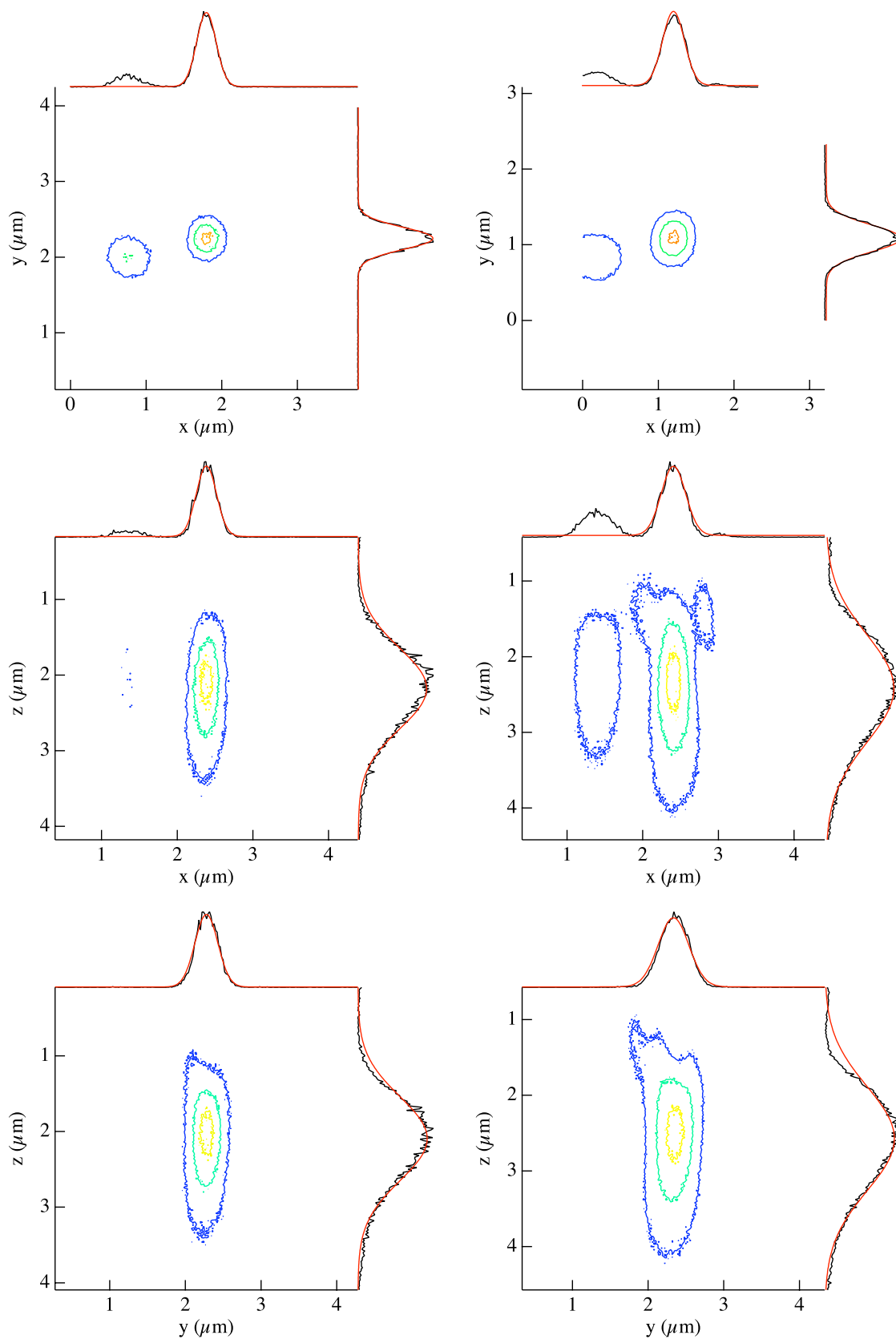


Fig. 3.17: Profiles of the confocal volume for different pinhole diameters, measured on 100 nm TetraSpec microspheres. Left: 36.5 μm and Right: 92.8 μm . The contour lines represent 90%, 50% and 13.5% of the maximum intensity. Along with the 2D sections line profiles through the center-positions are shown. Experimental values are shown as black lines whereas line sections of the 2D Gaussian fits are represented by red lines.

diameter	w_x (μm)	w_y (μm)	$w_{x,y}^{calc}$	w_z (μm)	w_z^{calc}
37 μm	0.262 ± 0.005	0.36 ± 0.07	0.243	1.16 ± 0.09	0.605
63 μm	0.29 ± 0.01	0.36 ± 0.02	0.289	1.23 ± 0.08	0.875
93 μm	0.31 ± 0.01	0.38 ± 0.02	0.295	1.40 ± 0.02	1.11

Tab. 3.3: Lateral and axial dimensions ($1/e^2$ -radii) of the MDF for the different pinholes measured. Calculated values (see section 2.4) are shown for comparison.

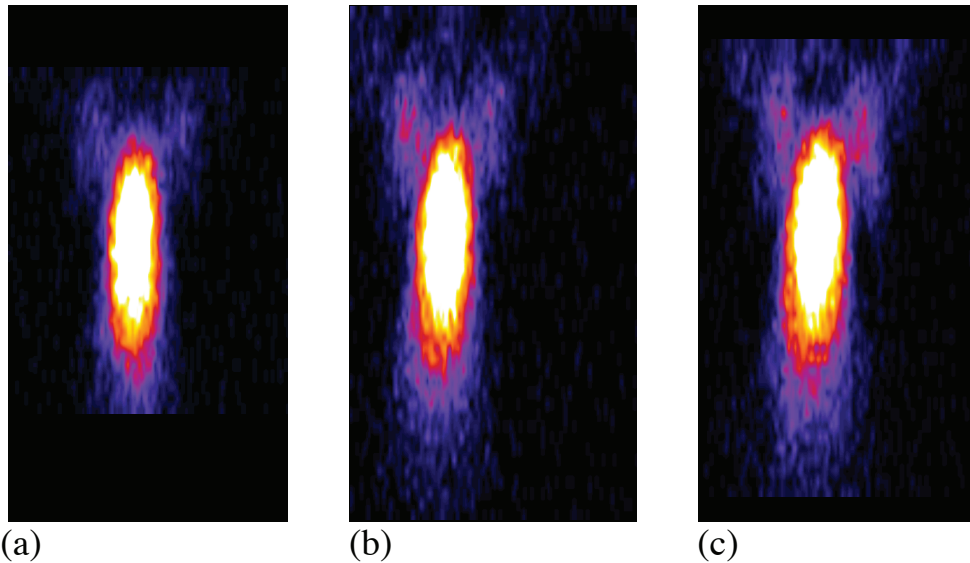


Fig. 3.18: xz-sections of the effective volume measured with 3 different pinholes: (a) 37 μm , (b) 63 μm and (c) 93 μm . The sections are 0.1 μm off the center of the MDF. The contrast has been enhanced to show lower intensity features.

as well as general expectation, since the microscope objective used, is designed for imaging through a cover slide in water. The occurrence of the ring-like features is not correlated with the pinhole diameter as might be assumed from figure 3.17, while their impact on the MDF, on the other hand, is dependent on the pinhole diameter. The ring like features are already present in the EID. Figure 3.18 shows intensity images of the MDF, measured with the three different pinholes. The contrast has been enhanced, maximum image intensity has been set to the half of the maximum detected count rate. Obviously the mentioned features do exist for all pinhole sizes, their intensity however increases with increasing pinhole diameter. This is indeed expected as the pinhole diameter mostly influences the depth of focus: a narrower pinhole results in a faster decrease of the CEF as can be seen from figure 3.19.

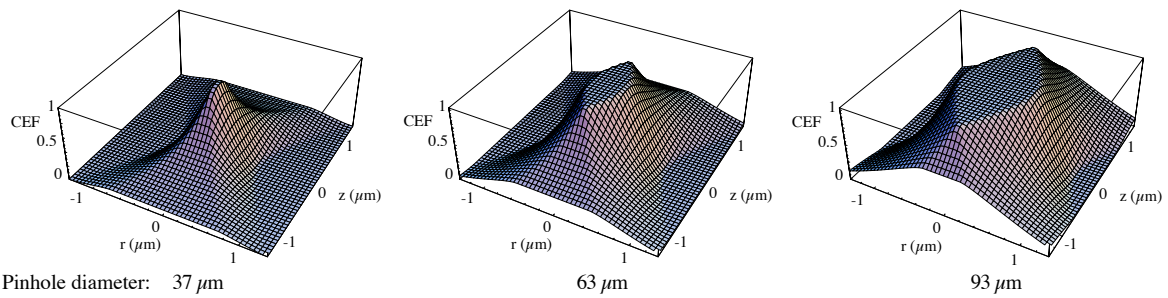


Fig. 3.19: Semigeometrical approximation of the CEF for the different pinholes used. For details on the calculation of the CEF see section 2.4.3.

3.6 Discussion

It has been shown in this chapter, that it is possible to measure the number of particles contained in the effective volume of a confocal scanning microscope for a concentration range covering six orders of magnitude. Uncorrelated background significantly hampers accurate determination of the number of particles for concentrations below 500 pM , this however can be taken into account and the correlation amplitude can be corrected for the influence of uncorrelated background. With this correction particle numbers for sample concentrations as low as 1 pM and concentrations as high as 1 μM could be determined. The uncertainties for the determination of the particle numbers are below 1% for concentrations between 50 pM and 100 nM . The small deviation from the expected linear dependence of the number of particles on the sample concentration is probably not due to uncertainties of the measuring technique itself but caused by sample loss during the sample preparation process.

Measuring concentrations with FCS requires knowledge about the effective volume which is not easy to determine. The two usually used methods are imaging of the effective volume by scanning a fluorescently labeled microsphere and determination of the effective volume by fitting the FCS of a dye with a known diffusion coefficient. In this chapter the mentioned methods were compared with a not commonly used approach.

It was shown that it is possible to extract the effective volume from the FCS analysis of a sample dilution series, where the sample was prepared simply by pipetting. The advantage of this technique is that it does not depend on a particular model for the Molecule Detection Function (MDF). The resulting effective volume was $(1.0 \pm 0.1) \text{ fl}$. The uncertainty is caused by the sample preparation method and the surface adsorption of the sample at low concentra-

tions. While it is probably not possible to prevent surface adsorption for low concentrations, the accuracy of the sample preparation method can be improved e.g. by using gravimetric dilution.

The other method to extract the effective volume from FCS measurements requires the knowledge of the diffusion coefficient of the fluorophore under investigation. There is no need to know the exact sample concentration and sample loss due to adsorption does not influence the result. The effective volume is extracted by fitting a model function to the correlated data, which also requires assumptions to be made about the MDF. The MDF was assumed to be a 3D Gaussian function. Since this approach involves fitting of the model function to the experimental data, the quality of the correlated data also influences the precision of the findings. It was found that the determination of the confocal volume was only possible for samples with concentrations between 100 *pM* and 5 *nM*. Altogether, the effective volume resulting from FCS fits can only be determined as precise as the used model describes the experimental reality. With this method the confocal volume was determined to be (1.15 ± 0.06) fl.

By scanning a fluorescent microsphere an effective volume of (1.0 ± 0.1) fl was found. Because of optical saturation occurring in the FCS experiments, the effective volume determined with both FCS methods is expected to be larger by 13%. While for the fitting approach this expectation is satisfied, the dilution series yields the same effective volume as the imaging of the fluorescent microspheres. The uncertainties of all three methods however are rather large and the saturation effect might not be resolvable.

Regarding the uncertainties of the three methods no clear recommendation for the determination of the effective volume can be given. However, the two methods employing FCS measurements have the advantage that the effective volume is measured in aqueous environment and distortions of the MDF due to this environment are taken into account. The dilution series approach offers additionally strong advantages over the two other methods since it does not depend on model assumptions.

To analyze the limits of the commonly used 3D Gaussian model for the MDF the influence of optical saturation, cover-slide thickness deviation, different pinhole diameters and different beam waists was investigated. In agreement with the calculations done by Enderlein et al. [64] the measurements show that saturation significantly influences the MDF. The increase of the

effective volume will lead to apparently higher concentrations. Even for modest excitation power ($P \sim 0.4 \cdot P_{sat}$) the confocal volume was found to increase by 13% compared to the extrapolated effective volume for no excitation. The increase of the effective volume due to saturation has to be accounted for, especially as FCS measurements have to be performed with high excitation intensities in order to obtain a sufficient count rate per molecule. The fact that saturation depends on the used fluorophore implements the necessity to analyze saturation characteristics for the fluorophore under investigation and to take it into account in the analysis. Without the occurrence of photo-bleaching, optical saturation results in an apparently smaller diffusion coefficient or a larger confocal volume, depending which parameter is fitted. Evidence for photo-destruction of the fluorophores was found at higher laser power levels which led to lower diffusion times and ultimately could result in a wrongly determined effective volume or diffusion coefficient.

Due to optical saturation not only the size of the confocal volume but also its shape changes. The assumption of a 3D Gaussian shape, therefore, with increasing excitation intensities, leads to increasing systematic errors. In agreement with Enderlein et al. [64] I conclude, that saturation effects always need to be taken into account in FCS experiments and that fluorophores and excitation intensities need to be chosen carefully to avoid misinterpretation of the findings.

The experiments showed that the molecular brightness depends on the diameter of the confocal pinhole. By decreasing the pinhole diameter, a higher confocality and thus a smaller confocal volume is achieved but this increase in resolution is paid by a decrease of the molecular brightness. Decreasing the excitation beam width on the other hand increases the confocal volume but also decreases the molecular brightness since the local excitation intensity is reduced. Therefore, excitation beam width and pinhole diameter have to be chosen according to each other.

The cover slide thickness correction ring setting of the objective is influencing the shape of the MDF. Besides the ability to adjust the objective to different cover slides, it can be used to correct for refractive index mismatch and other aberrations. By imaging fluorescent microspheres for different correction ring settings the shape of the MDF can be monitored and optimized.

The MDF is sensible to the experimental conditions. It is therefore most desirable to

calibrate the effective volume under the exact same conditions that apply in the experiment of interest. For the same reason it is advisable to use the same fluorophores during the experiments that were used for calibration, since a change in the photo-physic of the fluorophore will yield a change of the MDF. If this is not possible saturation effects have to be quantified and considered in the analysis.

With respect to the experimental protocol of FCS experiments I suggest to measure the MDF with fluorescent microspheres as this techniques yields an image of the MDF and artifacts can directly be identified. If the adjustment of the apparatus is found to be sufficient to be approximated by a 3D Gaussian function, then the confocal volume can be extracted from a fit of the correlation of the dye that will be used in the experiment, given its diffusion coefficient is known. Measuring the confocal volume through a dilution series is undoubtedly elaborate, but offers the advantage of being model independent and that the diffusion coefficient does not need to be known. The accuracy in this case only depends on the accuracy of the sample preparation. The effect of saturation on the MDF should always be taken into account, therefore the saturation curve should be recorded for all dyes employed in the determination of the effective volume and the final FCS measurements. To our finding a power of $P = 0.4 \cdot P_{sat}$ is the best compromise between low saturation and good signal to background ratio.

4. POLYPROLINE AS CALIBRATION ASSAY FOR FRET DISTANCE MEASUREMENTS

Förster Resonance Energy Transfer (FRET) describes an energy transfer mechanism between two fluorescent molecules¹. A fluorescent donor is excited at its specific fluorescence excitation wavelength. By a dipole-dipole coupling mechanism, the excitation energy is then nonradiatively transferred to a second molecule, the acceptor. The donor returns to the electronic ground state. The transfer efficiency depends on the distance between the donor and acceptor fluorophore [42, 54, 93].

FRET found its first application as "spectroscopic ruler" in 1967 [24], where it was used to experimentally prove the distance dependence found by Förster [42]. Ensemble FRET measurements have been used to characterize structures of different nucleic acids, B- and Z-DNA structures [94–96] but also complex structures like bent DNA [97, 98], three-way-junctions [99], hairpins [100, 101] and holliday-junctions [102] have been investigated for example.

With the recent advances in single molecule detection, single pair FRET (spFRET) serves as a means e.g. to detect co-localization and conformational changes of single molecules. Donor-acceptor distances on B-DNA molecules have been measured with spFRET in solution [11] and immobilized [29]. Conformational changes of the RNA strands in ribozymes [103] have been studied extensively as well. Studies of conformational dynamics of nucleic acids and proteins however, have as yet been limited to the investigation of relative distance changes [104–106].

There are two methods to analyze the energy transfer efficiency of a FRET pair in solution. The first uses the ratio of the fluorescence emission of the donor and acceptor fluorophores while the second method is based on the reduction of the donor fluorescence lifetime due to the additional relaxation channel provided by the energy transfer to the acceptor. Quanti-

¹ The acceptor does not necessarily need to be a fluorophore.

tative distance measurements with FRET on the single-molecule level are hampered by two problems:

The first is the occurrence of the so-called zero-efficiency peak [11], which is attributed to FRET pairs with a nonfluorescent or missing acceptor fluorophore [11, 107, 108]. To support this hypothesis it was shown that the zero-efficiency peak can be reduced by a factor of four if photobleaching of the acceptor is avoided [109].

Secondly the energy transfer efficiency calculated from the ratio of the donor and acceptor fluorescence intensity is subject to systematical errors due to spectral leakage, different fluorophore quantum yields and different detection efficiencies. Additional uncertainties result from the unknown relative dipole orientation of the donor and acceptor which influences the energy transfer efficiency. Different techniques have been developed in the past years to circumvent the problems mentioned. Multi Parameter Fluorescence Detection (MPFD) has been developed in the Group of Prof. Seidel in Düsseldorf, Germany [110]. With MPFD-FRET not only the intensities of single molecule fluorescence bursts are used to calculate the FRET efficiency but also fluorescence lifetimes are analyzed burstwise (Burst Integrated Fluorescence Lifetime, BIFL). The FRET efficiency is then calculated from a 2D histogram. Analyzing fluorescence lifetimes of diffusing single molecules is however far from trivial since only a few (usually below 100) photons can be collected per burst. Very recently, Lee et al. [111] published a method for accurate FRET measurements. Alternating Laser Excitation (ALEX) of donor and acceptor in the μs range was used to sort out donor-only molecules and an analyzing scheme to calculate accurate FRET efficiencies in the presence of leakage and direct excitation of the acceptor was presented. Since this method uses relatively long laser pulses it does not allow for a fluorescence lifetime analysis.

Because of the mentioned problems it is obvious that FRET distance measurements need to be calibrated in order to achieve quantitative results. The most promising candidate for a calibration assay appears to be the "spectroscopy ruler", the 1967 studied poly-L-proline. Poly-L-proline is regarded as the stiffest homooligopeptide [112] and therefore has been used already in 1967 for the experimental validation [24] of Förster's theory [42]. Since then it has been used to address a wide range of biological questions [51, 113–115]. Schuler et al. [107] reinvestigated poly-L-proline in 2002 with single molecule methods and encountered significant discrepancies between the experimental findings and the expected distance dependence.

The discrepancies could be explained with molecular dynamics. Simulations of the molecular dynamics of poly-L-proline recently revealed that it is behaving more like a worm-like chain [116] than rigid rod as assumed before [112, 117].

In this chapter, a novel method based on Pulsed Interleaved Excitation (PIE) as suggested by Don Lamb [118] will be presented to overcome the limitations mentioned above. I have used PIE to suppress the zero efficiency peak and to determine the fluorescence lifetime based on Time Correlated Single Photon Counting (TCSPC). For the first time to my knowledge the contributions of signal cross talk (leakage), direct acceptor excitation, different detection efficiencies as well as different confocal volumes for donor and acceptor fluorophores to the measured FRET efficiencies were determined by Fluorescence Correlation Spectroscopy (FCS). It is worth to notice, that the advantages of combining FRET with FCS analysis are much easier to achieve with the proposed PIE than with the ALEX approach since the pulse duration as well as the repetition time interval for ALEX are in the same temporal range as the triplet state lifetime of the dye molecules. It will be shown that all data needed for accurate determination of FRET based on intensity ratiometric measurements as well as fluorescence lifetime measurements can be retrieved by performing only a single measurement.

The developed method was applied for the determination of the conformation of the TransLocation Motif (TLM), a cell permeable protein that could be identified on the surface of the HBV virus [35]. Among various other transporter peptides, TLM is of special interest as it, unlike other peptides, does not show any tissue specificity or specificity for subcellular structures. It has been shown, that TLM is capable of transporting peptides [34, 35] and functional proteins [36] as well as particles and functional nucleic acids [37]. However the exact transport mechanism is not clear by now. The original intention of my collaborators at the Robert Koch Institute was to follow the membrane passage of TLM with FRET, as they expect the incorporation to be accomplished by a conformational change from the native α -helical structure [119] to a β -strand. Unfortunately the labeling strategy deployed by my collaborators essentially inhibited a transformational change as the used linkers impose their tertiary structure of the TLM. Therefore the labeling destroyed the cell permeability of the TLM peptide. Although the cell penetration mechanism of the TLM molecule could not be elucidated for the mentioned reason, it was however possible not only to determine the structure of the TLM but also to precisely measure its length in solution.

4.1 The Poly-L-Proline Assay

As mentioned, FRET distance measurements need to be calibrated in order to yield quantitative results. Therefore it is necessary to have a set of spacer molecules with different known lengths. The most obvious candidate for such a calibration assay would be DNA. However, due to its structure the distance between the fluorophores that would be coupled to it does not linearly depend on the length (the number of residues) of the DNA. The helical structure has to be considered [94].

At the time the calibration assay was planned, the other candidate, poly-L-proline was regarded as the stiffest homooligopeptide [112]. The structure was known [120] and it had already been subject of several FRET studies [24, 51, 113–115]. Therefore poly-L-proline was chosen as spacer molecule. It was only last year, that molecular modeling calculations [116] showed that poly-L-proline is not as stiff as assumed before. Details on the molecular structure and dynamics are given in section 4.1.3 and 4.1.4.

4.1.1 Selection of the Fluorophores

Since the long term goal of this study was the monitoring of conformational changes of the TLM molecule during membrane passage the fluorophores were selected accordingly. Important factors for FRET pair selection are from the biological point of view

- Förster radius (defines the working range for distance measurements)
- solubility in water
- bio-compatibility (not interfering with cellular processes, fluorophores need to be small in size)
- chemical stability in water
- the longer the excitation wavelength the better (since endogenous fluorescence in cells is mostly in the short wavelength range)

and from the physical point of view

- available laser wavelengths for excitation
- photo-stability
- low triplet fraction

- high quantum yield
- spectral separability

Obviously not all of the above listed criteria can be fulfilled, and as the order of the criteria already suggests, in most cases the biological necessities are to be considered more important as they, if not satisfied, would render the experiment senseless. Alexa-555 and Alexa-647 were chosen as donor-acceptor pair since their Förster radius is with 5.1 nm ideal to monitor the conformational change in the TLM molecule (the conformational transition expected is from α -helix (3.7 nm) to β -strand (6.1 nm)).

To cover the interesting distance range from about $0.5R_0$ to $1.5R_0$, four different lengths ($\approx 2, 4, 6, 8$ nm) of type II poly-L-proline were labeled with Alexa-555 and Alexa-647 as donor and acceptor: Alexa-647-Gly-(Pro)_{6,12,18,24}-Cys-maleimide-Alexa-555

4.1.2 Spectral Properties of Alexa-555 and Alexa-647

The absorption spectra of Alexa-555 and Alexa-647 have been measured using a Perkin Elmer Lambda9 spectrophotometer (Perkin Elmer GmbH, Germany). Figure 4.1 shows absorption of both dyes solved in Phosphate Buffered Saline, additionally containing the detergent Tween 20 (PBST). Alexa-555 has a maximum absorbance of 0.27 at 552 nm, while Alexa-647 has a maximum absorbance of 0.17 at 649 nm. The supplier, Molecular Probes specifies the absorption maximum for Alexa-555 to be at 555 nm and for Alexa-647 at 651 nm, both values for MeOH solutions. Obviously the absorption spectra shift 3 nm for Alexa-555 and 2 nm for Alexa-647 respectively to lower wavelengths when PBST is used as solvent instead of MeOH. Additional measurements with both dyes solved in MeOH (not shown) reproduced the values of Molecular Probes, indicating that the blue-shift of the absorption spectra is due the influence of the solvent. The extinction coefficients ϵ of Alexa-555 and Alexa-647 solved in MeOH are available on the Molecular Probes website [121] and on Wikipedia [122]. Apparently the values changed during the time span of this work. While when the dyes were purchased, an extinction coefficient of $\epsilon = 150000 \text{ cm}^{-1}\text{M}^{-1}$ was specified for Alexa-555 now $\epsilon = 155000 \text{ cm}^{-1}\text{M}^{-1}$ is published. The same happened to the extinction coefficient of Alexa-647 which changed from $\epsilon = 239000 \text{ cm}^{-1}\text{M}^{-1}$ to $\epsilon = 270000 \text{ cm}^{-1}\text{M}^{-1}$. I will use the earlier values, as specified at the date of purchase. Although

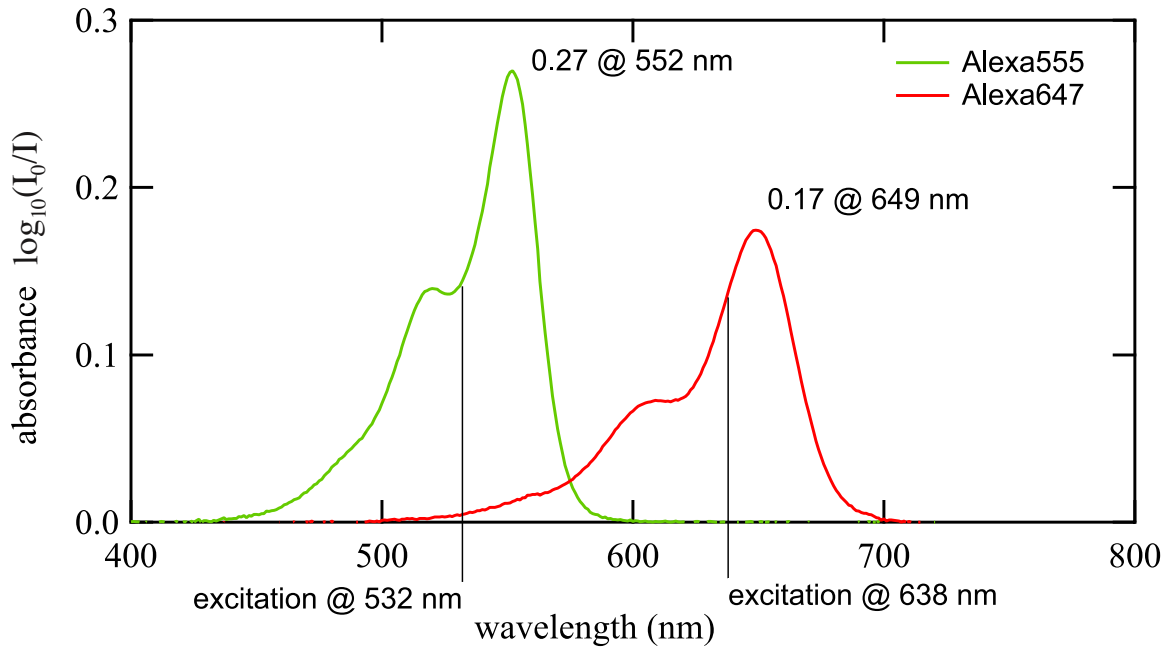


Fig. 4.1: Absorption spectra of Alexa-555 and Alexa-647 solved in PBST. The vertical lines mark the excitation wavelength used in the FRET experiments. Note that the absorbance depends on the sample concentrations ($c_{Alexa555} = 0.78 \mu M$ and $c_{Alexa647} = 0.31 \mu M$)

the measurements were performed in PBST, the MeOH extinction coefficients are used since extinction coefficients for PBST could not be found. For the later FRET experiments only the relative absorption cross sections of both dyes are of interest and the change due to the solvent is expected to be equally for both dyes.

Figure 4.2 shows the fluorescence emission spectra of both dyes, as measured with a custom built fluorometer, available in our laboratory. The emission spectrum of Alexa-555 was measured with excitation at 543 nm (at 79% of the absorption maximum) and Alexa-647 was excited at 633 nm (at 65% of the absorption maximum). The extinction coefficients at the excitation wavelengths are $\epsilon = 118500 \text{ cm}^{-1} M^{-1}$ for Alexa-555 and $\epsilon = 155350 \text{ cm}^{-1} M^{-1}$ for Alexa-647. Considering the concentrations, the quantum efficiency of Alexa-555 is only 69% of the quantum efficiency of Alexa-647.

The tabulated emission maxima of Alexa-555 and Alexa-647 [122] are at 565 nm and 665 nm . While the fluorescence emission curves in figure 4.2 reproduce the maximum for Alexa-555 the maximum of Alexa-647 is red shifted by 2 nm. Interestingly also the position of the fluorescence emission maxima of both fluorophores changed on the Molecular Probes website now listing 572 nm as emission maximum for Alexa-555 and 672 nm for Alexa-

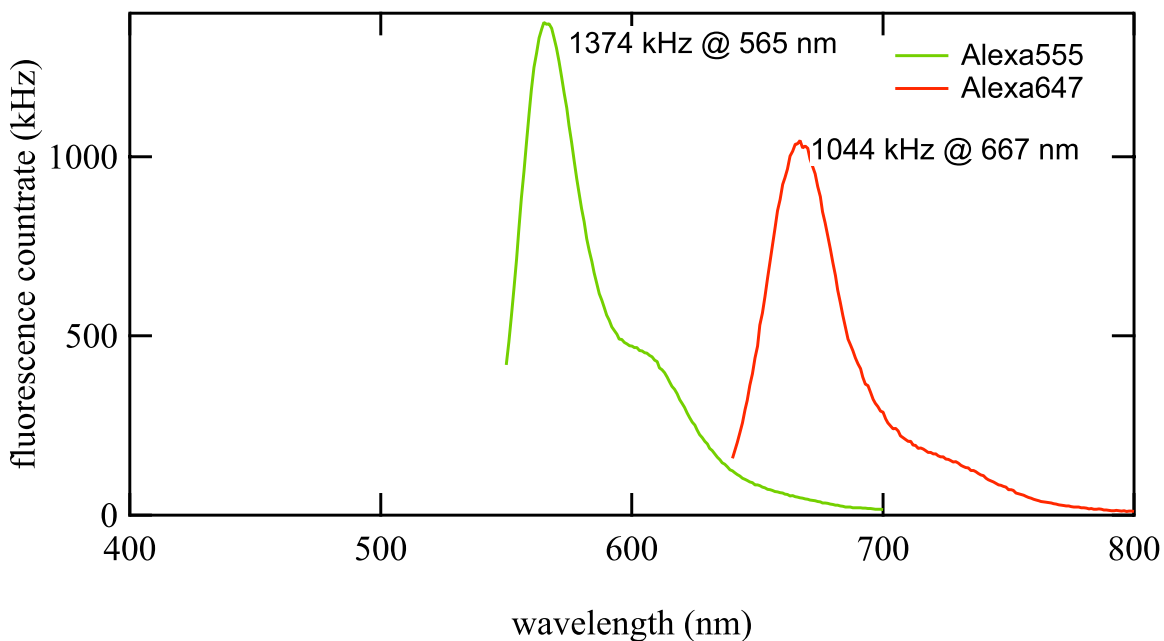


Fig. 4.2: Fluorescence spectra of Alexa-555 and Alexa-647 solved in PBST. Note that the sample concentrations are different ($C_{Alexa555} = 0.78 \mu M$ and $C_{Alexa647} = 0.31 \mu M$)

647 [121].

4.1.3 Structure of Poly-L-Proline

Figure 4.3 shows the structure of the four different poly-L-proline molecules with their according linkers. The fluorophores are not shown since their structural formula is kept secret. The structure of poly-L-proline has first been analyzed by Cowan et al. [120] in 1955. From x-ray diffraction analysis the length per residue was found to be 0.31 nm.

The contour lengths of the poly-L-proline peptides from the N-terminal group (NH_2) of glycine to the C-terminal Group (SH) of cysteine were modeled in water with AMBER97² [123, 124] and found to be 2.13 nm, 4.07 nm, 5.94 nm and 7.90 nm for P06, P12, P18 and P24 respectively. Those contour lengths are not in accordance with the findings from Cowan et al. [120] since they are not multiples of the 0.31 nm per residue. The length of the residue, however, was deducted from a crystallographic study in this reference and does not include additional terminal groups. Based on the modeling I propose the following expression for the contour length (l_c) of the used poly-L-proline spacers in dependence of the number of

² AMBER is a molecular dynamics simulation package.

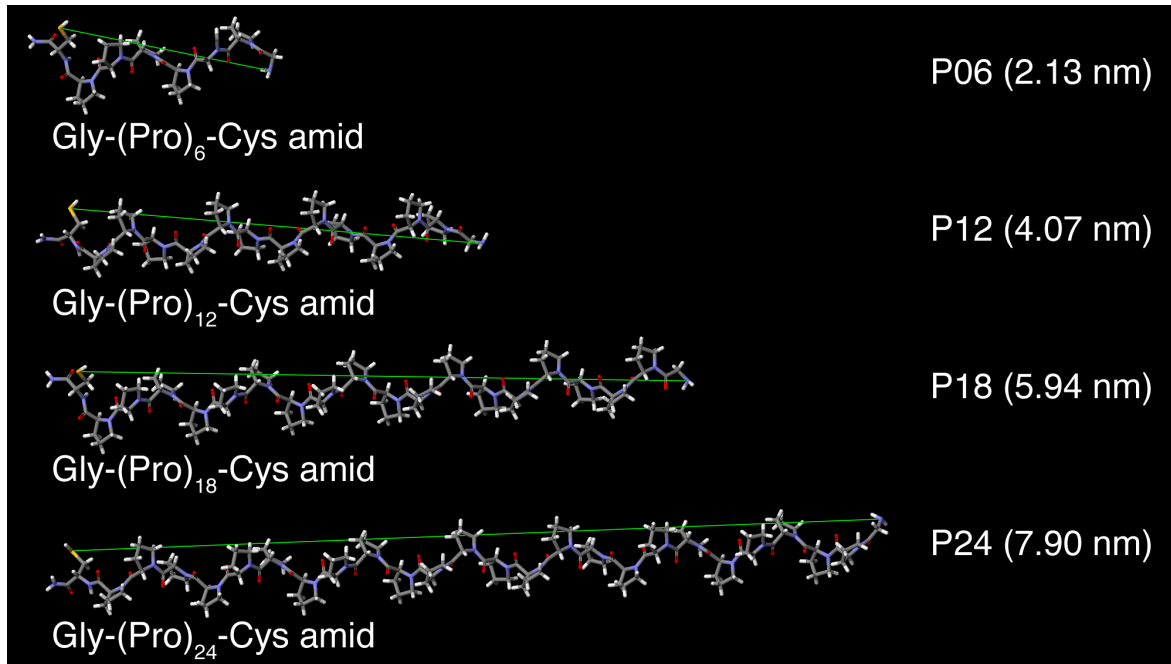


Fig. 4.3: Molecular structure of the poly-L-proline molecules used. The distances are the contour lengths (between N-terminal coupling group (NH_2) of glycerine and C-terminal coupling group (SH) of cysteine) as determined by molecular modeling with AMBER97.

residues k :

$$l_c = (0.22 + k \cdot 0.32) \text{nm}. \quad (4.1)$$

The offset is attributed to the terminal groups and I consider the 0.32 nm found for the length of one poly-L-proline residue in sufficient accordance with the crystallographic study mentioned above.

Very recently, molecular modeling findings [116] suggested that poly-L-proline is not as rigid as stated before [112, 117].

4.1.4 Dynamics of Poly-L-Proline - Worm-Like Chain Model

Because FRET efficiencies found for large poly-L-proline molecules were considerably larger than expected when treated as a rigid rod, Langmuir molecular dynamics simulations of poly-L-prolines with varying length were undertaken by Schuler et al. [116]. The calculations show that the longer peptides are quite flexible, with end-to-end distance distributions shorter than the contour lengths. The relaxation times of the distance fluctuations were found to vary between 0.2 ns (P10) to 2 ns (P25).

Poly-L-proline therefore cannot be described as a rigid rod instead it can be described

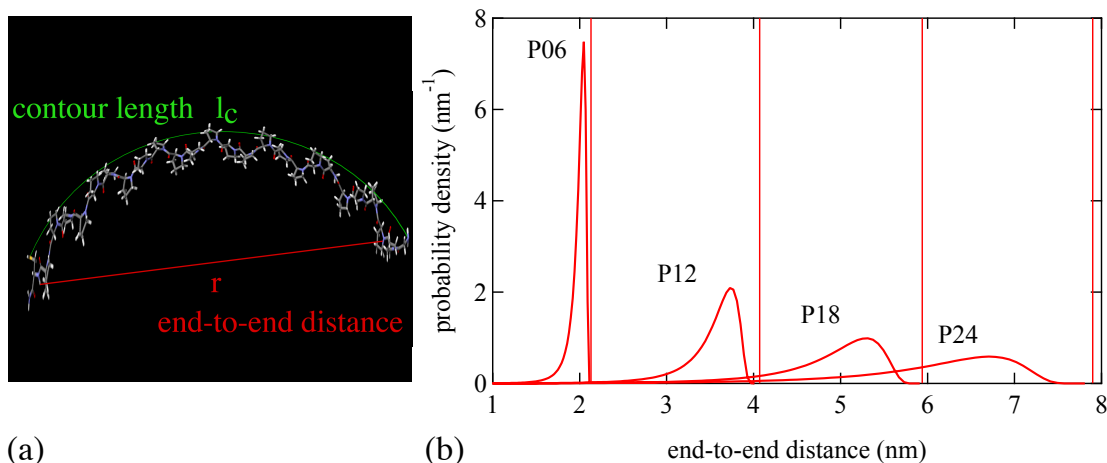


Fig. 4.4: (a) Illustration of contour length l_c and end-to-end distance r . (b) End-to-end distance distribution for a worm-like chain according to (4.2) for the four poly-L-proline spacers used. The vertical lines mark the contour lengths l_c . The average of all distributions is shifted towards shorter end-to-end distances as compared to the contour lengths.

better by a worm-like chain model. In this model the end-to-end distance r of the molecule is no longer fixed at the contour length l_c . The difference between l_c and r is visualized for a bent P24 molecule in figure 4.4a. The end-to-end distributions found in the simulations could be fitted with the following equation given by Thirumalai and Ha [125]:

$$P(r) = \frac{4\pi N r^2}{l_c^2 [1 - (r/l_c)^2]^{9/2}} \exp\left(-\frac{3l_c}{4l_p [1 - (r/l_c)^2]}\right) \quad (4.2)$$

yielding a persistence length of $l_p = (4.4 \pm 0.9)$ nm, significantly less than the 22 nm mentioned in textbooks [112, 117]. N is a normalization constant. The persistence length l_p is defined as the average projection of the end-to-end distance vector \vec{r} on the first bond of the chain, in the limit of infinite chain length. The persistence length is a measure of the length over which the chain persists in the same direction as the first bond and is closely related to the "stiffness" of the chain. Figure 4.4b shows the end-to-end distance distributions according to (4.2) for the four poly-L-prolines used.

While the end-to-end distance distribution for P06 is relatively narrow, for P24 the distribution is rather broad. The vertical lines indicate the contour lengths of the four poly-L-prolines under investigation. From figure 4.4b it becomes evident that, even if dynamic effects can be neglected, the average end-to-end distance will be smaller than the contour length. The difference between the average end-to-end distance and the contour length increases with

the number of residues.

4.2 Sample Preparation and Experimental Details

sample preparation

The dyes were supplied by Molecular Probes, Eugene, USA. The poly-L-proline peptides were synthesized per fmoc-technique and automatic multiple synthesis by Biosyntan, Berlin, Germany. Purity of the peptide samples was tested to be 95% by High Performance Liquid Chromatography (HPLC) and Mass Spectroscopy (MS).

The coupling of the fluorophores was done by my collaborators at the Robert-Koch Institute Berlin. First the acceptor fluorophore (Alexa-647, thiol-conjugate) was coupled to the N-terminal group (NH₂ of glycine). This avoids dimerization of the peptides. Size exclusion-HPLC was subsequently used to purify the product before in a second step the donor fluorophore (Alexa-555 maleimide) was coupled to the C-terminal group (SH) of cysteine. Size exclusion-HPLC and reverse phase-HPLC was used to purify the product and to exclude incompletely coupled molecules.

For the experiments the samples were diluted with PBST to concentrations between 20 pM and 150 pM to have statistically not more than one molecule inside the confocal volume at a time. The real number of molecules present in the focal volume was monitored by FCS during the experiment³.

experimental details

All experiments were performed on the confocal fluorescence microscope (Microtime 200, PicoQuant GmbH Berlin, Germany), described in section 2.3. The acceptor was excited using a picosecond diode laser (LDH-P-C-635B, PicoQuant GmbH, Berlin, Germany) with a wavelength of 638 nm (550 μ W average power at the sample). For excitation of the donor a pulsed amplified and doubled picosecond diode laser (PicoTA, PicoQuant GmbH Berlin, Germany) with an output wavelength of 532 nm (150 μ W average power at the sample) was used. Narrow band cleanup filters ensured that only light within the desired excitation

³ In contrast to conventional FCS measurements on FRET samples, FCS combined with PIE delivers the number of particles within the confocal volume even in the presence of FRET because the FCS analysis is done on donor and acceptor molecules separately.

band reached the sample. The repetition rate was set to 40 MHz for each laser. For pulsed interleaved excitation the 532 nm laser pulse was delayed by about 12.5 ns with respect to the 638 nm pulse to generate a sequence of pulses with alternating wavelengths. A dual band dichroic beam splitter with high reflectivity at 532 nm and 638 nm reflected the light to a high numerical aperture apochromatic objective (60x, NA 1.2, water immersion, Olympus, Japan) which finally focused the light to an confocal volume of 0.49 fl (0.69 fl) for excitation with 532 nm (638 nm) and detection at (575 ± 15) nm ((685 ± 35) nm). Fluorescence from excited molecules was collected with the same objective and focused with an achromatic lens ($f = 175$ mm) onto a $50\ \mu\text{m}$ diameter pinhole to achieve confocal detection. The donor and acceptor emissions were separated using a dichroic long pass filter with the dividing edge at 640 nm. Bandpass filters (HQ685/70 for acceptor, HQ575/30 for donor emission, both Chroma Technology Corp., Brattleboro, VT, USA) ensured further spectral separation. The fluorescence photons were detected with two Single Photon counting Avalanche Diode modules (SPADs) (SPCM-AQR-14, Perkin Elmer Inc., Santa Clara, Ca, USA), and signal processing was done using a TimeHarp 200 TCSPC PC-card (Picoquant GmbH, Berlin, Germany). The data were stored in the Time Tagged Time Resolved (t3r) format, allowing the recording of every detected photon with its individual timing and detection channel information, which is the basis for the following analysis. The measurements presented were performed approximately $10\ \mu\text{m}$ deep inside the solution with a total acquisition time of 20 minutes to assure good statistics.

A typical measuring protocol includes several supporting measurements for setup and sample characterization.

1. Measurement of the Instrument Response Function (IRF) (see section 2.5.2)
2. Measurement of size and shape of the confocal volume (see section 2.6)
3. Measurement of the solvent background count rate
4. Measurement of singly-labeled samples and quantification of molecular brightness
5. Measurement of the FRET sample

4.3 FRET Analysis

The energy transfer efficiency can be measured by analyzing the decrease of the donor excited state lifetime due to the additional relaxation channel provided by the energy transfer process or by measuring the fluorescence intensity ratio of the donor and acceptor fluorophore.

4.3.1 Fluorescence Lifetime FRET

One way to obtain the energy transfer efficiency of a FRET pair is to measure the donor fluorescence lifetime in presence and absence of an acceptor fluorophore. The determination of the fluorescence lifetime has been described in section 2.5.4. The fluorescence lifetime of the donor decreases due to the additional relaxation channel provided by the energy transfer. The fluorescence lifetime of the donor in absence of an acceptor is:

$$\tau_D = \frac{1}{k_F + k_i} = \frac{{}^DQ}{k_F}. \quad (4.3)$$

DQ is the quantum efficiency of the donor in absence of an acceptor, k_F the rate constant of the fluorescence process and k_i represents all other relaxation processes. If an acceptor is in close proximity, an additional relaxation channel k_T is provided by FRET and consequently the lifetime of the excited state decreases:

$$\tau_{DA} = \frac{1}{k_f + k_i + k_T} = \frac{{}^{DA}Q}{k_F}. \quad (4.4)$$

${}^{DA}Q$ denotes the quantum efficiency of the donor in presence of an appropriate acceptor molecule. With equation 1.4 (section 1.1.1) the transfer efficiency can be expressed as the ratio of the donor lifetime in absence and presence of an acceptor fluorophore:

$$E = 1 - \frac{\tau_{DA}}{\tau_D}. \quad (4.5)$$

4.3.2 Burst Detection

Since we work in the single molecule regime, most of the time there is only solvent molecules in the confocal volume, thus most of the recorded signal only consists of background. If a FRET pair diffuses through the confocal volume, a number of fluorescence photons are detected,

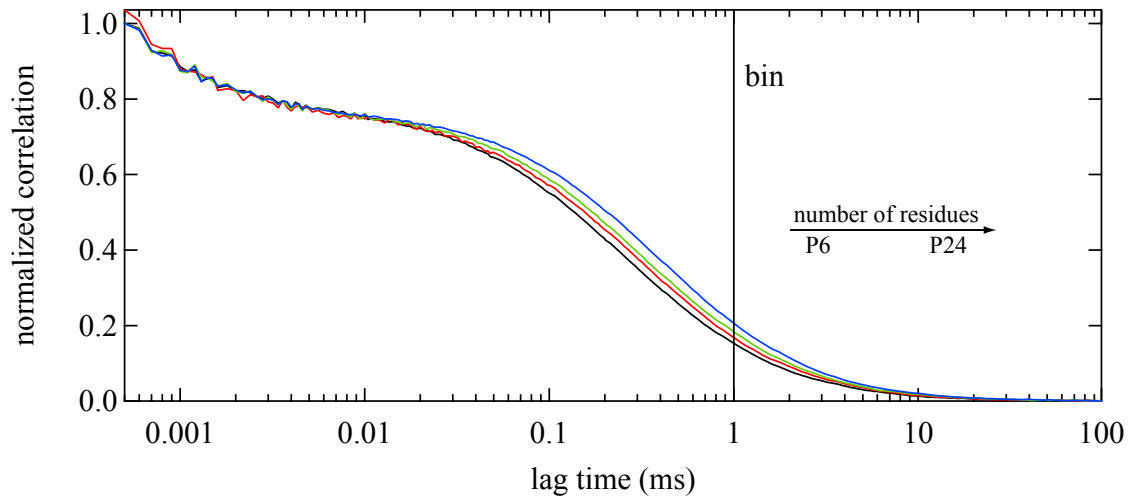


Fig. 4.5: Normalized FCS spectra of the four poly-L-prolines labeled with donor and acceptor. The acceptor was excited directly and the fluorescence signal was collected from the acceptor detection channel. Therefore the shown FCS spectra are not influenced by FRET. The diffusion time increases with the length of the poly-L-proline spacers. Since poly-L-proline has a stick-like shape, the increase of the diffusion time is stronger as expected for spherical molecules.

whose time intervals are shorter than without a fluorescent molecule. The measurand is the arrival time of these photons. For the calculation of the intensity FRET ratio these photon arrival times are converted into intensity traces by binning. A threshold selects the fluorescence bursts and suppresses the background. When a molecule diffuses through the confocal volume, it generates a photon burst whose duration depends on the size of the confocal volume and on its diffusional velocity. The photons detected within a fixed time span are counted. The time span has to be chosen larger than the diffusion time but not too large as background contribution increases with increasing integration time. Additionally the risk of summing up photons of two independent bursts and therefore of two independent molecules increases with increasing binning time which finally would cause us to leave the single molecule regime. On the other hand, if the bin size is chosen too short, bursts are split into two different bins and interpreted as two subsequent events with lower intensity. Figure 4.5 shows the normalized FCS spectra of the four poly-L-prolines. The diffusion time, and therefore the burst duration varies between (0.255 ± 0.001) ms and (0.385 ± 0.001) ms. A binning time of 1 ms was chosen, as indicated by the vertical line in figure 4.5. This bin size is about a factor of two larger than the average time a molecule spends in the confocal region.

4.3.3 Fluorescence Intensity FRET

If the acceptor is not directly excitable, the number of photons emitted per time by one ($^D F'$) donor ($^D F'$) respectively one acceptor ($^A F'$) fluorophore is given by:

$$\begin{aligned} ^D F' &= \phi(\vec{r}) \underbrace{^D \sigma (1 - E) ^D Q}_{^D \sigma ^{DA} Q} \\ ^A F' &= \phi(\vec{r}) ^D \sigma E ^D Q. \end{aligned} \quad (4.6)$$

$\phi(\vec{r})$ is the spatial distribution of the photon flux density with amplitude ϕ_0 (Excitation Intensity Distribution, EID), considered to be constant in time. $^D \sigma$ is the absorption cross section of the donor fluorophore at the excitation wavelength and $E ^D Q$ is the sensitized acceptor quantum yield due to FRET, while $(1 - E) ^D Q$ is the reduced donor quantum yield ($^{DA} Q$) due to the presence of a quenching acceptor. The energy transfer efficiency (see eq. 1.4, section 1.2) for this molecule can then be represented by the respective number of emitted photons:

$$E' = \frac{^A F'}{^D F' + ^A F'}. \quad (4.7)$$

Thus the transfer efficiency can be calculated from the fluorescence count rate of the donor and acceptor fluorophore respectively.

The apparent FRET efficiency - spectral crosstalk

A typical FRET setup involves two detectors, one for detection of the donor emission and one for the detection of the acceptor emission. Since the fluorophores need to be spectroscopically close for the energy transfer to take place, donor fluorescence will not only be detected in the donor detection channel but also in the acceptor detection channel. Furthermore the acceptor, in practice, will also be directly excitable. The number of detected photons per time in the acceptor channel F^A therefore has three different contributions:

$$F^A = \underbrace{^D F^A}_{Lk} + \underbrace{^A F^A}_{Dir} + \underbrace{^{DA} F^A}_{FRET}. \quad (4.8)$$

The upper left index indicates the fluorophore (D for donor, A for acceptor and DA for FRET mediated acceptor emission) whereas the upper right index denotes the detection

channel. Lk stands for donor fluorescence leaking into the acceptor detection channel and Dir stands for the direct excitation of the acceptor fluorophore, while $FRET$ denotes the acceptor fluorescence due to the FRET process. Note that ${}^D F^A$ now denotes the photons detected in the acceptor channel emitted by a donor fluorophore whereas ${}^D F'$ in (4.7) is the number of photons emitted by a single donor fluorophore.

Usually, the first two contributions of (4.8) are non-zero and sources of systematic errors. The donor detection channel, on the other hand, can be chosen to be unsusceptible to acceptor fluorescence:

$$F^D = {}^D F^D . \quad (4.9)$$

Analog to (4.7) we now define the apparent FRET efficiency as the photon count rate of the acceptor detection channel divided by the photon count rate detected in both detection channels:

$$E_{app} = \frac{F^A}{F^D + F^A} \quad (4.10)$$

In contrast to E' as in equation 4.7, E_{app} is an experimentally accessible value. In the presence of spectral crosstalk the apparent FRET efficiency will always be higher than the expected FRET efficiency. This is illustrated in figure 4.6 showing the intensity FRET histogram for donor-only labeled P06. A FRET efficiency of zero would be expected since there is no acceptor fluorophore available. The measured FRET efficiency of about 0.2 is purely due to donor fluorescence leaking into the acceptor detection channel. This example underlines the necessity to quantify the amount of spectral crosstalk.

Let us now concentrate on the apparent FRET efficiency in more detail. The number of photons detected per time can be written as a function of excitation, emission and detection efficiency:

$$F = \phi_0 \langle n \rangle V \cdot \sigma \cdot Q \cdot g . \quad (4.11)$$

ϕ_0 is the photon flux density of the excitation laser (the spatial average of the EID, introduced in section 2.4.1) which can be determined from the laser power measured behind the microscope objective, $P_0 = \phi_0 h\nu A$, where A is the cross sectional area of the laser beam at the focus and $h\nu$ the energy of the incident photon.

$\langle n \rangle$ is the fluorophore number density and V is the confocal volume depending on excitation

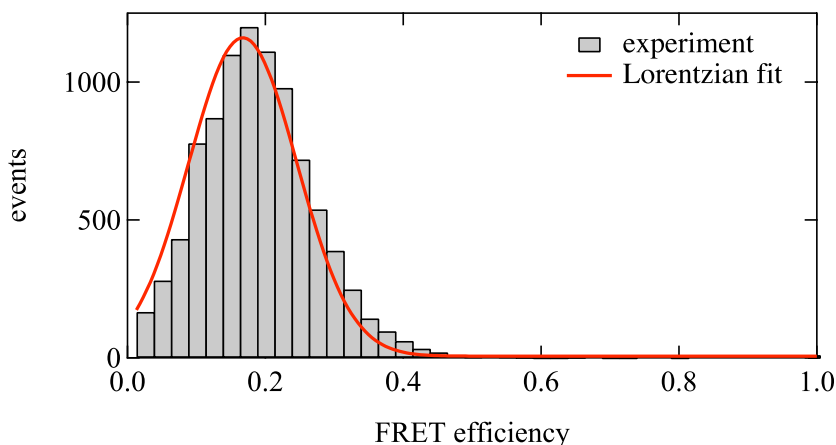


Fig. 4.6: Apparent FRET efficiency distribution of poly-L-proline labeled only with Alexa-555. Although this molecule has no acceptor fluorophore an apparent FRET efficiency of about 0.17 is measured due to spectral crosstalk.

as well as on the detection wavelength.

σ is the absorption cross section which can be derived from the absorption coefficient $\alpha = \sigma \langle n \rangle$ and g , the overall detection efficiency of the entire detection path of a specific detection channel. Since σ , Q and g are not directly observable we substitute their product with the molecular brightness $\sigma Q g / h\nu A = \beta$ introduced in section 3.4. β includes molecular properties of the fluorophore as well as properties of the experimental setup e.g. the overall detection efficiency. Consequently β has to be indicated with two indices, the upper left for either donor or acceptor and the upper right for the detection channel.

The confocal volume V depends on excitation and detection but since only the detection wavelength is different for the two detection channels, we label the confocal volume of the donor detection channel with V^D and the confocal volume of the acceptor detection channel with V^A . We can now rewrite (4.8) and (4.9) as follows:

$$\begin{aligned}
 F^D &= h\nu A \phi [\langle {}^D n \rangle V^D \cdot {}^D \beta^D (1 - E)] \\
 F^A &= h\nu A \phi \underbrace{[\langle {}^D n \rangle V^A \cdot {}^D \beta^A (1 - E)]}_{Lk} \\
 &\quad + h\nu A \phi \underbrace{[\langle {}^A n \rangle V^A \cdot {}^A \beta^A]}_{Dir} \\
 &\quad + h\nu A \phi \underbrace{[\langle {}^{DA} n \rangle V^A \cdot {}^{DA} \beta^A \cdot E]}_{FRET}.
 \end{aligned} \tag{4.12}$$

F is the number of detected fluorescence photons per time but for FRET analysis it is more convenient to count the fluorescence photons per burst. During a burst the number of particles $\langle N \rangle = \langle n \rangle V$ present in the confocal volume equals one if we are in the single molecule regime. The number of photons detected per burst is given by the detected count rate F multiplied by the burst duration T . Instead of the detection volume now the burst duration depends on the detection wavelength and therefore on the detection channel and (4.12) becomes:

$$\begin{aligned}
T^D F^D &= h\nu A \phi [T^D \cdot {}^D\beta^D (1 - E)] \\
T^A F^A &= \underbrace{h\nu A \phi [T^A \cdot {}^D\beta^A (1 - E)]}_{Lk} \\
&\quad + \underbrace{h\nu A \phi [T^A \cdot {}^A\beta^A]}_{Dir} \\
&\quad + \underbrace{h\nu A \phi [T^A \cdot {}^{DA}\beta^A \cdot E]}_{FRET}.
\end{aligned} \tag{4.13}$$

With this equation we can calculate the apparent FRET efficiency:

$$E_{app} = \frac{T^A [{}^D\beta^A (1 - E) + {}^A\beta^A + {}^{DA}\beta^A E]}{T^A [{}^D\beta^A (1 - E) + {}^A\beta^A + {}^{DA}\beta^A E] + T^D [{}^D\beta^D (1 - E)]}. \tag{4.14}$$

(4.14) gives the apparent FRET efficiency one would measure for a fluorescence burst caused by a FRET pair with energy transfer efficiency E .

Without spectral leakage (${}^D\beta^A = 0$) and without direct acceptor excitation (${}^A\beta^A = 0$) we get:

$$E_{app} = \frac{F^A}{F^A + F^D} = \frac{E}{E + 1/\gamma(1 - E)}, \tag{4.15}$$

and therefore

$$E = \frac{F^A}{F^A + \gamma F^D}. \tag{4.16}$$

With $\gamma = T^A {}^{DA}\beta^A / T^D {}^D\beta^D$ being the ratio of the molecular brightness of acceptor and donor in its respective detection channels. This is the conventional formula used in most FRET publications, only valid if spectral crosstalk can be neglected. Figure 4.7 shows the influence of spectral crosstalk as well as different molecular brightness. While leakage and direct

acceptor excitation mainly effects the FRET efficiencies for larger donor-acceptor separations (figure 4.7a), differences in molecular brightness of both fluorophores result in an apparent shifting of R_0 (figure 4.7b). Figure 4.7c shows the increasing deviation of the apparent from the FRET efficiency for increasing amounts of crosstalk and higher molecular brightness of the acceptor fluorophore.

FRET with Pulsed Interleaved Excitation (PIE)

Consider a sample consisting of FRET pairs, i.e. a donor and an appropriate acceptor fluorophore covalently bound to a molecular spacer at a suitable distance of a few nanometers to each other. These molecules are solved in a solvent at sub nanomolar concentration to allow for single molecule detection. Accurate determination of FRET efficiencies may be hampered in this situation by incomplete FRET molecules, namely those molecules which are missing the acceptor fluorophore (donor-only molecules) as well as those missing the donor fluorophore (acceptor-only molecules). Even if both fluorophores are present, it may also happen that one of them is photochemically or photophysically damaged and does not show fluorescence anymore, which means effectively that one of the chromophores is "not present" as above. In FRET-imaging those "broken" pairs can be identified by recording the image at donor excitation wavelength and then recording the same image again at acceptor excitation wavelength. In solutions, however, the average time a molecule needs to pass through the confocal region is in the order of milliseconds or below. Therefore the diffusing molecules have to be probed on a faster time scale with two laser pulses to make sure both measurements are done on the same molecule.

For this purpose pulsed interleaved excitation is applied, i.e. two picosecond laser pulses at different wavelengths are interleaved to excite alternately the acceptor and the donor at a repetition rate chosen that the pulse separation is longer than the fluorescence lifetime of the fluorophores but much shorter than its diffusion time. Time Correlated Single Photon Counting (TCSPC) is used for temporal analysis of the detected photons. Time gating of the detected fluorescence offers the possibility to distinguish between fluorescence excited by the first or the second laser.

Compared to a conventional FRET experiment, where donor and acceptor fluorescence is detected after donor excitation now three different fluorescence photon currents are detected:

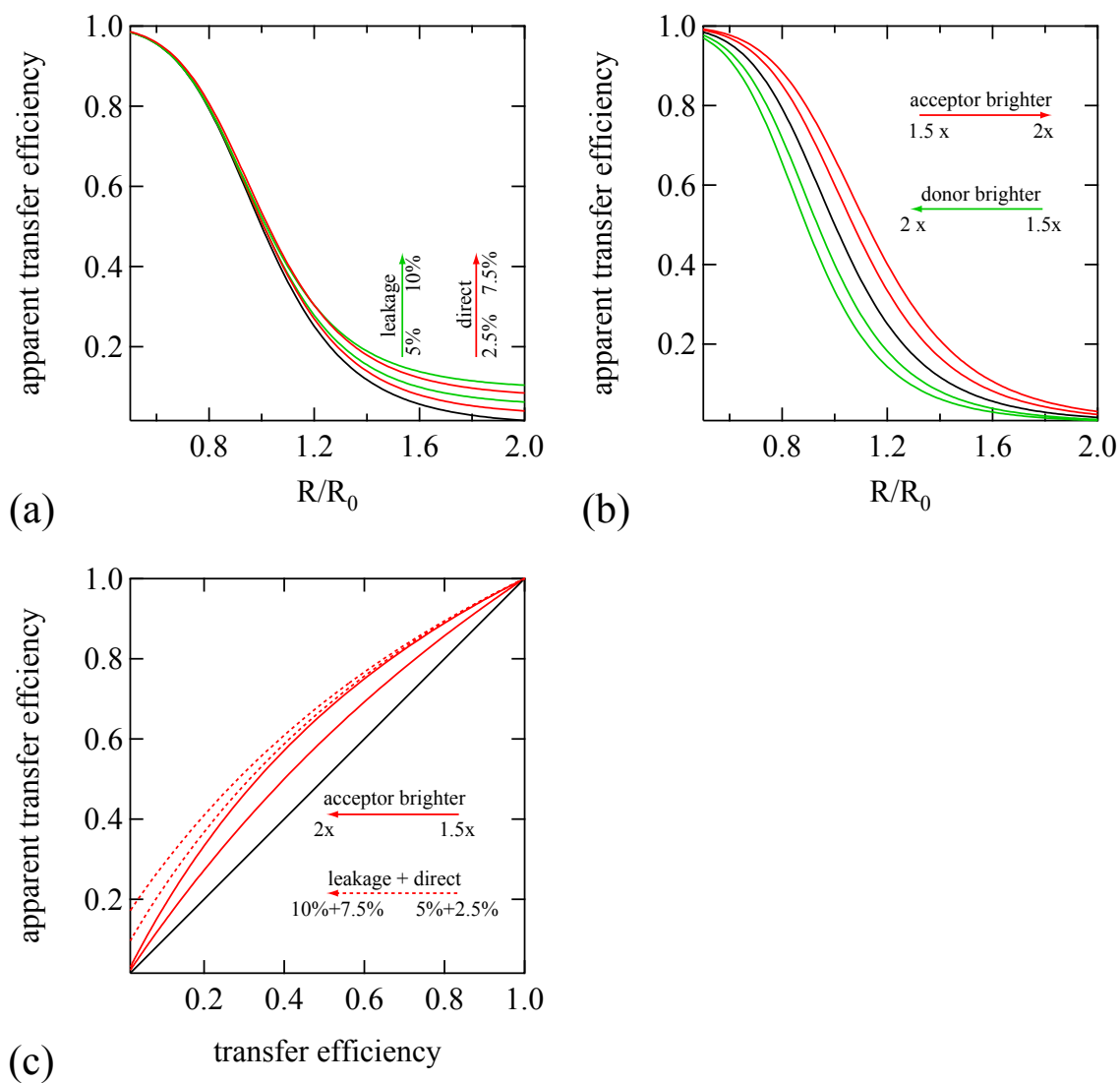


Fig. 4.7: The apparent FRET efficiency for (a) different amounts of spectral crosstalk (leakage and direct acceptor excitation), (b) different ratios of molecular brightness of donor and acceptor in their respective detection channels. (c) shows the increasing deviation of the apparent transfer efficiency from the transfer efficiency for varying amounts of crosstalk and different brightness of donor and acceptor fluorophore

$F_{\lambda_D}^D$, $F_{\lambda_D}^A$ and $F_{\lambda_A}^A$, where the upper index indicates the detection channel as before and the lower index stands for the excitation wavelength, e.g. $F_{\lambda_D}^A$ are the photons detected in the acceptor detection channel following excitation with the donor excitation wavelength (λ_D). The principle of a Pulsed Interleaved Excitation FRET (PIE-FRET) experiment is shown in figure 4.8a - 4.8c. Figure 4.8a shows an intact molecule with a high FRET efficiency, mainly emitting into the acceptor detection channel upon donor excitation ($F_{\lambda_D}^A$). In figure 4.8b on the other hand, the situation for a molecule with low FRET efficiency is shown, i.e. upon donor excitation, fluorescence is mainly detected in the donor detection channel ($F_{\lambda_D}^D$). Without the second laser pulse at λ_A this case would not be distinguishable from the case shown in figure 4.8c where the acceptor molecule is not present or does not fluoresce. Using PIE the acceptor fluorescence emission following excitation at λ_A ($F_{\lambda_A}^A$) can be evaluated and thus figure 4.8b and 4.8c can be distinguished. In the case shown in figure 4.8c no photons are detected upon excitation with λ_A in contrast to figure 4.8b which indicates the absence of a fluorescing acceptor.

The three detected photon currents have the following contributions:

$$\begin{aligned}
 F_{\lambda_D}^D &= {}^D F_{\lambda_D}^D \\
 F_{\lambda_D}^A &= \underbrace{{}^D F_{\lambda_D}^A}_{Lk} + \underbrace{{}^A F_{\lambda_D}^A}_{Dir} + \underbrace{{}^{DA} F_{\lambda_D}^A}_{FRET} \\
 F_{\lambda_A}^A &= {}^A F_{\lambda_A}^A .
 \end{aligned} \tag{4.17}$$

Applying (4.11) and also substituting $\sigma Q g / h\nu A = \beta$ we get the number of detected photons per burst analog to (4.13) in the now three detection channels:

$$\begin{aligned}
 T_{\lambda_D}^D F_{\lambda_D}^D &= h\nu_D A_{\lambda_D} \phi_{\lambda_D} [T_{\lambda_D}^D \cdot {}^D \beta_{\lambda_D}^D (1 - E)] \\
 T_{\lambda_D}^A F_{\lambda_D}^A &= \underbrace{h\nu_D A_{\lambda_D} \phi_{\lambda_D} [T_{\lambda_D}^A \cdot {}^D \beta_{\lambda_D}^A (1 - E)]}_{Lk} \\
 &\quad + \underbrace{h\nu_D A_{\lambda_D} \phi_{\lambda_D} [T_{\lambda_D}^A \cdot {}^A \beta_{\lambda_D}^A]}_{Dir} \\
 &\quad + \underbrace{h\nu A_{\lambda_D} \phi_{\lambda_D} [T_{\lambda_D}^A \cdot {}^{DA} \beta_{\lambda_D}^A \cdot E]}_{FRET} \\
 T_{\lambda_A}^A F_{\lambda_A}^A &= h\nu_A A_{\lambda_A} \phi_{\lambda_A} [T_{\lambda_A}^A \cdot {}^A \beta_{\lambda_A}^A] .
 \end{aligned} \tag{4.18}$$

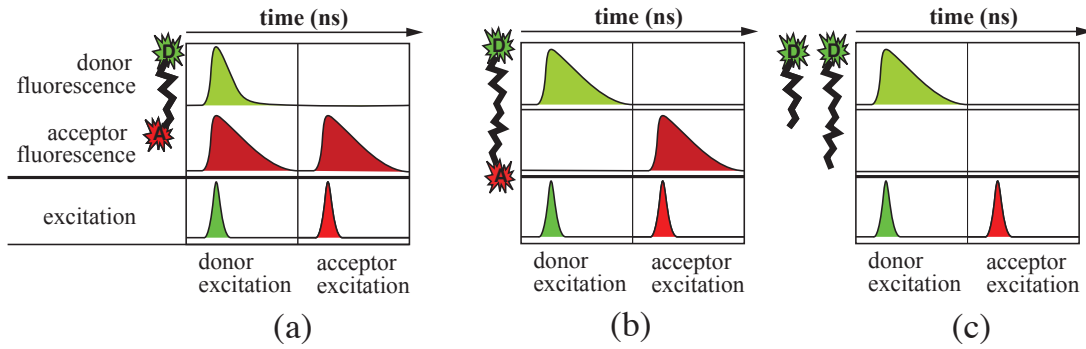


Fig. 4.8: FRET detection with Pulsed Interleaved Excitation (PIE). Within the time the molecule diffuses through the confocal volume it is probed with two lasers subsequently. (a) depicts the case of a molecule with high FRET efficiency where after excitation of the donor acceptor fluorescence can be measured ($F_{\lambda_D}^A$). The fluorescence of the acceptor can be probed independently from the FRET process with the second laser pulse ($F_{\lambda_A}^A$). Molecules with low energy transfer (b) thus can be distinguished from molecules with absent or non fluorescing acceptor (c) where $F_{\lambda_A}^A = 0$.

The apparent FRET efficiency is calculated from the first two photon currents while the third is used for the discrimination of broken and intact FRET pairs, which can then be analyzed independently.

4.4 PIE-FRET Data Analysis

In a conventional FRET experiment donor and acceptor fluorescence is detected, while the donor is excited (see figure 4.9a). When a FRET molecule passes through the confocal volume a fluorescence burst, dependent on the FRET efficiency, is generated in the donor and acceptor detection channel. The arrival times and channel information is stored in a `t3r` file.

For the FRET analysis the arrival times of the photons are converted into an intensity trace by counting the number of detected photons per binning time in both detection channels. A threshold then differentiates between background and an actual single molecule event. This procedure is shown in figure 4.9a. The threshold is applied to the sum of the detected photons, that is, photons in the donor and acceptor detection channel. The FRET efficiency is calculated from the intensities of the selected fluorescence bursts and plotted into a histogram. The problem of this burst selection method is that it tends to favor the brighter fluorophor. The second problem becomes already evident through the appearance of a second unexpected

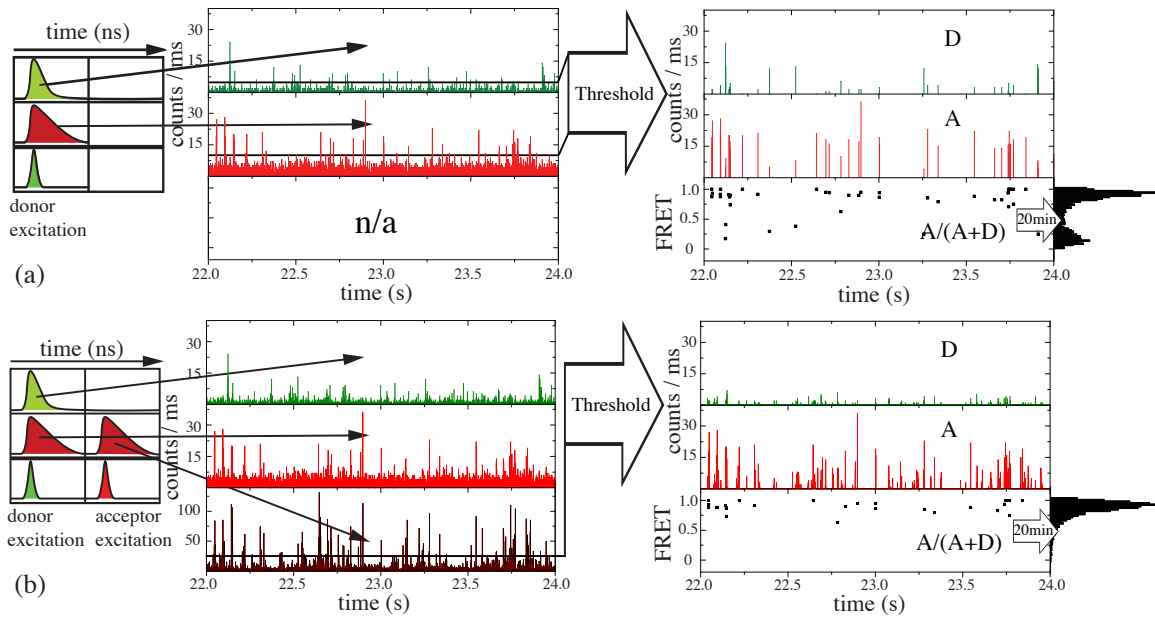


Fig. 4.9: Comparison of the conventional FRET measuring scheme (a) and the PIE-FRET measuring scheme (b). Conventional burst selection is done through thresholding the sum of donor and acceptor fluorescence while the acceptor fluorescence after direct acceptor excitation is used for PIE-FRET burst selection. With the latter only bursts with a functional acceptor fluorophore are selected.

peak in the histogram in figure 4.9a. It is the so called zero-efficiency peak, caused by FRET pairs with a non fluorescing or absent acceptor.

To overcome these limitations, the additional information, one gets through the use of pulsed interleaved excitation is exploited. With PIE the donor and acceptor molecule are excited alternating during the time span the molecule needs to traverse the confocal region. The presence of the acceptor fluorophore therefore can be probed whether FRET takes place or not. Intact FRET pairs show fluorescence in both detection channels (i.e. for donor and acceptor emission) depending on the FRET efficiency following excitation at 532 nm as well as excitation of the acceptor with 638 nm.

To select the intact FRET pairs the recorded $t3r$ data pass a filter which involves a temporary binning of the detected photons with a bin size of 1 ms (see section 4.3.2). This temporal intensity trace allows to identify photon bursts which are above a certain threshold (here 25 cts per bin). Only if a burst is detected in the acceptor channel after excitation at 638 nm (F_{638}^A) (figure 4.9b) all photons recorded during the time span of the bin pass the filter and are considered for further processing. By setting this threshold molecules with large interaction time and hence a larger number of emitted photons are favored.

When performing the experiments, the MicroTime software did not have support for PIE filtering (it is now included in the latest beta version). Therefore I wrote an additional program which parses the `t3r` files and performs the filtering mentioned above. It should be noted that this binning is only temporary so that after filtering the whole information (e.g. photon arrival times with respect to the excitation laser pulse) is still available for those photons which passed the filter. The data remain in the `t3r` format and can then be treated in various ways, like analyzing the fluorescence lifetime, FCS or intensity FRET. Practically the PIE-sorting algorithm converts the original `t3r` data file into two separate `t3r` files, one containing all records of the photons belonging to the bursts that passed the threshold criteria and the other with the records of the remaining photons. Here, the filtered data was loaded into the MicroTime 200 software and treated exactly in the same way as any unfiltered data would be analyzed. One important advantage of this method is that the burst selection criterion is completely independent in respect to the FRET process and thus not biasing the FRET analysis.

With PIE-FRET the differentiation between background and a single-molecule event is done by applying a threshold in the the F_{638}^A channel as compared to the threshold $F_{532}^D + F_{532}^A$ applied in the conventional FRET analysis (see figure 4.9b). Once the single molecule events are selected the following data treatment is exactly the same as for the conventional FRET analysis. The FRET efficiency is calculated from the burst intensities of the donor and acceptor detection channels after excitation with the donor excitation wavelength and likewise plotted into a histogram.

The zero-efficiency peak visible in the histogram of figure 4.9a is not present in figure 4.9b and can thus be attributed to molecules with a missing or non fluorescent acceptor fluorophore.

4.5 Results

In this section the experimental results of the FRET experiments on the poly-L-proline calibration assay are presented and discussed. Finally distance measurements on the TLM molecule are presented and some concluding remarks will be given.

		donor detection channel (575 ± 15 nm)	acceptor detection channel (685 ± 35 nm)
donor excitation (532 nm) confocal volume	lateral (w_0)	$(0.45 \pm 0.02) \mu m$	$(0.46 \pm 0.02) \mu m$
	axial (z_0)	$(2.06 \pm 0.02) \mu m$	$(2.22 \pm 0.02) \mu m$
		$(0.49 \pm 0.06) fl$	$(0.57 \pm 0.06) fl$
acceptor excitation (638 nm) confocal volume	lateral (w_0)	-	$(0.50 \pm 0.02) \mu m$
	axial (z_0)	-	$(2.29 \pm 0.02) \mu m$
		-	$(0.69 \pm 0.07) fl$

Tab. 4.1: Lateral and axial dimensions FWHM of confocal volume measured on fluorescent labeled beads and the respective confocal volumes.

4.5.1 Confocal Volume

The confocal volume has been measured using 100 nm diameter fluorescent beads on a clean cover slide as described in section 2.6.

The resulting axial and lateral dimensions of the confocal volumes are shown in table 4.1 for the three excitation/detection wavelength combinations. The beam waist at the focal point linearly depends on the wavelength. Therefore, the lateral size of the confocal volume is expected to be larger for longer excitation as well as detection wavelengths. From table 4.1 it becomes clear that the lateral dimension of the confocal volume is almost not influenced by the detection wavelengths. While the ratio of the detection wavelengths is 1.19, w_0 only increases by 2%, a small increase, given the uncertainty of 4%. The axial size of the confocal volume (z_0) shows a stronger dependence on the detection wavelength as z_0 of the acceptor detection channel is about (8%) larger than z_0 of the donor detection channel. The lateral size of the confocal volume on the other hand, is more influenced by the excitation wavelength as becomes evident comparing w_0 for the acceptor detection channel after excitation at 532 nm and 638 nm. I therefore conclude that, as expected, the confocal pinhole is influencing the axial resolution stronger than the lateral resolution.

4.5.2 Background

The background signal obviously can hamper the accurate analysis of the transfer efficiency, especially if its contribution is different in different detection channels. Therefore a sample containing solvent only was measured under the exact same conditions the FRET samples were measured. Table 4.2 shows the related count rates for both detection channels after

(solvent)	donor detection channel (575 ± 15 nm)	acceptor detection channel (685 ± 35 nm)
donor excitation (532 nm)	(0.23 ± 0.02) kHz	(2.52 ± 0.05) kHz
acceptor excitation (638 nm)	(0.05 ± 0.01) kHz	(1.36 ± 0.04) kHz

Tab. 4.2: Background count rates measured on a sample containing only solvent.

excitation at 532 nm and 638 nm respectively. Striking is the large amount of background detected following the excitation at 532 nm. The fact that the background is almost only detectable in the acceptor detection channel indicates that this background mostly stems from inelastic scattering of the excitation light at the solvent molecules. Analyzing the solvent data with FCS no correlation is found from which I conclude that the solvent is not contaminated by dye molecules (see figure 4.10b). Figure 4.10a shows the lifetime histogram for the donor (green) and acceptor (red) detection channel. For comparison the IRF is also shown in black. The lifetime histogram of the solvent measurement very much resembles the IRF. Clearly the background stems not from fluorescence but is completely correlated to the excitation at 532 nm. The background found in the acceptor detection channel is most likely due to Raman scattering of the 532 nm excitation laser at water molecules. Although the Raman cross section is about 8 fold smaller than the cross section for fluorescence, the sheer number of water molecules compared to a single fluorescent molecule makes the Raman scattering significant.

4.5.3 Donor-Only and Acceptor-Only Labeled Poly-L-Proline

The molecular brightness $\langle\beta\rangle$ is obtained from donor-only and acceptor-only molecules and since it has a strong influence on the apparent FRET efficiency it needs to be measured exactly, hence a large number of bursts from singly-labeled molecules need to be collected. Although all FRET samples contained a fraction of donor-only and acceptor-only molecules, from which the respective molecular brightness can be deducted, I decided to additionally measure singly-labeled samples with a higher concentration than that of the actual samples (It is not necessary to measure the singly-labeled samples in the single-molecule regime since only one species is contained in the sample). Tables 4.3 and 4.4 show the measured average

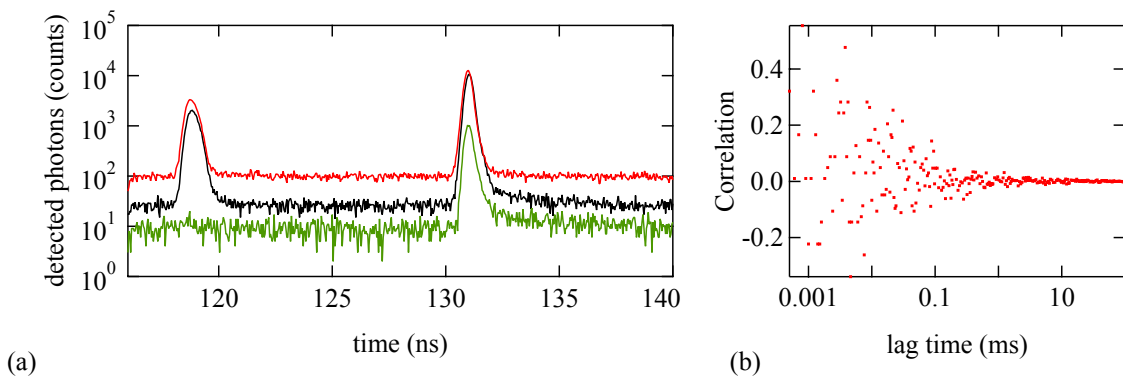


Fig. 4.10: (a) The lifetime histogram of the solvent (green and red lines) shows no indication of fluorescence as it very much resembles the IRF (black line). The first pulse correlates with the acceptor excitation (638 nm) while the second pulse results from the donor excitation laser (532 nm). Note that while exciting with 532 nm (second pulse) the signal detected in the acceptor detection channel is larger than the signal detected in the donor detection channel. (b) FCS of the solvent used. No correlation is visible thus suggesting that the sample is not polluted by diffusing dye molecules

(Alexa-555 - P06)	donor detection channel (575 ± 15 nm)	acceptor detection channel (685 ± 35 nm)
donor excitation (532 nm)	(7.71 ± 0.10) kHz	(1.42 ± 0.11) kHz
acceptor excitation (638 nm)	(0.04 ± 0.02) kHz	(0.28 ± 0.08) kHz

Tab. 4.3: Average count rates $\langle f \rangle$ of donor-only labeled poly-L-proline (6 residues). The background (see table 4.2) by the solvent and other scattering has been subtracted

count rates due to the fluorophore which are calculated by subtracting the average count rate of the solvent $\langle b \rangle$ (see table 4.2) from the average count rate detected in the respective channel $\langle F \rangle$ for both singly-labeled samples:

$$\langle f \rangle = \langle F \rangle - \langle b \rangle. \quad (4.19)$$

The average number of particles $\langle N \rangle$ present in the confocal volume is calculated from the amplitude of the autocorrelation function G_0 as described in sections 1.3.3 and 3.2.1.

As stated above, the advantage of the additional measurement of singly labeled poly-L-prolines is that the concentration of the sample does not need to be in the single molecule region, allowing to achieve better statistics in a shorter acquisition time. The number of particles in the confocal volume was found to be $\langle N \rangle = 1.35 \pm 0.04$ molecules for the donor-

(P06 - Alexa-647)	donor detection channel (575 ± 15 nm)	acceptor detection channel (685 ± 35 nm)
donor excitation (532 nm)	(0.14 ± 0.03) kHz	(2.26 ± 0.12) kHz
acceptor excitation (638 nm)	(0.01 ± 0.01) kHz	(139.14 ± 0.41) kHz

Tab. 4.4: Average count rates $\langle f \rangle$ of acceptor-only labeled poly-L-proline (6 residues). The background (see table 4.2) by the solvent and other scattering has been subtracted

	donor detection channel (575 ± 15 nm)	acceptor detection channel (685 ± 35 nm)
Alexa-555 - P06		
donor excitation	$^D\beta_{532}^D = 38 \pm 5$	$^D\beta_{532}^A = 7.0 \pm 1.5$
acceptor excitation		
P06 - Alexa-647		
donor excitation		$^A\beta_{532}^A = 4.2 \pm 0.7$
acceptor excitation		$^A\beta_{638}^A = 71 \pm 8$

Tab. 4.5: Molecular brightnesses in kHz per molecule and mW of Alexa-555 and Alexa-647 coupled to poly-L-proline after excitation with 532 nm and 638 nm and detection in both detection channels.

only labeled sample and $\langle N \rangle = 3.56 \pm 0.01$ molecules for the acceptor-only sample. Now the molecular brightness of both fluorophores coupled to poly-L-proline can be calculated according section 3.4:

$$\beta = \frac{\langle f \rangle}{\langle N \rangle P}, \quad (4.20)$$

where P denotes the laser power. The resulting molecular brightness are given in counts per ms per molecule and per mW laserpower in table 4.5. It becomes evident that the acceptor is almost two times brighter than the donor fluorophore. The molecular brightness of the acceptor, listed in table 4.5 is the molecular brightness of the acceptor after excitation at 638 nm, but for the FRET analysis the interesting molecular brightness is that of the acceptor due to FRET mediated excitation $^{DA}\beta_{532}^A$. With the knowledge of the excitation spectra of both fluorophores this parameter however is easy to calculate from $^A\beta_{638}^A$:

$$^{DA}\beta_{532}^A = \frac{^D\sigma_{532}}{^A\sigma_{638}} \frac{h\nu_{638}A_{638}}{h\nu_{532}A_{532}} \cdot ^A\beta_{638}^A, \quad (4.21)$$

since β for one molecule ($\langle N \rangle = 1$) can be written as⁴

$$\beta = \frac{\sigma Q g}{h\nu A}. \quad (4.22)$$

For the experiments of this work $\frac{h\nu_{638}A_{638}}{h\nu_{532}A_{532}}$ was close to unity and ${}^{DA}\beta_{532}^A = \frac{{}^D\sigma_{532}A}{A\sigma_{638}}\beta_{638}^A$ is assumed in the further analysis. ${}^D\sigma_{532}/A\sigma_{638} = 51\%/71\%$ and therefore ${}^{DA}\beta_{532}^A = 51$ kHz per molecule and per mW laser power. The detected fluorescence from FRET mediated acceptor emission is still almost 35% brighter than the detected donor fluorescence (${}^D\beta_{532}^D = 38 \pm 5$).

4.5.4 Alexa-555 - Poly-L-Proline - Alexa-647

The four different poly-L-prolines, labeled with donor and acceptor fluorophore were diluted to pico-molar concentrations to assure that only one molecule can be found in the confocal volume at a time. Intensity FRET as well as FRET efficiencies from fluorescence lifetime measurements were measured for all four poly-L-proline spacers.

For the intensity based FRET analysis the transfer efficiency of every burst was calculated from the ratio of the detected acceptor fluorescence photons and the number of photons detected in both detection channels. No corrections besides background subtraction was applied.

$$E_{meas} = \frac{\langle F_{532}^A \rangle - \langle b_{532}^A \rangle}{(\langle F_{532}^A \rangle - \langle b_{532}^A \rangle) + (\langle F_{532}^D \rangle - \langle b_{532}^D \rangle)} \quad (4.23)$$

F_{532}^A is the number of photons detected per bin interval in the acceptor detection channel after excitation with 532 nm. Likewise F_{532}^D is the number of photons detected per bin interval in the donor detection channel, again after excitation at 532 nm.

During the experiment the arrival times of the detected photons were recorded. For the FRET intensity analyses the arrival times were converted into intensity traces. The bin size was set to 1 ms (see section 4.3.2). Bursts originating from single molecules traversing the confocal volume were then selected by applying a threshold criteria. For the conventional FRET analysis the sum of donor and acceptor detection (after donor excitation) must exceed 25 counts per bin ($F_{532}^D + F_{532}^A > 25$) and for PIE-FRET each burst must contain at least 25 detected photons in the acceptor channel after direct acceptor excitation ($F_{638}^A > 25$). To eliminate bursts caused by molecules without an intact donor molecule the threshold used in

⁴ $\beta = \frac{\langle f \rangle}{\langle N \rangle P} = \frac{\phi_0 \sigma Q g}{1 \cdot \phi_0 h\nu A}$, with $\langle N \rangle = 1$

the conventional analysis was also applied in the PIE-FRET analysis.⁵

The FRET histograms obtained from the four different poly-L-proline spacers are shown in figure 4.11 and 4.12. While usually the shown FRET histograms already include corrections I here intentionally present the uncorrected data to keep the uncertainties low. To calculate the actual distance between the fluorophores those corrections can later be applied to the extracted average FRET efficiency $\langle E \rangle$. Figure 4.11 displays the FRET histograms achieved with the conventional method of analysis in contrast to figure 4.12 where the information gained by PIE has been used to sort out FRET molecules with an absent or non fluorescing acceptor.

The zero efficiency peak is clearly suppressed by the PIE selection in figure 4.12, hence the zero efficiency peak is obviously connected with molecules with absent or non fluorescing acceptor. Besides removing the zero efficiency peak the filtering does not alter the distribution of the FRET efficiencies.

With increasing donor-acceptor separation the transfer efficiency distribution shifts towards lower efficiencies. For P24 the transfer efficiency distribution has already a considerable overlap with the zero efficiency peak, if the PIE selection is not performed.

The widths of the FRET efficiency distributions are given by photon statistics, i.e. the limited number of photons collected per burst. If the uncertainty of the number of collected photons is estimated assuming Poisson statistics, i.e. as given by the square root of the number of photons per burst, the FRET efficiency distribution widths are readily reproduced. This means that the donor-acceptor distances are not fluctuating on a time scale large compared to the diffusion time.

FRET efficiencies were also determined from the decrease of the donor fluorescence lifetime (see section 4.3.1). Unfortunately, because of the limited number of photons collected per burst, the determination of the transfer efficiency via a donor fluorescence lifetime analysis was only possible for the ensemble. However, even ensemble lifetime analysis profits from PIE because it can be performed on the sorted molecules. The donor-only fluorescence lifetime has been measured on FRET molecules detected with an absent or non fluorescing acceptor in a PIE experiment as 0.45 ns. This value was obtained as well in the control experiment on molecules labeled with only a donor fluorophore. Since the measured lifetime

⁵ The FRET data analysis is explained in more detail in section 4.4

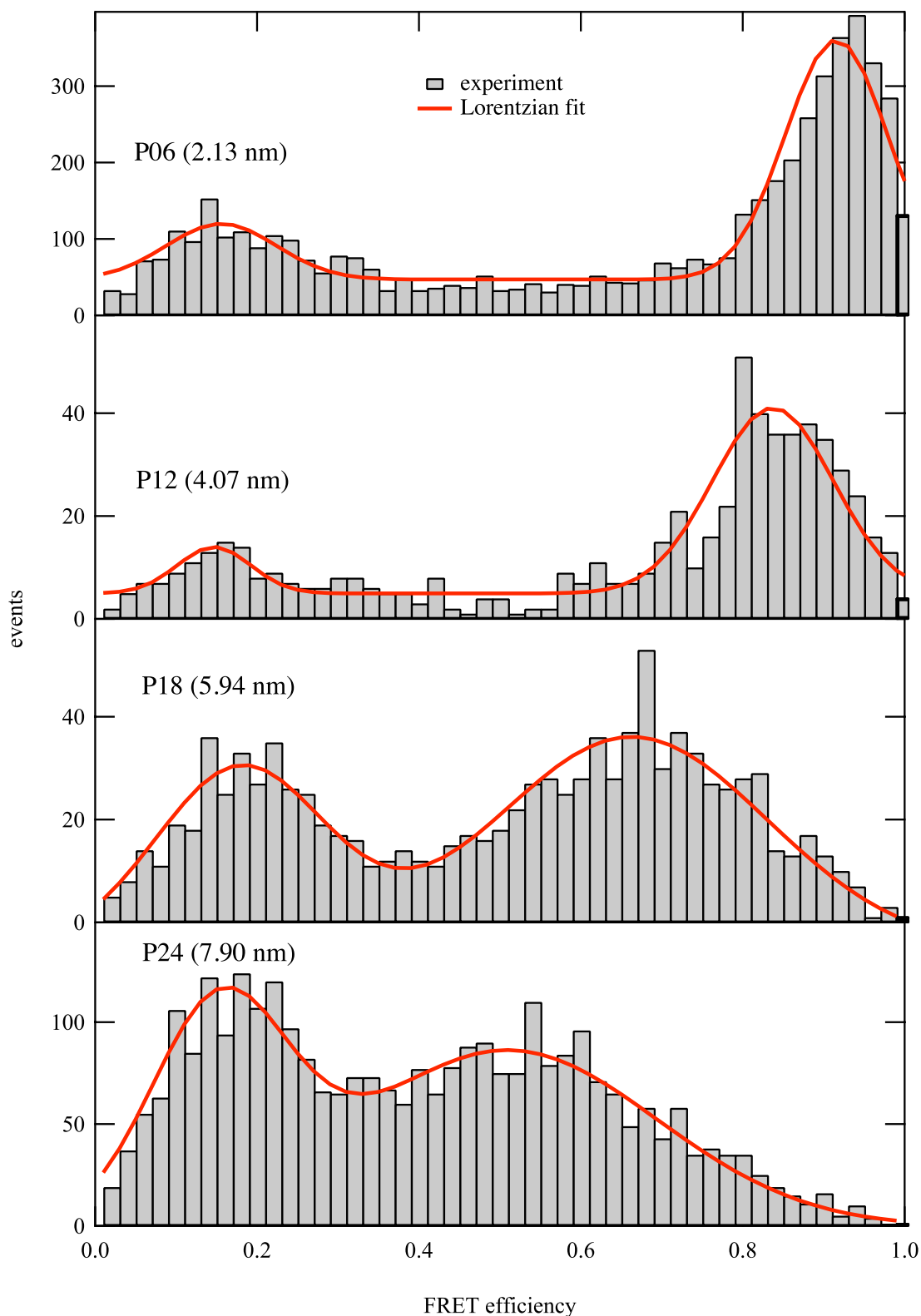


Fig. 4.11: Conventional FRET histograms for different lengths of poly-L-proline labeled with Alexa-555 and Alexa-647 as donor and acceptor respectively. The zero efficiency peak is visible for all lengths.

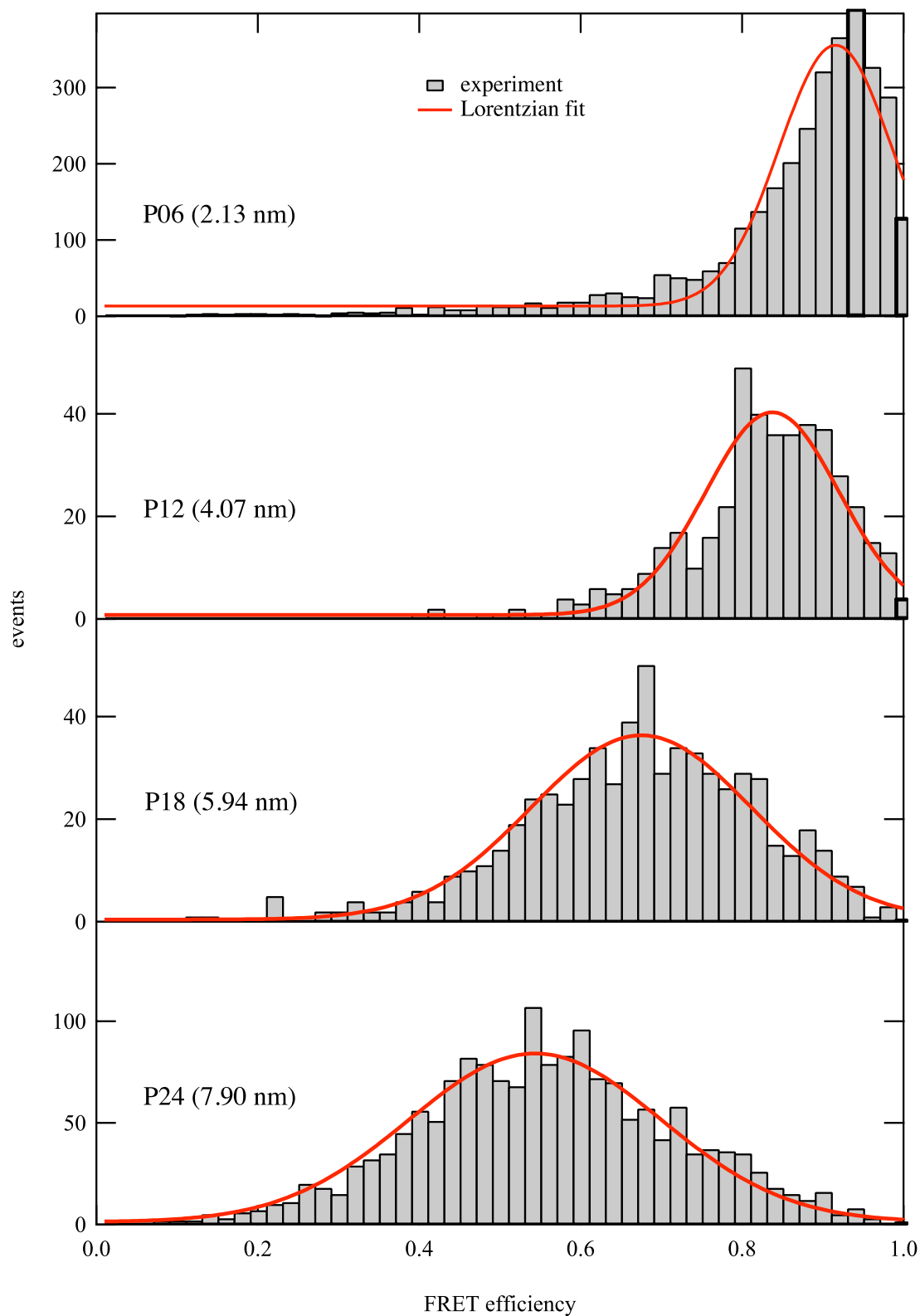


Fig. 4.12: PIE-filtered FRET histograms for different lengths of poly-L-proline labeled with Alexa-555 and Alexa-647 as donor and acceptor respectively. The zero efficiency peak visible in figure 4.11 is suppressed while otherwise the histograms are not changed.

is already in the order of the IRF of 0.3 ns (see section 2.5.2), shorter lifetimes expected for the FRET pairs can be deduced only with increasing uncertainties. For P12 fluorescence lifetimes below 0.1 ns are expected which can not be resolved properly, even after a deconvolution with the IRF. In consequence, the determination of the transfer efficiency from fluorescence lifetime measurements was only possible for the P24 and P18 pairs but not for P12 and P06. The donor fluorescence decay of the PIE-filtered intact P18 and P24 FRET pairs could be fitted with a mono exponential decay after deconvolution with the IRF, yielding lifetimes of (0.30 ± 0.02) ns and (0.35 ± 0.02) ns respectively. In contrast, a mono exponential fit was not able to reproduce the fluorescence decay for the unfiltered data. The corresponding transfer efficiencies (eq. 4.5) are (0.33 ± 0.08) for P18 and (0.24 ± 0.08) for the P24 FRET pair. The given uncertainties are connected with the fitting procedure of the fluorescence decay curves⁶.

From figure 4.12, the centers of the distributions were identified by Lorentzian fits and attributed to the average measured FRET efficiencies of the corresponding samples. These measured FRET efficiencies are plotted against the contour length of the poly-L-proline spacer in figure 4.13 along with the FRET efficiencies from the fluorescence lifetime analysis. The dashed curve in figure 4.13 represents the conventional Förster distance dependence (with $R_0 = 5.1$ nm):

$$E = \frac{1}{1 + (R/R_0)^6}. \quad (4.24)$$

The disagreement between theory and experimental values is obvious. While the theory has to be adjusted for the experimental conditions to include spectral crosstalk for the intensity based FRET analysis (see equation 4.14) this correction is not necessary for the lifetime based FRET analysis. Nevertheless the FRET values obtained from lifetime measurements are not reproduced very well by the simple distance dependence (4.24) (dashed curve in figure 4.13).

The two assumptions made for this model are that the dye separation is fixed and can be described by a linear function of the number of proline residues (eq. 4.1) and that the dipoles of the donor and acceptor are free to rotate in all directions on a timescale much faster than their fluorescence lifetime. If the first condition is not met, the actual mean dye separation is smaller than the contour length of the poly-L-proline spacer (see section 4.1.4). The second

⁶ The lifetime fitting procedure is described in section 2.5.4, page 36

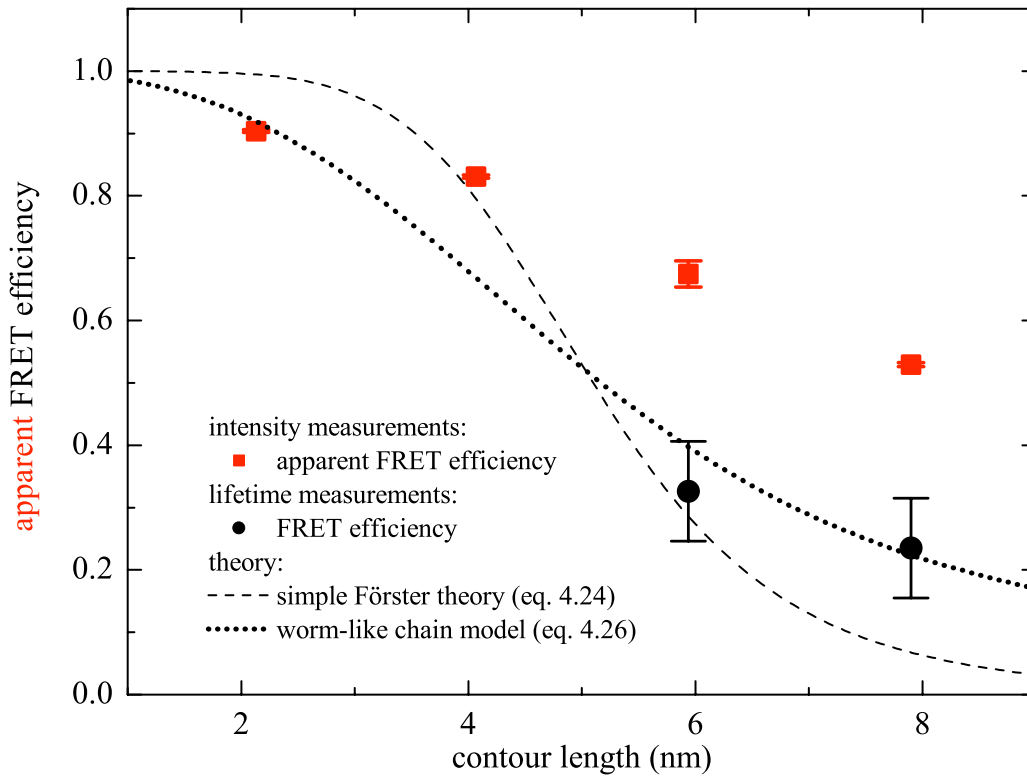


Fig. 4.13: Apparent FRET efficiencies from burst intensity analysis (red squares) and FRET efficiencies from fluorescence lifetime analysis (black circles). For comparison the expected distance dependence of the transfer efficiency for $R_0 = 5.1$ nm according to (4.24) (dashed curve) and the expected FRET efficiency according to the worm-like chain model (4.26) (dotted curve) are shown.

assumption has an explicit consequence for the Förster distance R_0 as it can not be calculated assuming $\kappa^2 = 2/3$, if the rotational freedom of the dyes is limited or a temporal averaging over all dipole orientations of the dye molecules can not be presumed because the fluorescence lifetime is in the same order of magnitude as the rotational decay time of the fluorophores.

Unfortunately both assumptions do not hold for the system under investigation and dynamical effects of the poly-L-proline spacer and the fluorophores must be considered as has been shown by Schuler et al. [116] recently. Simulations revealed that poly-L-proline does not behave like a rigid rod but more like a worm-like chain. According to Schuler the distance of the fluorophores follows a distribution with the contour length being the largest possible end-to-end distance (see section 4.1.4).

The important characteristic time scales are the donor fluorescence lifetime, the relaxation time of the distance fluctuations, the rotational anisotropy relaxation time of the donor fluorophore and the diffusion time.

The relaxation time of the distance fluctuations were found to increase from 0.2 ns (P10) to 2 ns (P25) and to 10 ns for P40 [116] compared to diffusion times of (0.255 ± 0.001) ms to (0.385 ± 0.001) ms. That means that the distance fluctuations are too fast to be resolved and only the average distance can be measured, underpinning the statement that the widths of the distance FRET efficiency distributions shown in the figures 4.11 and 4.12 are purely due to shot noise.

The energy transfer, on the other hand is faster than the distance fluctuations, at least for the larger poly-L-proline molecules. This means, that the average transfer efficiency has to be calculated by integrating the transfer efficiency $E(r)$ weighted by the end-to-end distance distribution $P(r)$ (eq. 4.2) over all possible end-to-end distances:

$$\langle E \rangle = \int_0^{l_c} E(r)P(r) dr . \quad (4.25)$$

l_c is the contour length of the poly-L-proline spacer (see equation 4.1). This equation only holds for cases where fast rotational averaging of the dipole orientation moments can be presumed. Anisotropy measurements done on Alexa-488 (coupled in the same way to P20 as Alexa-555 in this study) revealed an anisotropy relaxation time of 0.3 ns [116]. The fluorescence lifetime of the donor was found to be shorter than 0.35 ns (P24). Consequently the usual assumption of $\kappa^2 = 2/3$ is not valid anymore. Since I do not have anisotropy data for the system I assume the anisotropies to be similar as measured for Alexa-488 since the same linkers were used and the fluorophores are similar. Anisotropy should mainly depend on the rotational mobility of the fluorophores which is determined by the linker. Assuming that the fluorescence lifetime of the donor is much smaller than the anisotropy decay time (which holds at least for the small poly-L-proline molecules) the transition dipole orientations are randomly oriented but static during the FRET process (see also section 1.2.1).

Therefore equation 4.25 is adjusted to take the dynamic behavior of the dipole orientations into account and I compare the results with the distance dependence of the transfer efficiency $\langle E \rangle$ for dyes with random but static relative transition dipole orientations using the isotropic

probability density $\rho(\kappa^2)$ (see section 1.2.1 or [50]) and a distance distribution $P(r)$ of a worm-like chain (eq. 4.2, section 4.1.4 or [125]).

$$\begin{aligned} \langle E \rangle &= \int_0^4 \int_a^{l_c} E(r, \kappa^2) P(r) \rho(\kappa^2) dr d\kappa^2 \\ \text{with} \\ E(r, \kappa^2) &= \left(1 + \frac{2}{3\kappa^2} \left(r/R_{\frac{2}{3}} \right)^6 \right)^{-1} \\ \text{and} \\ \rho(\kappa^2) &= \begin{cases} \frac{1}{2\sqrt{3}\kappa^2} \ln(2 + \sqrt{3}), & 0 \leq \kappa^2 \leq 1 \\ \frac{1}{2\sqrt{3}\kappa^2} \ln\left(\frac{2+\sqrt{3}}{\sqrt{\kappa^2+\sqrt{\kappa^2-1}}}\right), & 1 \leq \kappa^2 \leq 4 \end{cases}. \end{aligned} \quad (4.26)$$

This equation holds for cases where the rotational relaxation and the chain dynamics are slower than the fluorescence lifetime of the donor. Equation 4.26 is also depicted in figure 4.13 as a black dotted line. Considering the uncertainties of the lifetime FRET values for the longest poly-L-prolines the measured transfer efficiencies are reproduced quite well by the model.

Let us now focus on the intensity FRET measurements. As stated above the experimental conditions must be considered to account for spectral crosstalk. Intensity FRET measurements yield an apparent FRET efficiency which can be calculated using the following equation, developed in section 4.3.3:

$$\langle E_{app} \rangle = \frac{T^A [{}^D\beta_{532}^A(1 - \langle E \rangle) + {}^A\beta_{532}^A + {}^{DA}\beta_{532}^A \langle E \rangle]}{T^A [{}^D\beta_{532}^A(1 - \langle E \rangle) + {}^A\beta_{532}^A + {}^{DA}\beta_{532}^A \langle E \rangle] + T^D [{}^D\beta_{532}^D(1 - \langle E \rangle)]}. \quad (4.27)$$

The parameters needed for calculation of the apparent FRET efficiency for a particular donor-acceptor distance are the molecular brightness β of the donor and acceptor in both detection channels as well as the burst duration times which can be approximated by the diffusion time, since only their ratio (T^A/T^D) is important. The molecular brightness β have already been determined from donor-only and acceptor-only labeled samples in section 4.5.3 but can also be directly extracted from the donor-only fraction of the FRET samples since donor-only molecules can be identified by PIE. The molecular brightness of the acceptor fluorophore can be directly analyzed from acceptor-only but also from acceptor and donor bearing molecules after direct acceptor excitation. Table 4.6 shows the molecular brightness extracted compared

	singly labeled	PIE sorted
${}^D\beta_{532}^D$	38 ± 5	45 ± 12
${}^D\beta_{532}^A$	7.0 ± 1.5	16 ± 11
${}^A\beta_{532}^A$	4.2 ± 0.7	-
${}^A\beta_{638}^A$	71 ± 8	99 ± 28

Tab. 4.6: Molecular brightnesses (in kHz per molecule and mW) extracted by PIE sorting from FRET samples in comparison with molecular brightnesses found for the singly-labeled samples. Shown also are the average passage times T^A and T^D for acceptor and donor detection channel respectively.

to the respective molecular brightnesses from section 4.5.3. Since the samples now have much lower concentration than the singly-labeled molecules in section 4.5.3 the uncertainties of the obtained molecular brightnesses are higher. The molecular brightness of the acceptor fluorophore excited with 532 nm and detected in the acceptor detection channel ($Dir, {}^A\beta_{532}^A$), could not be determined from the PIE sorted data, since almost no acceptor-only molecules could be found in the samples. Although the molecular brightnesses measured on the singly labeled and the PIE sorted molecules are in accordance within the uncertainties the PIE sorted values are higher than the values obtained from the singly-labeled samples. This is attributed to the PIE sorting since due to the selection with a threshold criterion brighter molecules (or molecules that spend more time in the effective volume) are favored.

Figure 4.14 once more shows the intensity FRET measurements. The dashed curve again shows the simple $1/R^6$ distance dependence of the FRET efficiency along with the dependence of the energy transfer efficiency on the contour length supposing the worm-like chain model. Calculating the mean apparent FRET efficiency (4.27) for a worm like chain (equation 4.26), the resulting distance dependence reproduces the measured intensity FRET efficiencies very well (red curve, figure 4.14). The disagreement, still existent for P06, might be caused by the breakdown of the point-dipole approximation used in the Förster theory since the distance of the fluorophores in this case is in the same dimension as the size of the fluorophores.

If one would consider fast averaging of the dipole orientations ($\kappa = 2/3$) instead of static but random dipole orientations the apparent FRET efficiency is higher than the measured intensity FRET values, especially for the shorter poly-L-prolines (red dashed curve in figure 4.14). This supports that fast rotational averaging is not taking place and the approximation of $\kappa = 2/3$ is not valid for our FRET pair.

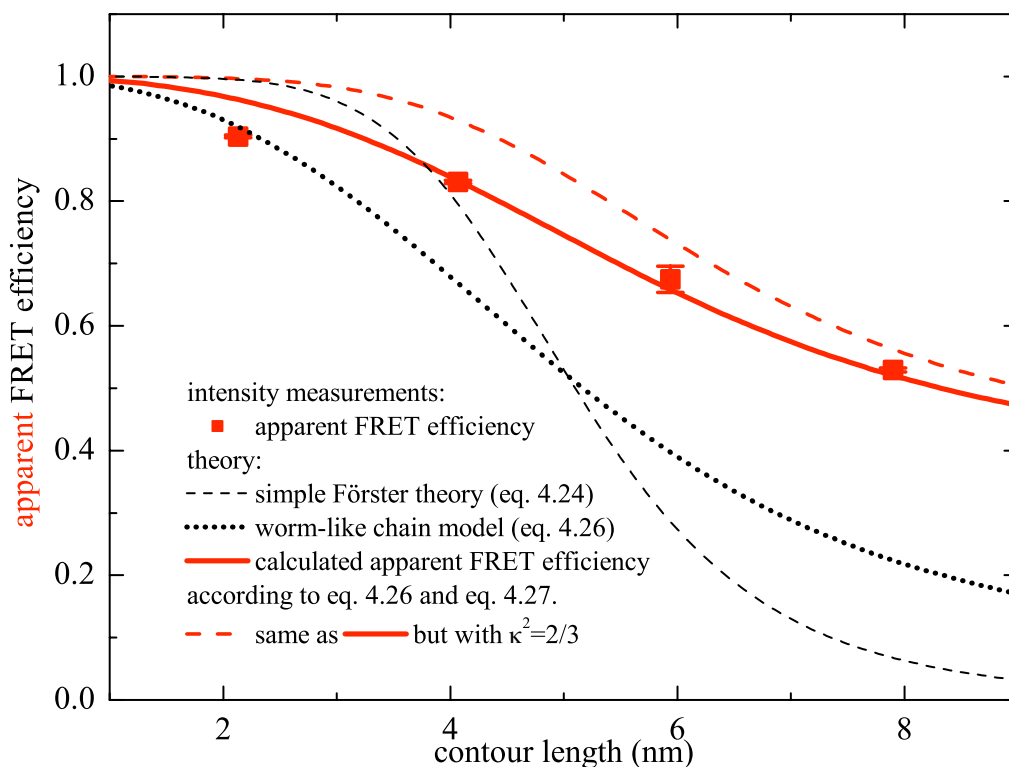


Fig. 4.14: Apparent FRET efficiencies from intensity FRET analysis and the calculated apparent FRET efficiencies for the worm-like chain model assuming random but static dipole orientations (straight red curve). For comparison the calculated apparent FRET efficiency assuming $\kappa^2 = 2/3$ (red dashed curve), the expected dependence of the transfer efficiency for $R_0 = 5.1$ nm (black dashed curve) and the expected FRET efficiency for poly-L-proline according to the worm-like chain model without considering spectral crosstalk etc. (black dotted curve) are shown as well.

4.6 Trans-Location-Motif (TLM)

To test the PIE-FRET measuring and analysis technique on a biological relevant molecule, the FRET efficiency of the TransLocation Motif (TLM) was measured. Figure 4.16 shows the FRET histogram from which the center of the transfer efficiency distribution was derived by fitting the histogram with a Lorentzian function. The measured apparent FRET efficiency of the TLM was found to be 0.84 ± 0.01 . With the knowledge of the molecular brightness of the two fluorophores in its respective detection channels, equation 4.14 can be used to extract

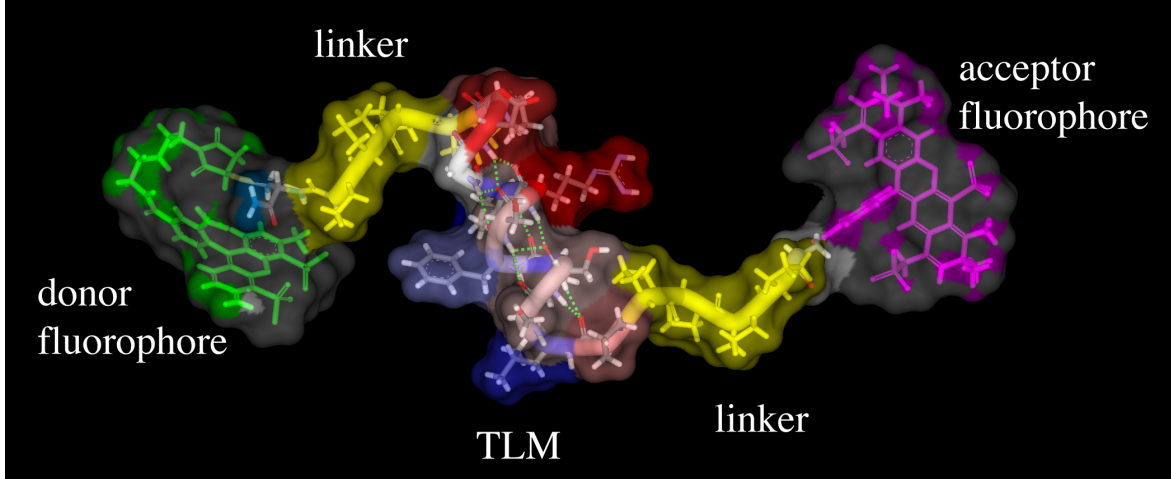


Fig. 4.15: Molecular structure of the TLM molecule. Shown is the TLM molecule with donor and acceptor fluorophore coupled through P04 (poly-L-proline) linkers. Since the structure of the used Alexa-555 and Alexa-647 is kept secret, for visualisation here Alexa-488 and Alexa-594 are shown instead. The end-to-end distance of this α -helical conformation has been determined by molecular modeling with AMBER97 to be 3.8 nm, already including the linker molecules.

the mean FRET efficiency from intensity FRET measurements:

$$\langle E \rangle = \frac{A\beta_{532}^A T^A (\langle E_{app} \rangle - 1) + D\beta_{532}^A T^A (\langle E_{app} \rangle - 1) + D\beta_{532}^D T^D \langle E_{app} \rangle}{D\beta_{532}^A T^A (\langle E_{app} \rangle - 1) + DA\beta_{532}^A T^A (1 - \langle E_{app} \rangle) + D\beta_{532}^D T^D \langle E_{app} \rangle}. \quad (4.28)$$

With this equation the corrected energy transfer efficiency can be calculated from the apparent FRET efficiency. To calculate the contour length, a model for the TLM molecule needs to be applied. Since the same fluorophores, coupled the same way, as for the poly-L-proline assay were used, the dynamics of the fluorophores are expected to be identical (fluorescence lifetime has been measured and found to be identical for both fluorophores as compared to donor and acceptor coupled to the poly-L-prolines). Whether the TLM molecule itself undergoes bending or other dynamics is unknown, therefore only the end-to-end distance can be calculated. This parameter, however is the parameter of interest, since information about the molecular structure and its actual conformation can be extracted.

To obtain the end-to-end distance, the following equation needs to be solved numerically:

$$\int_0^4 \left(1 + \frac{2}{3\kappa^2} \left(r/R_{\frac{2}{3}} \right)^6 \right)^{-1} \rho(\kappa^2) d\kappa^2 = \frac{A\beta_{532}^A T^A (\langle E_{app} \rangle - 1) + D\beta_{532}^A T^A (\langle E_{app} \rangle - 1) + D\beta_{532}^D T^D \langle E_{app} \rangle}{D\beta_{532}^A T^A (\langle E_{app} \rangle - 1) + DA\beta_{532}^A T^A (1 - \langle E_{app} \rangle) + D\beta_{532}^D T^D \langle E_{app} \rangle}, \quad (4.29)$$

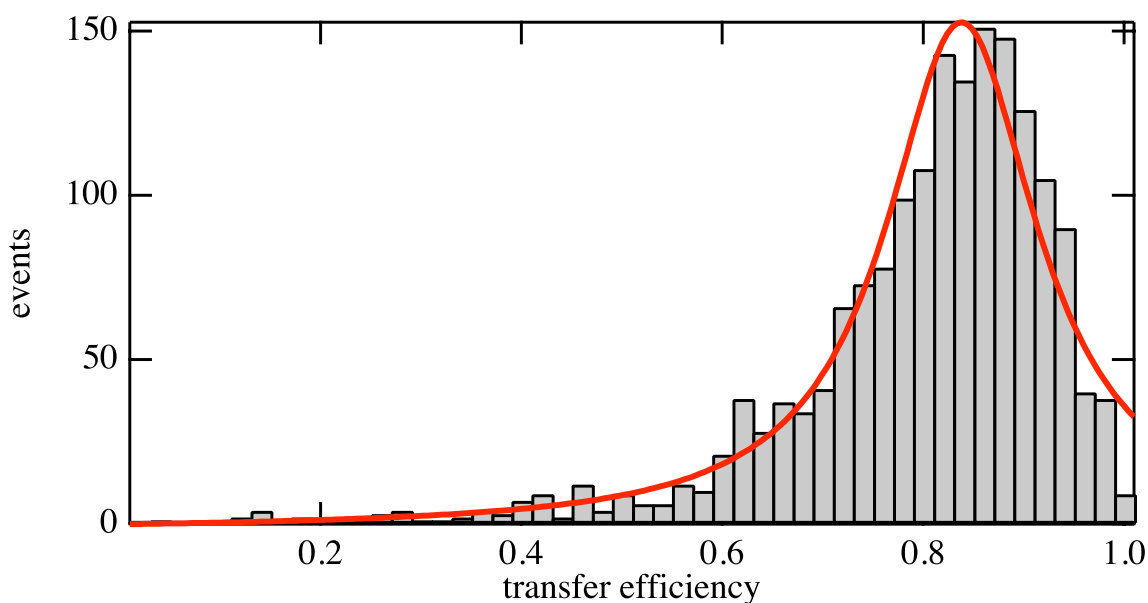


Fig. 4.16: PIE-filtered FRET histogram for TLM labeled with Alexa-555 and Alexa-647 as donor and acceptor respectively.

with $\rho(\kappa^2)$ as defined in equation 4.26 and $R_{2/3} = 5.1 \text{ nm}$. The apparent FRET efficiency of 0.84 ± 0.1 as extracted from figure 4.16 translates into an end-to-end distance of $(3.7 \pm 0.5) \text{ nm}$. Figure 4.15 shows the molecular structure of the TLM molecule in the α -helix conformation. For this conformation the molecular modeling calculations done by my collaborators at the Robert Koch Institute predict an end-to-end distance of 3.8 nm as opposed to 6.1 nm for the β -strand conformation. From the histogram in figure 4.16 it becomes obvious that the TLM is exclusively in the α -helix conformation, which is expected from molecular energy simulations of the TLM peptide in water.

4.7 Concluding Remarks

Quantitative distance measurements are difficult to obtain in spite of the strong distance dependency of the energy transfer efficiency. One problem for the interpretation of the FRET efficiency is the so-called zero efficiency peak caused by FRET pairs with missing or non-fluorescent acceptors. Other problems occurring are direct excitation of the acceptor, spectral crosstalk and the determination of the quantum efficiency of the dyes as well as the different detector sensitivities.

The presented approach to overcome these limitation uses Pulsed Interleaved Excitation

(PIE) to separately excite donor and acceptor fluorophores. Time Correlated Single Photon Counting (TCSPC) makes it possible to probe the presence and function of donor and acceptor independently through time gating of the detected fluorescence photons. With the method described, molecules with absent or non fluorescing acceptor are identified and excluded from FRET analysis. The zero efficiency peak, present in most intensity FRET histograms disappears if only molecules bearing intact donor and acceptor fluorophores are considered for analysis. This implicitly proves that the zero efficiency peak originates from FRET pairs with absent or non fluorescent acceptor chromophores.

Lifetime measurements also gain advantage from PIE because with PIE the fluorescence lifetime of intact and broken FRET pairs can be analyzed independently.

By combining FCS with PIE-FRET quantitative FRET results were obtained even in the presence of strong spectral crosstalk. I have shown that systematic errors introduced by spectral crosstalk, direct acceptor excitation and different detection- and quantum-efficiencies for the donor and acceptor fluorophores can be determined by this combination. It is not necessary to measure or calculate transmission and detection efficiencies of the experimental setup, as all sample and setup parameters needed are obtained by FCS analysis of the same experimental data set or analyzing probes containing single labeled FRET molecules.

The measured donor-acceptor separations are in accordance with the contour lengths of the poly-L-proline spacers determined by molecular modeling considering the worm-like chain model for poly-L-proline peptides as proposed by Schuler et al. [116].

It was shown that accurate single pair FRET distance measurements with uncertainties of about 0.5 nm to 1 nm are reasonable. The accuracy depends on the actual distance. Distances close to the Förster radius R_0 can be measured more accurate due to the shape of the distance dependence function.

The developed method was used to measure the end-to-end distance of the TLM molecule, a peptide playing an integral role for the cell permeability of the HBV virus. The end-to-end distance found was (3.7 ± 0.5) nm, which corresponds to the α -helical conformation of the the TLM molecule. Because the measurements were done in the single molecule regime it could be ascertained that the TLM molecule was exclusively in this conformation.

5. SUMMARY

The scope of this work was to evaluate the accuracy and the limits of quantitative Fluorescence Correlation Spectroscopy (FCS) and Förster Resonance Energy Transfer (FRET) on a single molecule level. In particular the accuracy of FCS for the determination of picomolar concentrations of fluorophores and their diffusion coefficients in solution as well as the accuracy of single molecule distance measurements on the nm-scale with FRET was investigated.

First, three different methods to determine the confocal volume of a confocal microscope are compared as knowledge of the confocal volume is mandatory for concentration measurements as well as measurements of the diffusion coefficient employing FCS. In fact, the accuracy in determining concentrations and diffusion coefficients is mainly given by the uncertainty of the confocal volume. i) The confocal volume was directly visualized by imaging a sub-resolution sized fluorescent microsphere, which offers the advantage that not only the confocal volume itself but also its shape can be evaluated. ii) The confocal volume was further extracted by fitting the correlation curve of a dye with a known diffusion coefficient. iii) The confocal volume was also determined from FCS measurements of a dilution series with known concentration. With this method, the confocal volume can be extracted without knowledge of the diffusion coefficient and without an assumptions for the shape of the confocal volume.

Considering the uncertainties of each of these methods which were found to be 10% at typically $V_{eff} = 1.0 \text{ fl}$, the confocal volumes determined with all three methods were inaccordance.

The imaging of fluorescent microspheres is a mandatory technique for the adjustment of the confocal setup. It serves to discover and minimize artifacts caused by cover slide thickness deviation, refractive index mismatch etc. Obtaining the confocal volume from fitting the correlation curve of a dye with a known diffusion coefficient is a straightforward and fast calibration method, however, since the photophysics of the dye influence the Molecule Detection Function (MDF) and therefore the confocal volume, those effects need to be considered,

especially if different fluorophores are used for the calibration and in the experiment. Furthermore, since this method depends on a model assumption, it can only be as accurate as the model describes the system. Determining the confocal volume through a dilution series offers the possibility to measure the confocal volume under the same experimental conditions that apply in the experiment but is considered more elaborate. The accuracy depends on the accuracy of the sample preparation. Different experimental conditions and their influence on the MDF were analyzed; e.g. laser power and cover-slide thickness mismatch were found not only to change the size but also the shape of the confocal volume. Although the commonly used 3D Gaussian approximation of the confocal volume seems sufficient for most FCS experiments, deviations from the assumed shape became apparent when the experimental setup was only slightly misaligned. The influence of laser excitation power, cover-slide thickness mismatch as well as different excitation and detection configurations on the count rate per molecule and the confocal volume were discussed.

In the second part FRET measurements with Pulsed Interleaved Excitation (PIE) and time correlated single photon counting are presented. With PIE both fluorophores, donor and acceptor molecules, are excited separately. Time gating enables to probe the presence of donor and acceptor molecules independently. With the method described, molecules with absent or non fluorescing acceptor are identified and excluded from FRET analysis. It was shown that the zero efficiency peak present in most intensity FRET histograms disappears if only molecules bearing intact donor and acceptor fluorophores are considered for intensity FRET analysis. This implicitly proves that the zero efficiency peak originates from FRET pairs with absent or non fluorescent acceptor chromophores.

Lifetime measurements also gain advantage from PIE because with PIE the fluorescence lifetime of intact and broken FRET pairs can be analyzed independently.

Furthermore, combining FCS with PIE-FRET enables to obtain quantitative FRET results even in the presence of strong spectral crosstalk. It was shown that systematic errors introduced by leakage, direct acceptor excitation and different detection- and quantum-efficiencies for the donor and acceptor fluorophores can be determined by this combination. It is not necessary to measure or calculate transmission and detection efficiencies of the experimental setup, as all sample and setup parameters needed are obtained by FCS analysis of the same experimental data set or analyzing probes containing single labeled FRET molecules.

The measured donor-acceptor separations are in accordance with the contour lengths of the polyproline spacers determined by molecular modeling considering the worm-like chain model for polyproline peptides as proposed by Schuler et al. [116].

With the improvements presented, accurate single pair FRET distance measurements with uncertainties of 0.5 nm for distances close to the Förster radius and about 1 nm otherwise are reasonable, pushing single pair FRET from a qualitative method one step further towards a quantitative distance measuring technique.

With the developed method not only the conformation but also the length of the TransLocation Motif (TLM), a peptide important for the cell permeability of the HBV virus, could be determined. The end-to-end distance of the investigated TLM molecules was found to be (3.7 ± 0.5) nm which corresponds to the α -helical conformation of the molecule.

ACRONYMS

AFM Atomic Force Microscopy

AFM is a very high-resolution type of scanning probe microscope. AFM employs a cantilever tip which measures forces between the sample and the tip. Depending on the situation, forces that are measured in AFM include mechanical contact force, Van der Waals forces, capillary forces, chemical bonding, electrostatic forces, magnetic forces, Casimir forces, solvation forces etc.

ALEX Alternating Laser Excitation

The term ALEX has originally been introduced for the independent excitation of two fluorophores by two lasers, interleaved on the microsecond time scale. At present it is also used for Pulsed Interleaved Excitation (PIE) by some groups.

AMBER Assisted Model Building and Energy Refinement

AMBER is a family of force fields for molecular dynamics of biomolecules originally developed by the late Peter Kollman's group at the University of California, San Francisco. AMBER is also the name for the molecular dynamics simulation package that implements these force fields.

APD Avalanche Photo Diode

APDs are photodetectors that can be regarded as the semiconductor analog to photomultipliers. By applying a high reverse bias voltage (typically 100-200 V in silicon), APDs show an internal current gain effect (around 100) due to impact ionization (avalanche effect).

ASCII American Standard Code for Information Interchange

ASCII is a character encoding based on the English alphabet. ASCII codes represent text in computers

BIFL Burst Integrated Fluorescence Lifetime

- CEF** Collection Efficiency Function
the CEF is explained in detail in section 2.4.3
- cw** Continuous Wave
In laser physics the term "continuous wave" or "CW" refers to a laser which produces a continuous output beam.
- EID** Excitation Intensity Distribution
the EID is explained in detail in section 2.4.1
- EPD** Excitation Propability Distribution
the EPD is explained in detail in section 2.4.2
- FCS** Fluorescence Correlation Spectroscopy
Analysis of fluorescence intensity fluctuations (e.g. due to brownian motion)
- FIDA** Fluorescence Intensity Distribution Analysis
- FRET** Förster Resonance Energy Transfer
Radiationless transmission of an energy quantum from an excited donor fluorophore to an acceptor by resonance interaction
- FWHM** Full Width Half Maximum
FWHM is the extent of a function, given by the difference between the two extreme values of the independent variable at which the dependent variable is equal to half of its maximum value.
- HPLC** High Performance Liquid Chromatography
HPLC is a form of column chromatography. HPLC is used to separate components of a mixture based on a variety of chemical interactions between the substance being analyzed (analyte) and the chromatography column.
- IC** Internal Conversion
IC is a transition between one set of electronic excited levels to another set of the same spin multiplicity (for example, the second singlet state to the first singlet state). It is sometimes called "radiationless de-excitation", because no photons are emitted.
- IRF** Instrument Response Function

ISC	InterSystem Crossing ISC is a transition between two electronic states having different spin multiplicities. Usually referred to as the relaxation of an excited singlet state to an excited triplet state.
MDF	Molecule Detection Function the MDF is explained in detail in section 2.4.4
MFD	Multi Parameter Fluorescence Detection
MS	Mass Spectroscopy MS is used to measure the mass-to-charge ratio of ions.
NA	Numerical Aperture NA is a dimensionless number that characterizes the range of angles over which a system can accept or emit light.
NMR	Nuclear Magnetic Resonance
OD	Optical Density The optical density is the absorbance of an optical element.
PBS	Phosphate Buffered Saline PBS is a buffer solution commonly used in biochemistry to maintain a constant pH. It is a salty solution containing sodium chloride, sodium phosphate and potassium phosphate in concentrations that match the human body.
PBST	Phosphate Buffered Saline, additionally containing the detergent Tween 20 Tween 20 is added to PBS in order to prevent sample agglomeration and surface adsorption.
PCA	Photon Counting Analysis see Photon Counting Histogram (PCH)
PCH	Photon Counting Histogram
PCR	Polymerase Chain Reaction PCR is a molecular biology technique for enzymatically replicating DNA without using a living organism. PCR allows a small amount of the DNA molecule to be amplified exponentially.

PIE-FRET Pulsed Interleaved Excitation FRET

PIE Pulsed Interleaved Excitation

Two picosecond laser pulses at different wavelengths are interleaved to excite alternately two different fluorophores.

PMT Photo Multiplier Tube

PMTs are sensitive detectors of light. PMTs multiply the signal produced by incident light by as much as 10^8 , from which single photons can be resolved.

S/B Signal to Background ratio

The signal to background ratio is different from the Signal to Noise ratio (S/N) as it the background can be considered as a quantifiable bias to the signal. S/B reduces the signal contrast

S/N Signal to Noise ratio

S/N is a term for the ratio between a signal (meaningful information) and the uncorrelated noise of a measurand due to detector noise etc.

SPAD Single Photon counting Avalanche Diode module

SPADs are APDs specifically designed for single photon counting. The APD is operated at voltage biases above the breakdown voltage (in the so-called Geiger mode) so that a single photon incident on the detector will give rise to a macroscopic current pulse. SPADs are APDs combined with appropriate pulse detection circuitry which transforms a single detected photons into a electrical (usually TTL) pulse.

spFRET single pair FRET

FRET on single molecules

STM Scanning Tunneling Microscopy

STM scans an electrical probe (tip) over a surface to be imaged to detect a weak electric current flowing between the tip and the surface. The tip and the surface are not brought into contact, electrons tunnel through the insulator gap between tip and surface.

TCSPC Time Correlated Single Photon Counting

TCSPC records the arrival time of a photon at an appropriate single photon detector (e.g. SPAD or PMT) with respect to a preceding laser pulse or previously detected photon. Timing accuracy is in the order of picoseconds, enabling fluorescence lifetime or antibunching analysis

TLM TransLocation Motif

Tween 20 Tween 20

A polysorbate used as a detergent

t3r Time Tagged Time Resolved

file format in which the temporal information of all detected photons is stored along with routing and spatial informations.

BIBLIOGRAPHY

- [1] Wikipedia, The Free Encyclopedia, “Ergodic Hypothesis.” <http://en.wikipedia.org/w/index.php?oldid=59163871>, accessed 16-August-2006.
- [2] E. Schrödinger, *What is Life?* Cambridge University Press, Cambridge, 1944.
- [3] B. Krämer, S. Rüttinger, J. Neukammer, R. Macdonald, H. Rinneberg, M. Roos, K. Büchner, and R. Kroczeck, “Single Molecule Detection in Tissue Sections of Human Lymph Nodes by Confocal Microscopy,” Talk given at the 9th PicoQuant Workshop on Single Molecule Detection and Ultrasensitive Analysis in the Life Sciences, Berlin, 2003.
- [4] T. Kohl, K. G. Heinze, R. Kuhlemann, A. Koltermann, and P. Schwille, “A Protease assay for two-photon crosscorrelation and FRET analysis based solely on fluorescent proteins,” *Proc. Natl. Acad. Sci. USA*, vol. 99, pp. 12161–12166, 09 2002.
- [5] D. Magde, E. L. Elson, and W. W. Webb, “Thermodynamic Fluctuations in a Reacting System—Measurement by Fluorescence Correlation Spectroscopy,” *Phys. Rev. Lett.*, vol. 29, no. 11, pp. 705–708, 1972.
- [6] E. L. Elson, D. M. Elson, and D. Magde, “Fluorescence Correlation Spectroscopy: I. Conceptual Basis and Theory,” *Biopolymers*, vol. 13, pp. 1–27, 1974.
- [7] D. Magde, E. L. Elson, and W. W. Webb, “Fluorescence correlation spectroscopy: II. an experimental realization,” *Biopolymers*, vol. 13, pp. 29–61, 1974.
- [8] R. Rigler, Ü. Mets, J. Widengren, and P. Kask, “Fluorescence correlation spectroscopy with high count rate and low background: analysis of translational diffusion,” *European Biophysical Journal*, vol. 22, no. 3, pp. 169–175, 1993.

- [9] M. Eigen and R. Rigler, "Sorting single molecules: Application to diagnostics and evolutionary biotechnology," *Proc. Natl. Acad. Sci. USA*, vol. 21, pp. 5740–5747, 06 1994.
- [10] T. Ha, A. Ting, J. Liang, A. Deniz, D. Chemla, P. Schultz, and S. Weiss, "Temporal fluctuations of fluorescence resonance energy transfer between two dyes conjugated to a single protein," *Chem. Phys.*, vol. 247, pp. 107–118, 1999.
- [11] A. A. Deniz, M. Dahan, J. R. Grunwell, T. Ha, A. E. Faulhaber, D. S. Chemla, S. Weiss, and P. G. Schultz, "Single-pair fluorescence resonance energy transfer on freely diffusing molecules: Observation of Förster distance dependence and subpopulations," *Proc. Natl. Acad. Sci. USA*, vol. 96, pp. 3670–3675, 1999.
- [12] A. Deniz, T. Laurence, G. Beligere, M. Dahan, A. Martin, D. Chemla, P. Dawson, P. Schultz, S. W. Laurence, M. Dahan, D. Chemla, P. Schultz, and S. Weiss, "Ratiometric single-molecule studies of freely diffusing biomolecules," *Ann. Rev. Phys. Chem.*, vol. 52, pp. 233–253, 2001.
- [13] S. Nie and R. Zare, "Optical detection of single molecules," *Annu. Rev. Biophys. Biomol. Struct.*, vol. 26, pp. 567–596, 1997.
- [14] X. Xie and J. Trautmann, "Optical studies of single molecules at room temperature," *Ann. Rev. Phys. Chem.*, vol. 49, pp. 441–480, 1998.
- [15] T. Basché, S. Nie, and J. M. Fernandez, "Single molecules," *Proc. Natl. Acad. Sci. USA*, vol. 98, no. 19, pp. 10527–10528, 2001.
- [16] S. R. Aragon and R. Pecora, "Fluorescence correlation spectroscopy as a probe of molecular dynamics," *J. Chem. Phys.*, vol. 64, no. 4, pp. 1791–1803, 1976.
- [17] A. G. Palmer, 3rd and N. L. Thompson, "Molecular aggregation characterized by high order autocorrelation in fluorescence correlation spectroscopy," *Biophys. J.*, vol. 52, no. 2, pp. 257–270, 1987.
- [18] M. Kinjo and R. Rigler, "Ultrasensitive hybridization analysis using fluorescence correlation spectroscopy," *Nucleic Acids Res.*, vol. 23, no. 10, pp. 1795–1799, 1995.

- [19] P. Schwille, J. Bieschke, and F. Oehlenschläger, “Kinetic investigations by fluorescence correlation spectroscopy: the analytical and diagnostic potential of diffusion studies,” *Biophys. Chem.*, vol. 66, pp. 211–228, 1997.
- [20] J. Widengren, Ü. Mets, and R. Rigler, “Fluorescence Correlation Spectroscopy of Triplet States in Solution: A Theoretical and Experimental Study,” *J. Phys. Chem.*, vol. 99, pp. 13368–13379, June 1995.
- [21] P. Schwille, F. Meyer-Almes, and R. Rigler, “Dual-color fluorescence cross-correlation spectroscopy for multicomponent diffusional analysis in solution,” *Biophys. J.*, vol. 72, no. 4, pp. 1878–1886, 1997.
- [22] S. Maiti, U. Haupts, and W. W. Webb, “Fluorescence correlation spectroscopy: Diagnostics for sparse molecules,” *Proc. Natl. Acad. Sci. USA*, vol. 94, pp. 11753–11757, 1997.
- [23] R. Brown, J. Gallop, and M. Milton, “Review of techniques for single molecule detection in biological applications,” tech. rep., NPL National Physical Laboratory, 2001.
- [24] L. Stryer and R. P. Haugland, “Energy transfer: A spectroscopic ruler,” *Proc. Natl. Acad. Sci. USA*, vol. 58, pp. 719–726, 05 1967.
- [25] M. A. van Zandvoort, C. J. de Grauw, H. C. Gerritsen, J. L. Broers, M. G. oude Egbrink, F. C. Ramaekers, and D. W. Slaaf, “Discrimination of DNA and RNA in Cells by a Vital Fluorescent Probe: Lifetime Imaging of SYTO13 in Healthy and Apoptotic Cells,” *Cytometry*, vol. 47, pp. 226–235, 2002.
- [26] E. Galperin and A. Sorkin, “Visualization of Rab5 activity in living cells by FRET microscopy and influence of plasma-membrane-targeted Rab5 on clathrin-dependent endocytosis,” *Journal of Cell Science*, vol. 116, pp. 4799–4810, 2003.
- [27] L. Achnine, E. B. Blancaflor, S. Rasmussen, and R. A. Dixon, “Colocalization of L-Phenylalanine Ammonia-Lyase and Cinnamate 4-Hydroxylase for Metabolic Channeling in Phenylpropanoid Biosynthesis,” *The Plant Cell*, vol. 18, pp. 3099–3109, 2004.

- [28] R. B. Sekar and A. Periasamy, "Fluorescence resonance energy transfer (FRET) microscopy imaging of live cell protein localizations," *Journal of Cell Biology*, vol. 160, no. 5, pp. 629–633, 2005.
- [29] T. Ha, X. Zhuang, H. D. Kim, J. W. Orr, J. R. Williamson, and S. Chu, "Ligand-induced conformational changes observed in single RNA molecules," *Proc. Natl. Acad. Sci. USA*, vol. 96, pp. 9077–9082, August 1999.
- [30] T. Heyduk, "Measuring protein conformational changes by FRET/LRET," *Curr. Opin. Biotechnol.*, vol. 13, no. 4, pp. 292–296, 2002.
- [31] N. G. Walter, D. A. Harris, M. J. B. Pereira, and D. Rueda, "In the Fluorescent Spotlight: Global and Local Conformational Changes of Small Catalytic RNAs," *Biopolymers*, vol. 61, pp. 224–241, 2002.
- [32] M. Ottolia, K. D. Philipson, and S. John, "Conformational changes of the Ca(2+) regulatory site of the Na(+)-Ca(2+) exchanger detected by FRET," *Biophys. J.*, vol. 87, pp. 899–906, August 2004.
- [33] L. Zheng, K. P. Hoefflich, L. M. Elsby, M. Ghosh, S. G. E. Roberts, and M. Ikura, "FRET evidence for a conformational change in TFIIB upon TBP-DNA binding," *Eur. J. Biochem.*, vol. 271, pp. 792–800, 2004.
- [34] E. Hildt, B. Munz, G. Saher, K. Reifenberg, and P. H. Hofschneider, "The PreS2 activator MHBst of the Hepatitis B virus activates c-raf-1/ERK2- signaling in transgenic mice," *EMBO J.*, vol. 21, no. 4, pp. 525–535, 2002.
- [35] S. Oess and E. Hildt, "Identification of a novel cell permeable peptide derived from the Hepatitis B virus surface antigen," *Gene Ther.*, vol. 7, pp. 750–758, 2000.
- [36] G. Saher and E. Hildt, "Activation of c-raf-1 kinase signal transduction pathway in alpha(7) integrin-deficient mice," *J. Biol. Chem.*, vol. 274, pp. 27651–27657, 1999.
- [37] B. Brandenburg, *Cell Permeable Nucleocapsids as a novel Tool for Efficient Gene Transfer and HBV Biology*. PhD thesis, FU Berlin, 06 2005.
- [38] *Historia Plantarum Novae Hispania, 16 volumes (lost)*. F. Hernández.

- [39] *Codice Florentino*. B. Sahagun, ca.1548-1565.
- [40] A. U. Acuña and F. Amat-Guerri, "On the Origins of Molecular Luminescence: The Strange Colours of Lignum Nephriticum," Talk given at the 9th International Conference on Methods and Applications of Fluorescence, 2005.
- [41] T. Förster, *Fluoreszenz organischer Verbindungen*. Vandenhoeck und Ruprecht, Göttingen, 1951.
- [42] T. Förster, "Zwischenmolekulare Energiewanderung und Fluoreszenz," *Annalen der Physik*, vol. 2, no. 6, pp. 55–74, 1948.
- [43] T. Förster, *Modern Quantum Chemistry, Istanbul Lectures*, ch. III: Action of Light and Organic Crystals, pp. 93–137. Academic Press, New York, 1965.
- [44] I. Berlman, *Energy Transfer Parameters of Aromatic Compounds*. Academic Press New York, 1971.
- [45] N. N. Quant and A. V. Guzzo, "Energy-transfer studies using doublet-state acceptors," *J. Phys. Chem.*, vol. 85, no. 2, pp. 140–144, 1981.
- [46] T. Förster, "Experimentelle und theoretische Untersuchung des zwischenmolekularen Übergangs von Elektronenanregungsenergie," *Zeitschrift für Naturforscher*, vol. 4a, no. 5, pp. 321–327, 1949.
- [47] T. Förster, "10th Spiers Memorial Lecture. Transfer mechanisms of electronic excitation," *Discussions of the Faraday Society*, vol. 27, no. 7, pp. 7–17, 1959.
- [48] Invitrogen Website, Molecular Probes, "Spectral Data Alexa Fluor 555." <http://probes.invitrogen.com/media/spectra/data/21687h2o.txt>, accessed 16-August-2006.
- [49] Invitrogen Website, Molecular Probes, "Spectral Data Alexa Fluor 647." <http://probes.invitrogen.com/media/spectra/data/21686h2o.txt>, accessed 16-August-2006.
- [50] R. E. Dale, J. Eisinger, and W. E. Blumberg, "The orientational freedom of molecular probes," *Biophys. J.*, vol. 26, pp. 161–194, 05 1979.

- [51] E. Haas, E. Katchalskikatzir, and I. Z. Steinberg, "Effect of the orientation of donor and acceptor on the probability of energy transfer involving electronic transitions of mixed polarization," *Biopolymers*, vol. 17, pp. 5064–5070, November 1978.
- [52] W. B. Van Der Meer, M. A. Raymer, S. L. Wagoner, R. L. Hackney, J. M. Beechem, and E. Gratton, "Designing matrix models for fluorescence energy transfer between moving donors and acceptors," *Biophys. J.*, vol. 64, no. 4, pp. 1243–1263, 1993.
- [53] H. Tompa and A. Englert, "The frequency distribution of the orientation factor of dipole-dipole interaction," *Biophys. Chem.*, vol. 9, pp. 211–214, November 1979.
- [54] W. B. Van der Meer, I. George Choker, and S.-Y. S. Chen, *Resonance Energy Transfer - Theory and Data*, ch. 4.2, pp. 60–66. VCH Publishers, Inc, 1994.
- [55] N. Wiener, "Extrapolation, interpolation and smoothing of stationary time series," *MIT Press*, 1949.
- [56] D. Koppel, "Statistical accuracy in fluorescence correlation spectroscopy," *Phys. Rev. A*, vol. 10, pp. 1938–1945, Dec 1974.
- [57] R. Rigler and J. Widengren, "Ultrasensitive detection of single molecules by fluorescence correlation spectroscopy," *Bioscience*, vol. 3, pp. 180–183, 1990.
- [58] R. Rigler, J. Widengren, and Ü. Mets, *Fluorescence Spectroscopy*, pp. 13–24. Springer Verlag Berlin, O.S. Wolfbeis ed., 1992.
- [59] Ü. Mets and R. Rigler, "Submillisecond detection of single rhodamine molecules in water," *J. Fluoresc.*, vol. 4, no. 3, pp. 259–264, 1994.
- [60] H. Qian and E. L. Elson, "Analysis of confocal laser-microscope optics for 3-D fluorescence correlation spectroscopy," *Appl. Opt.*, vol. 30, pp. 1185–1195, 1991.
- [61] D. R. Sandison and W. W. Webb, "Background rejection and signal-to-noise optimization in the confocal and alternative fluorescence microscopes," *Appl. Opt.*, vol. 33, pp. 603–615, 1994.
- [62] T. Dertinger, "Diffusion Coefficient of Atto 655." private communication, March 2006.

- [63] J. Enderlein, "Theoretical study of detection of a dipole emitter through an objective with high numerical aperture," *Opt. Lett.*, vol. 25, pp. 634–636, 2000.
- [64] J. Enderlein, I. Gregor, D. Patra, T. Dertinger, and U. B. Kaupp, "Performance of fluorescence correlation spectroscopy for measuring diffusion and concentration," *ChemPhysChem*, vol. 5, pp. 2324–2336, 2005.
- [65] J. Enderlein and C. Zander, *Theoretical Foundations of Single Molecule Detection in Solution*, ch. 2, pp. 35–48. Wiley-VCH, 1 ed., 2002.
- [66] D. V. O'Connor and D. Phillips, *Time-correlated Single Photon Counting*. Academic Press New York, 1984.
- [67] U. P. Wild, A. R. Holzwarth, and H. P. Good, "Measurement and analysis of fluorescence decay curves," *Rev. Sci. Instrum.*, vol. 48, pp. 1621–1627, 1977.
- [68] M. Wahl, I. Gregor, M. Patting, and J. Enderlein, "Fast calculation of fluorescence correlation data with asynchronous time-correlated single-photon counting," *Optics Express*, vol. 11, no. 26, pp. 3583–3591, 2003.
- [69] V. Buschmann, K. Weston, and M. Sauer, "Spectroscopic study and evaluation of red-absorbing fluorescent dyes," *Bioconjug. Chem.*, vol. 14, no. 1, pp. 195–204, 2003.
- [70] S. A. Soper, J. Benjamin L. Legendre, and J. Huang, "Evaluation of thermodynamic and photophysical properties of tricyanocyanine near-IR dyes in organized media using single-molecule monitoring," *Chem. Phys. Lett.*, vol. 237, no. 3-4, pp. 339–345, 1995.
- [71] C. Eggeling, J. R. Fries, L. Brand, R. Günther, and C. A. M. Seidel, "Monitoring conformational dynamics of a single molecule by selective fluorescence spectroscopy," *Proc. Natl. Acad. Sci. USA*, vol. 95, no. 4, pp. 1556–1561, 1998.
- [72] U. Haupts, S. Maiti, P. Schwille, and W. W. Webb, "Dynamics of fluorescence fluctuations in green fluorescent protein observed by fluorescence correlation spectroscopy," *Proc. Natl. Acad. Sci. USA*, vol. 95, pp. 13573–13578, 11 1998.
- [73] D. C. Daniel, M. Thompson, and N. W. Woodbury, "Fluorescence Intensity Fluctuations of Individual Labeled DNA Fragments and a DNA Binding Protein in Solution

- at the Single Molecule Level: A Comparison of Photobleaching, Diffusion, and Binding Dynamics,” *J. Phys. Chem. B*, vol. 104, no. 6, pp. 1382–1390, 2000.
- [74] L. Edman, Ü. Mets, and R. Rigler, “Conformational transitions monitored for single molecules in solution,” *Proc. Natl. Acad. Sci. USA*, vol. 93, no. 13, pp. 6710–6715, 1996.
- [75] S. Wennmalm, L. Edman, and R. Rigler, “Conformational fluctuations in single DNA molecules,” *Proc. Natl. Acad. Sci. USA*, vol. 94, pp. 10641–10646, 09 1997.
- [76] J. Widengren and R. Rigler, “Fluorescence correlation spectroscopy as a tool to investigate chemical reactions in solutions and on cell surfaces,” *Cell. Mol. Biol.*, vol. 44, no. 5, pp. 857–879, 1998.
- [77] D. C. Lamb, A. Schenk, C. Röcker, C. Scalfi-Happ, and G. U. Nienhaus, “Sensitivity enhancement in fluorescence correlation spectroscopy of multiple species using time-gated detection,” *Biophys. J.*, vol. 79, no. 2, pp. 1129–1138, 2000.
- [78] T. T. Le, S. Harlepp, C. C. Guet, K. Dittmar, T. Emonet, and P. Cluzel, “Real-time RNA profiling within a single bacterium,” *Proc. Natl. Acad. Sci. USA*, vol. 102, pp. 9160–9164, 06 2005.
- [79] P. Schwille, U. Haupts, S. Maiti, and W. W. Webb, “Molecular Dynamics in Living Cells Observed by Fluorescence Correlation Spectroscopy with One- and Two-Photon Excitation,” *Biophys. J.*, vol. 77, pp. 2251–2265, 1999.
- [80] P. Schwille, F. Oehlenschläger, and N. G. Walter, “Quantitative Hybridization Kinetics of DNA Probes to RNA in Solution Followed by Diffusional Fluorescence Correlation Analysis,” *Biochemistry*, vol. 35, pp. 10182–10193, 05 1996.
- [81] N. G. Walter, P. Schwille, and M. Eigen, “Fluorescence correlation analysis of probe diffusion simplifies quantitative pathogen detection by PCR,” *Proc. Natl. Acad. Sci. USA*, vol. 93, pp. 12805–12810, 11 1996.
- [82] Y. Chen, J. D. Müller, P. T. C. So, and E. Gratton, “The photon counting histogram in fluorescence fluctuation spectroscopy,” *Biophys. J.*, vol. 77, pp. 553–567, 1999.

- [83] Y. Chen, J. D. Müller, S. Y. Tetin, J. D. Tyner, and E. Gratton, “Probing ligand protein binding equilibria with fluorescence fluctuation spectroscopy,” *Biophys. J.*, vol. 79, no. 2, pp. 1074–1084, 2000.
- [84] L. N. Hillesheim and J. D. Müller, “The photon counting histogram in fluorescence fluctuation spectroscopy with non-ideal photodetectors,” *Biophys. J.*, vol. 85, pp. 1948–1958, 2003.
- [85] K. Palo, Ü. Mets, S. Jäger, P. Kask, and K. Gall, “Fluorescence intensity multiple distributions analysis: Concurrent determination of diffusion times and molecular brightness,” *Biophys. J.*, vol. 79, pp. 2858–2866, 2000.
- [86] K. Palo, L. Brand, C. Eggeling, S. Jäger, P. Kask, and K. Gall, “Fluorescence Intensity and Lifetime Distribution Analysis: Toward Higher Accuracy in Fluorescence Fluctuation Spectroscopy,” *Biophys. J.*, vol. 83, no. 2, pp. 605–618, 2002.
- [87] P. Kask, K. Palo, N. Fay, L. Brand, Ü. Mets, D. Ullmann, J. Jungmann, J. Pschorr, and K. Gall, “Two-Dimensional Fluorescence Intensity Distribution Analysis: Theory and Applications,” *Biophys. J.*, vol. 78, no. 4, pp. 1703–1713, 2000.
- [88] Y. Chen, L.-N. Wei, and J. D. Müller, “Unraveling protein-protein interactions in living cells with fluorescence fluctuation brightness analysis,” *Biophys. J.*, vol. 88, pp. 4366–4377, 2005.
- [89] A. Sanchez-Andres, Y. Chen, and J. D. Müller, “Molecular Brightness Determined from a Generalized Form of Mandel’s Q-Parameter,” *Biophys. J.*, vol. 89, no. 5, pp. 3531–3547, 2005.
- [90] J. Enderlein, I. Gregor, D. Patra, and J. Fitter, “Art and artefacts of fluorescence correlation spectroscopy,” *Current Pharmaceutical Biotechnology*, vol. 5, pp. 155–161, 2004.
- [91] J. Enderlein, “Dependence of the optical saturation of fluorescence on rotational diffusion,” *Chem. Phys. Lett.*, vol. 410, pp. 452–456, 2005.
- [92] I. Gregor, D. Patra, and J. Enderlein, “Optical saturation in fluorescence correlation

- spectroscopy under continuous-wave and pulsed excitation,” *ChemPhysChem*, vol. 6, pp. 164–170, 2005.
- [93] R. M. Clegg, “Fluorescence resonance energy transfer and nucleic acids,” *Methods Enzymol.*, vol. 211, pp. 353–388, 1992.
- [94] R. M. Clegg, A. I. H. Murchie, and D. M. Lilley, “Observing the helical geometry of double-strand DNA in solution by fluorescence energy transfer,” *Proc. Natl. Acad. Sci. USA*, vol. 90, pp. 2294–2298, 1993.
- [95] R. Hochstrasser, S. Chen, and D. Millar, “Distance distribution in a dye-linked oligonucleotide determined by time-resolved fluorescence energy transfer,” *Biophys. Chem.*, vol. 45, pp. 133–141, 1992.
- [96] E. A. Jares-Erijman and T. Jovin, “Determination of DNA Helical Handedness by Fluorescence Resonance Energy Transfer,” *J. Mol. Biol.*, vol. 257, pp. 597–617, 1996.
- [97] C. Gohlke, A. Murchie, D. Lilley, and R. Clegg, “Kinking of DNA and RNA helices by bulged nucleotides observed by fluorescence energy transfer,” *Proc. Natl. Acad. Sci. USA*, vol. 91, pp. 11660–11664, 1994.
- [98] M. Lorenz, A. Hillisch, D. Payet, M. Buttinelli, A. Travers, and S. Diekmann, “DNA bending induced by high mobility group proteins studied by fluorescence resonance energy transfer,” *Biochemistry*, vol. 38, no. 37, pp. 12150–12158, 1999.
- [99] F. Stühmeier, J. Wlech, A. Murchie, D. Lilley, and R. Clegg, “Global structure of threeway DNA junctions with and without additional unpaired bases: a fluorescence resonance energy transfer analysis,” *Biochemistry*, vol. 36, pp. 13530–13538, 1997.
- [100] G. Vámosi and R. Clegg, “The helix-coil transition of dna duplexes and hairpins observed by multiple fluorescence parameters,” *Biochemistry*, vol. 37, no. 40, pp. 14300–14316, 1998.
- [101] M. Wallace, L. Ying, and D. Klenermann, “FRET Fluctuation Spectroscopy: Exploring the Conformational Dynamics of a DNA Hairpin Loop,” *J. Phys. Chem. B*, vol. 104, no. 48, pp. 11551–11555, 2000.

- [102] S. Miick, R. Fee, D. Millar, and W. Chazin, "Crossover isomer bias is the primary sequence-dependent property of immobilized holliday junctions," *Proc. Natl. Acad. Sci. USA*, vol. 94, no. 17, pp. 9080–9084, 1997.
- [103] X. Zhuang, L. Bartley, H. Babcock, R. Russel, T. Ha, D. Herschlag, and S. Chu, "A single molecule study of RNA catalysis and folding," *Science*, vol. 288, no. 5473, pp. 2048–2051, 2000.
- [104] A. Deniz, T. Laurence, G. Beligere, M. Dahan, A. Martin, D. Chemla, P. Dawson, P. Schultz, and S. Weiss, "Single-molecule protein folding: Diffusion fluorescence resonance energy transfer studies of the denaturation of chymotrypsin inhibitor 2," *Proc. Natl. Acad. Sci. USA*, vol. 97, no. 10, pp. 5179–5184, 2000.
- [105] S. Weiss, "Fluorescence spectroscopy of single biomolecules," *Science*, vol. 283, pp. 1676–1783, 03 1999.
- [106] S. Weiss, "Measuring conformational dynamics of biomolecules by single molecule fluorescence spectroscopy," *Nat. Struct. Biol.*, vol. 7, no. 9, pp. 724–729, 2000.
- [107] B. Schuler, E. Lipman, and W. Eaton, "Probing the free-energy surface for protein folding with single-molecule fluorescence spectroscopy," *Nature*, vol. 419, pp. 743–747, 2002.
- [108] A. Dietrich, V. Buschmann, C. Müller, and M. Sauer, "Fluorescence energy transfer (FRET) and competing processes in donor-acceptor substituted DNA strands: a comparative study of ensemble and single-molecule data," *Reviews in Molecular Biotechnology*, vol. 82, pp. 211–231, 2002.
- [109] J. Grunwell, J. Glass, T. Lacoste, A. Deniz, D. Chemla, and P. Schultz, "Monitoring the conformational fluctuation of DNA hairpins using single-pair fluorescence resonance energy transfer," *J. Am. Chem. Soc.*, vol. 123, pp. 4295–4303, 2001.
- [110] P. J. Rothwell, S. Berger, O. Kensch, S. Felekyan, M. Antonik, B. M. Wöhrle, T. R. A. S. Goody, and C. A. M. Seidel, "Multiparameter single-molecule fluorescence spectroscopy reveals heterogeneity of HIV-1 reverse transcriptase:primer/template complexes," *Proc. Natl. Acad. Sci. USA*, vol. 100, no. 4, pp. 1655–1660, 2003.

- [111] N. K. Lee, A. N. Kapanidis, Y. Wang, X. Michalet, J. Mukhopadhyay, R. H. Ebright, and S. Weiss, "Accurate FRET measurements within single diffusing biomolecules using Alternating-Laser Excitation," *Biophys J BioFast*, vol. 88, pp. 2939–2953, 4 2005.
- [112] P. R. Schimmel and P. J. Flory, "Conformational energy and configurational statistics of poly-L-proline," *Proc. Natl. Acad. Sci. USA*, vol. 58, pp. 52–59, 1967.
- [113] J. R. Lakowitz, *Principles of Fluorescence Spectroscopy*. New York: Kluwer Academic/Plenum.
- [114] L. Stryer, "Fluorescence energy transfer as a spectroscopic ruler," *Ann. Rev. Biochem*, vol. 47, pp. 819–846, 1978.
- [115] P. R. Selvin, "The renaissance of fluorescence resonance energy transfer," *Nat. Struct. Biol.*, vol. 7, pp. 730–734, 2000.
- [116] B. Schuler, E. A. Lipman, P. J. Steinbach, M. Kumke, and W. A. Eaton, "Polyproline and the "spectroscopic ruler" revisited with single-molecule fluorescence," *Proc. Natl. Acad. Sci. USA*, vol. 102, pp. 2754–2795, 02 2005.
- [117] C. R. Cantor and P. R. Schimmel, *Configurational Statistics of Polymer Chains*, ch. 18, pp. 1012–1014. Freeman, San Francisco, 1980.
- [118] D. C. Lamb, "It's as easy as PIE: Applications of Pulsed Interleaved Excitation to FCCS and FRET," Talk given at the 10th PicoQuant Workshop on Single Molecule Detection and Ultrasensitive Analysis in the Life Sciences, Berlin, 2004.
- [119] E. Hildt, S. Urban, and P. Hofschneider, "Characterization of essential domains for the functionality of the mhbst transcriptional activator and identification of a minimal mhbst activator," *Oncogene*, vol. 11, pp. 2055–2066, 1995.
- [120] P. M. Cowan and S. McGavin, "Structure of poly-L-proline," *Nature*, vol. 176, pp. 501–503, 1955.
- [121] Invitrogen Website, Molecular Probes, "Data Table — 1.3 Alexa Fluor Dyes Spanning the Visible and Near-Infrared Spectrum."

- <http://probes.invitrogen.com/servlets/datatable?item=30005&id=38089>, accessed 16-August-2006.
- [122] Wikipedia, The Free Encyclopedia, “Alexa (fluor).” <http://en.wikipedia.org/w/index.php?oldid=65646185>, accessed 16-August-2006.
- [123] D. Pearlman, D. Case, J. Caldwell, W. Ross, III, T. Cheatham, S. DeBolt, D. Ferguson, G. Seibel, and P. Kollman, “AMBER, a computer program for applying molecular mechanics, normal mode analysis, molecular dynamics and free energy calculations to elucidate the structures and energies of molecules,” *Comp. Phys. Commun.*, vol. 91, pp. 1–41, 1995.
- [124] J. Ponder and D. Case, “Force fields for protein simulations,” *Adv. Prot. Chem.*, vol. 66, pp. 27–85, 2003.
- [125] D. Thirumalai and B. Y. Ha, *Statistical Mechanics of Semiflexible Chains: A Mean Field Variational Approach*, ch. 1, pp. 1–35. Academic Press, San Diego, 1988.